



## PRODUCTION AND CHARACTERIZATION OF ACTIVATED CARBON FROM POMEGRANATE PULP BY PHOSPHORIC ACID

Eylem PEHLİVAN<sup>1</sup>

1. Faculty of Engineering, Department of Chemical and Process Engineering, Bilecik Şeyh Edebali University, Bilecik, Turkey

*(This article first appeared in PPM2017 and was accepted as a non-peer-reviewed manuscript to be published in JOTCSA)*

**Abstract:** In this study, samples of activated carbon were prepared from pomegranate pulp by chemical activation.  $H_3PO_4$  was used as chemical activation agent and three impregnation ratios (50-100-200%) by mass were applied on biomass at impregnation times of 24 and 48 hours. Carbonization is applied to impregnated biomass samples under  $N_2$  sweeping gas in a fixed bed reactor at 500 and 700 °C. For determination of chemical and physical properties of the obtained activated carbons; elemental analysis was applied to determine the elemental composition (C, H, N, O) and FT-IR spectra was used to analyze the functional groups. BET equation was used to calculate the surface areas of activated carbons. For understanding the changes in the surface structure, activated carbons were conducted to Scanning Electron Microscopy (SEM). Maximum BET surface area (840  $m^2/g$ ) was reached with the activated carbon generated using 200%  $H_3PO_4$  impregnated biomass sample, at a carbonization temperature of 700 °C and impregnation time of 48 hours. Experimental results showed that impregnation ratio have a significant effect on the pore structure of activated carbon and pomegranate pulp seems to be an alternative precursor for commercial activated carbon production.

**Keywords:** Chemical activation, carbonization, characterization, activated carbon, biomass.

**Cite This:** Pehlivan E. PRODUCTION AND CHARACTERIZATION OF ACTIVATED CARBON FROM POMEGRANATE PULP BY PHOSPHORIC ACID. Journal of the Turkish Chemical Society, Section A: Chemistry. 5(sp. is. 1):1-8.

**Corresponding Author. E-mail:** [eylem.onal@bilecik.edu.tr](mailto:eylem.onal@bilecik.edu.tr)

## INTRODUCTION

Activated carbon is a black charcoal-like material, which has a well-developed pore structure, which leads to its large surface area; in addition, it possesses good mechanical strength. Activated carbon is commonly used as adsorbent in wastewater treatment and gas removal as well as a catalyst. Commercial activated carbon is normally obtained by using coal as the precursor, making it very costly and hence requiring searches for cheaper substitutes, mainly from biomass. Agricultural waste is gaining credence as a suitable precursor for the preparation of activated carbon to be used as an adsorbent due to its easy availability and nearly-zero or low cost [Senthilkumar, *et al.*, 1999].

In this study, activated carbons were prepared from pomegranate pulp by chemical activation with  $H_3PO_4$ . The yields, specific surface areas, pore volumes and, pore sizes of the activated carbons were determined. The influence of the different impregnation ratios, activation times and the carbonization temperatures on surface chemistry was investigated using instrumental methods such as elemental analysis, FT-IR, BET and SEM.

## MATERIALS AND METHODS

Pomegranate pulp have been supplied by a fruit factory in the region of western Turkey. It was dried at room temperature. Drying was timed up to obtaining a constant weight. After drying raw material was ground in a high-speed rotary cutting mill and stored in a cool and dark room. Average particle size in 0.5245 mm was used for preparation of activated carbon. The characteristics of the raw material are presented in Table 1.

**Table 1:** Properties of the pomegranate pulp.

<i>Proximate analysis</i>	<i>%</i>	<i>Ultimate analysis</i>	<i>%</i>
Moisture	8.38	C	48.80
Volatile matters	76.36	H	5.36
Ash	2.51	N	1.75
Fixed carbon	13.64	O*	44.09
Bulk density(kg/m <sup>3</sup> )	500	Empirical formula	CH <sub>1.1.31</sub> N <sub>0.031</sub> O <sub>0.68</sub>
<i>Component analysis</i>	<i>%</i>	H/C	1.31
Extractive material	3.70	O/C	0.68
Hemicellulose	15.56	Higher calorific value (Mj/kg)	18.88
Lignin	46.56		
Cellulose*	35.52		

Raw material was directly impregnated with chemical activation agent. Ground and sieved pomegranate pulp were treated with  $H_3PO_4$  solutions at room temperature in three different weight ratios as 0.5/1–1/1–2/1. Continuous mixing of the precursor with chemicals for 24 and 48 h was maintained by using a magnetic stirrer. After mixing, solutions were allowed to dry at room temperature for 24 h and then dried at 85 °C for 72 h in a temperature controlled oven to prepare impregnated samples. Impregnated samples were carbonized in a stainless steel fixed bed reactor at 500 and 700 °C under nitrogen ( $N_2$ ) flow of 100 cm<sup>3</sup>/min and at a heating rate of 10 °C/min and held at this temperature for 1 h. After being cooled, all the carbonized

samples were washed several times with hot water until pH became neutral and finally washed with cold water to remove residual chemicals. Washed samples were dried at 105 °C for 24 h to obtain the final activated carbons. Results in Table 2 indicate that both the concentrations and carbonization temperatures influenced the yields of the activated carbons.. An increase in the reagent concentration at the same temperatures resulted in a decrease in the yields of the activated carbons. An increase in the temperature at the same concentrations led to a decrease in the yields of the activated carbons.

$$\text{Yield of activated carbon wt\%} = \frac{\text{Final weight of activated carbon}}{\text{Initial weight of pomegranate pulp}} \times 100 \quad (1)$$

**Table 2:** Nomenclature, preparation conditions and yields of activated carbon.

Activated Carbon Name	Carbonization temperature (°C)	Impregnation ratio (g/g)	Impregnation time (hours)	Yield (%)
AC1	500	0,5/1	24	23,25
AC2	500	1/1	24	12,32
AC3	500	2/1	24	6,30
AC4	500	0,5/1	48	28,70
AC5	500	1/1	48	10,21
AC6	500	2/1	48	2,25
AC7	700	0,5/1	24	24,91
AC8	700	1/1	24	12,08
AC9	700	2/1	24	4,62
AC10	700	0,5/1	48	24,00
AC11	700	1/1	48	13,46
AC12	700	2/1	48	4,60

**Table 3:** Surface areas and pore volumes of activated carbons.

AC	<i>S</i> <sub>BET</sub> (m <sup>2</sup> /g)	<i>S</i> <sub>mikro</sub> (m <sup>2</sup> /g)	<i>S</i> <sub>ext</sub> (m <sup>2</sup> /g)	<i>V</i> <sub>total</sub> (cm <sup>3</sup> /g)	<i>V</i> <sub>micro</sub>	
(cm <sup>3</sup> /g)	<i>V</i> <sub>meso</sub>					
(cm <sup>3</sup> /g)	% <i>S</i> <sub>micro</sub>	<i>D</i> <sub>p</sub> (°A)				
AC1	352	183	169	0.2153		
	0.1313	0.084	52	170		
AC2	617	443	174	0.3948	0,3178	0.077 72 97
AC3	830	735	95	0.7313	0,6953	0.036 88 72
AC4	266	171	95	0.1505	0.0715	0.079 64 225
AC5	602	335	267	0.3630	0.2403	0.1227 55 99
AC6	830	652	178	0.6150	0.5380	0.077 78 77
AC7	378	221	157	0.2193	0.1174	0.1019 58 158
AC8	597	394	203	0.3953	0.3043	0.091 65 100
AC9	869	728	141	0.8167	0.7727	0.044 86 71
AC10	293	208	85	0.1626	0.067	0.095 70 204
AC11	669	383	286	0.3746	0.2437	0.1309 57 89
AC12	819	664	155	0.6868	0.6214	0.065 81 73

### Characterization of the activated carbons

The carbon, hydrogen, nitrogen, and oxygen (by difference) contents of the pomegranate pulp and activated carbons were measured using a Carlo Erba EA 1108 model Elemental Analyzer. Surface areas of each activated carbon were calculated from N<sub>2</sub> adsorption isotherms by using

BET (Brunauer–Emmett–Teller) method with Quantachrome Autosorb 1 analyzer. The adsorption data of the total pore volume ( $V_{\text{total}}$ ) were determined from the amount of nitrogen adsorbed at a relative pressure of 0.995 and calculated with the manufacturer's software. The same adsorption data were also used for calculation of the micropore volume by the t-plot method. The mesopore volume ( $V_{\text{meso}}$ ) was calculated by subtracting  $V_{\text{micro}}$  from  $V_{\text{total}}$  ( $V_{\text{meso}} = V_{\text{total}} - V_{\text{micro}}$ ). The functional groups on the surface of the activated carbon were determined by Bruker Tensor 27 Model FTIR spectrometer. The spectrum was obtained over the range of 400–4,000  $\text{cm}^{-1}$ . The surface morphologies were studied by SEM. The SEM images were obtained using Zeiss Evo 50 SEM.

## RESULTS AND DISCUSSION

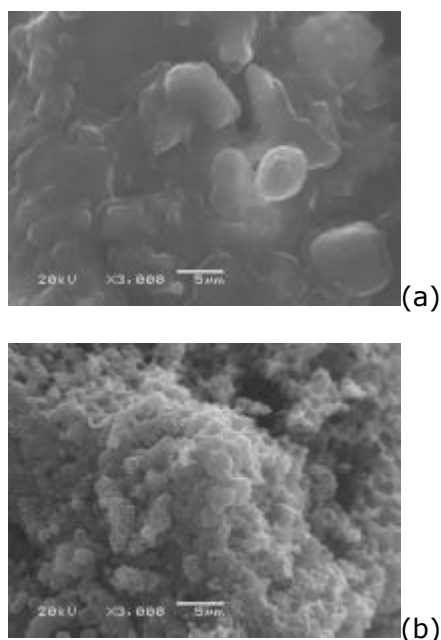
BET surface area of activated carbon is important because, like other physical and chemical characteristics, it may strongly affect the reactivity and combustion behavior. The higher surface areas are probably due to the opening of the restricted pores [Ioannidou and Zabaniotou, 2007]. BET surface area of activated carbons are shown in Table 3. It can be seen that surface area increases with impregnation ratio and carbonization temperature. The highest surface area (869  $\text{m}^2/\text{g}$ ) was obtained having 2/1 impregnation ratio and 700 °C temperature which is relatively high surface area for an activated carbon. The effect of different activation temperature impregnation ratios and times on total pore volume, micropore volume and micropore area for the activated carbons with the highest surface areas are given in Table 4. It was seen that, microporous structure is well developed for the activated carbon produced activation with increasing impregnation ratio up to 2/1. The optimum impregnation ratio to get higher surface area and pore volume was determined as 2/1%, where the highest surface area of 839  $\text{m}^2/\text{g}$  with a pore volume of 0.8167  $\text{cm}^3/\text{g}$  were obtained activated carbon.

The elemental analysis results of the activated carbons obtained are shown in Table 4. Compared to the pomegranate pulp, all carbon samples had higher contents of C and lower contents of H and O. It can be said that chemical activation accelerated the removal of H and O and this resulted in an increased C content as expected.

**Table 4:** Elemental analysis of activated carbons.

	(%) N	(%) C	(%) H	(%) O
Raw material	1.75	48.80	6.96	42.49
AC1	2.07	67.26	4.10	26.52
AC2	1.50	68.63	4.18	25.67
AC3	1.42	69.11	3.77	25.69
AC4	1.69	71.59	4.59	22.11
AC5	1.54	70.16	4.80	23.48
AC6	1.47	65.83	4.71	27.96
AC7	1.47	70.30	3.49	24.73
AC8	1.23	64.18	3.36	31.21
AC9	1.10	63.00	3.31	32.58
AC10	1.25	67.78	3.14	27.81
AC11	1.11	63.54	3.17	32.15
AC12	0.98	64.53	2.67	31.80

Scanning electron microscopy (SEM) technique was used to observe the surface physical morphology of the samples. SEM micrographs of the pomegranate pulp and the produced activated carbon (AC9) were given in Figure 2a and b. From Figure 2a, it is clear that the pomegranate pulp has fibrous structure with smooth surface.  $H_3PO_4$  activation has substantial effect on the pomegranate pulp with impregnation ratio of 2/1 shows cavities on their external surface that improve the porosity. Different pore sizes and shapes were observed on the activated carbon surface because of depolymerization and subsequent release of volatile organic substances from carbonization.

**Figure 1:** SEM images pomegranate pulp (a) and its activated carbon (b).

Functional groups are very important characteristics of the activated carbons, because they determine the surface properties of the carbons and their quality. FT-IR spectroscopy in its various forms is an important and forceful technique which can give useful information about structures. It can provide basic spectra of activated carbons, especially for determination of

types and intensities of their surface functional groups [El-Hendawy, 2006]. FT-IR spectrum of pomegranate pulp is given in Figure. 3. The broad and flat band at about  $3300\text{--}3400\text{ cm}^{-1}$  shows the presence of OH stretching vibration of alcohol, phenol or carboxylic acid. The strong band at  $2950\text{--}2800\text{ cm}^{-1}$  represents C H stretching vibration in methyl group. Another strong band at  $1750\text{ cm}^{-1}$  is ascribed to C=O vibrations probably from esters, ketones or aliphatic acids. The band at  $1620\text{ cm}^{-1}$  can be ascribed to C= C aromatic ring stretching vibration. The peak at  $1245\text{--}1155\text{ cm}^{-1}$  may be assigned to the hydrogen-bonded P=O, O C stretching vibrations in P -O -C linkage, and P=O(OH). The very strong band at  $1020\text{ cm}^{-1}$  represents C-O stretching vibrations. The weaker bands between  $765$  and  $530\text{ cm}^{-1}$  are ascribed to aromatic structures. Figure. 4 represents the FTIR spectra. The spectra are approximately very similar for the activated carbons; however they differ from raw material, which is a result of the chemical and thermal treatment. Some bands disappeared or weakened during the activated carbon preparation including the impregnation and the activation; in particular, the bands located in two regions between  $3,600$  and  $2,800\text{ cm}^{-1}$  and between  $800$  and  $400\text{ cm}^{-1}$ . The first peak at  $3,300\text{ cm}^{-1}$  is ascribed to OH stretching vibration in hydroxyl groups. This peak is stronger for the pomegranate pulp and has weakened for the activated carbon. Two strong bands observed at  $2,920$  and  $2,860\text{ cm}^{-1}$  are assigned to asymmetric C-H and symmetric C-H bands, respectively, present in alkyl groups such as methyl and methylene groups. However, this band disappeared in the activated carbon. These bands were visible in raw material, but not in activated carbon.

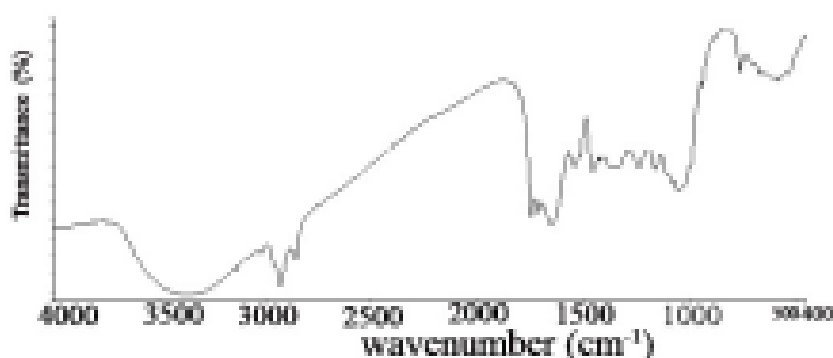


**Figure 2:** FT-IR spectrum of pomegranate pulp.

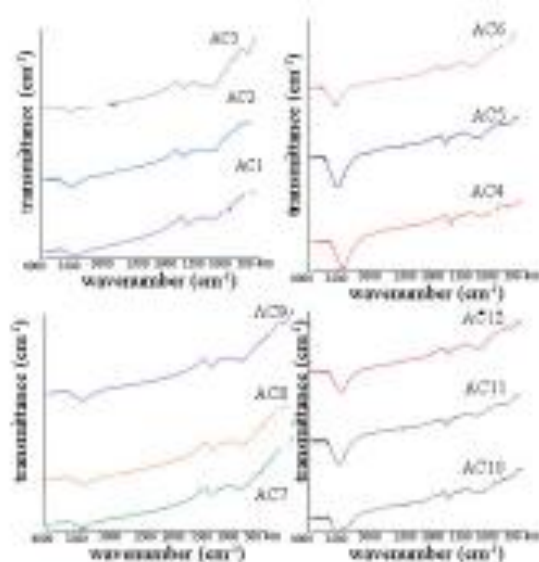


**Figure 3:** FT-IR spectra of activated carbons.

## CONCLUSIONS

The present investigation showed that pomegranate pulp, a waste of fruit juice industries, can be effectively used as a raw material for the preparation of activated carbon. Activation temperature and impregnation ratios are effective on the porosity, surface area of activated carbons. The production of activated carbons with high surface area and highly developed micropore from pomegranate pulp is indeed of importance from the view point of economic and environmental aspects. The activated carbons produced can be effectively used as a low cost adsorbent for various environmental applications such as removing hazardous compounds from industrial wastewater and waste gases.

## REFERENCES

- Hendawy, A.A.,2006. Variation in the FTIR spectra of a biomass under impregnation, carbonization and oxidation conditions, *Journal of Analytical Applied Pyrolysis*, 75, 159.
- Ioannidou, O. and Zabaniotou, A., 2007. Agricultural residues as precursors for activated carbon production—a review, *Renewable and Sustainable Energy Reviews*, 11 ,1966.
- Senthilkumar, T., Chattopadhyay, S.K. and Miranda, L.M., 2017. Optimization of Activated Carbon Preparation from Pomegranate Peel (*Punica granatum* Peel) Using RSM, *Chemical Engineering Communications*,204 , 238.





## EFFECTS OF Zn-DOPING ON THE PHOTOCATALYTIC ACTIVITY AND MICROSTRUCTURES OF NANOCRYSTALLINE SnO<sub>2</sub> POWDERS

Metin Yurddaskal<sup>1,2</sup>, , Serdar Yildirim<sup>1,2</sup>, , Tuncay Dikici<sup>3</sup>, Melis Yurddaskal<sup>4</sup>,  
Mustafa Erol<sup>3</sup>, , Idil Aritman<sup>1,2</sup>, , Hilmiye Deniz Ertugrul Uygun<sup>1,2</sup>,  and  
Erdal Celik<sup>2,5,6</sup>

*(This article first appeared in PPM2017 and was accepted as a non-peer-reviewed manuscript to be published in JOTCSA)*

<sup>1</sup> Dokuz Eylul University, The Graduate School of Natural and Applied Sciences, 35390, Izmir, Turkey

<sup>2</sup> Dokuz Eylul University, Center for Fabrication and Applications of Electronic Materials (EMUM), 35390, Izmir, Turkey

<sup>3</sup> Izmir Katip Celebi University, Department of Materials Science and Engineering, 35620, Izmir, Turkey

<sup>4</sup> Celal Bayar University, Department of Mechanical Engineering, 45140, Manisa, Turkey

<sup>5</sup> Dokuz Eylul University, Department of Metallurgical and Materials Engineering, 35390, Izmir, Turkey

<sup>6</sup> Dokuz Eylul University, Department of Nanoscience and Nanoengineering, 35390, Izmir, Turkey

**Abstract:** In this study, undoped and Zn-doped SnO<sub>2</sub> nanoparticles in different concentrations were synthesized by flame spray pyrolysis (FSP) technique. The produced particles were post-annealed after FSP process at 600 °C in order to obtain a crystalline structure. The structural analysis of the produced powders was performed by X-Ray Diffraction (XRD) methods. The surface morphology of the nanoparticles was identified using scanning electron microscopy (SEM). In addition, photocatalytic degradation of aqueous methylene blue (MB) solutions were evaluated using undoped and Zn-doped SnO<sub>2</sub> nanoparticles under UV light illumination. Photocatalytic degradation of the MB solutions followed the pseudo-first-order-kinetics and the effect of the Zn doping amount on the photocatalytic reaction was investigated.

**Keywords:** SnO<sub>2</sub>; Zn-doped; nanoparticles; photocatalysis; flame spray pyrolysis.

**Cite This:** Yurddaskal M, Yildirim S, Dikici T, Yurddaskal M, Erol M, Aritman İ, et al. EFFECTS OF Zn-DOPING ON THE PHOTOCATALYTIC ACTIVITY AND MICROSTRUCTURES OF NANOCRYSTALLINE SnO<sub>2</sub> POWDERS. Journal of the Turkish Chemical Society, Section A: Chemistry. 5(sp. is. 1):9-14.

**Corresponding Author. E-mail:** [metin.yurddaskal@deu.edu.tr](mailto:metin.yurddaskal@deu.edu.tr).

## INTRODUCTION

In recent years, environmental pollution has been an important issue (Huang *et al.*, 2012). Semiconducting oxide nanocrystals, which have unique properties, has been intensively studied for photocatalytic applications in the fields of catalytically decomposing and detecting organic compounds that are usually volatile and toxic (Pauluskas *et al.*, 2013).

SnO<sub>2</sub>, as an n-type semiconductor with a wide band gap (3.6 eV). SnO<sub>2</sub> materials can be produced by many techniques such as solvothermal synthesis (Jia *et al.*, 2009), chemical precipitation (Shanmugam *et al.*, 2016), hydrothermal (Dave *et al.*, 2010), hydrolysis (Rahman *et al.*, 2011), flame spray pyrolysis (FSP) (Ang *et al.*, 2011). These methods provide to obtain particles with controlled shape, porosity and particle size for wide range of applications such as dye based solar cells, optoelectronic devices, electrode materials, transistors, gas sensors, and catalyst supports (Jia *et al.*, 2009). The versatile capabilities of the flame spray pyrolysis are given ideal characteristics to the method as ideal synthetic method to produce homogeny nanoparticles fast and cost effectively. Instead of wet chemistry the literatures are suggested that doped and undoped metallic nanoparticles production provide homogenous doped material synthesis methodology (Liu *et al.*, 2010).

For improving the effective performance of SnO<sub>2</sub>, a common way is doping SnO<sub>2</sub> with proper metal elements such as Sb, Fe, Co, Ni, Mn, Zn etc. (Huang *et al.*, 2012). Zn doped SnO<sub>2</sub> has more effective photocatalytic properties and ability to modify its structural performance and preferred by regarding other materials. Doping leads to obtain large surface area and trapping mass centers. These particles have more effective photocatalytic activity (Yildirim *et al.*, 2016).

In this study, Zn doped SnO<sub>2</sub> with different amount of Zn were synthesized by flame spray pyrolysis (FSP) technique to improve the catalytic performance.

## EXPERIMENTAL

In this work, undoped and Zn-doped tin oxide (SnO<sub>2</sub>) samples were prepared using flame spray pyrolysis (FSP) technique (Tethis, Np 10, Italy). The liquid precursor solution was sprayed into the flame from syringe pump with a ratio of 5 mL/min. The mixture of supporting gas (methane/oxygen) flow rate was kept constant with 5 L/min and oxygen/fuel ratio of 1.5/3. Undoped and different ratio of Zn doped (1, 3, 5, 7 and 9

at.%) SnO<sub>2</sub> nanoparticles with diameters of below 200 nm were obtained with this method.

The phase structure and crystallinity of the samples are studied by a Thermo Scientific ARL- Ka X-ray diffractometer (XRD). This instrument works with voltage and current settings of 45 kV and 44 mA, respectively. The Cu-Ka has been used as the radiation source (1.5405 Å). The samples were scanned over a range of 20° to 70° with a scanning rate of 2°/min. The morphology and structure of the samples were characterized using by a scanning electron microscope (SEM, Philips XL 30S FEG).

Photocatalytic activity of undoped and Zn-doped SnO<sub>2</sub> nanoparticles were determined by studying photodegradation of methylene blue (MB) dye solution under UV light. MB (Sigma Aldrich) solution with 10<sup>-5</sup> M concentration was prepared with distilled water and undoped and Zn doped SnO<sub>2</sub> nanoparticles were dispersed in this solution.

The photodegradation of the MB experiments were conducted up to 180 min. The distance between the light source and the suspension beaker was kept as 20 cm. All the absorption experiments of the MB solutions were performed using by a UV-1240 (Shimadzu) spectrophotometer based on the characteristic absorption peak of MB at 664 nm.

## RESULTS AND DISCUSSION

The X-ray diffraction (XRD) pattern of the undoped and 1-9 at.% Zn doped SnO<sub>2</sub> nanoparticles produced by FSP technique are shown in Figure 1. It was observed that all peaks of the SnO<sub>2</sub> phases corresponding to 26.6, 33.9, 38.0, 51.8 and 55.0 at 2θ values were assigned to (110), (101), (200), (211) and (220), respectively (JCPDS Card No: 41-1445). These crystal planes were prominently seen in XRD indicating the polycrystalline nature of powder of SnO<sub>2</sub>. No other peak for the polycrystalline phases of SnO<sub>2</sub> or any other impurity was seen and no impurities were detected.

SEM analysis was performed to reveal morphological features of the sample. SEM micrographs of polycrystalline SnO<sub>2</sub> nanoparticles are shown in Figure 2. These micrographs show homogeneous, uniform distribution of SnO<sub>2</sub> nanoparticles over a scanned area. It's clear that the surface morphology of the nanoparticles has an important role in their photocatalytic activity. General view for undoped and 1% Zn doped SnO<sub>2</sub> nanoparticles can be seen in Figure 2a and c, respectively. Additionally, Figure 2b and d represent the detailed structure and morphology of the nanoparticles

with 100k magnification. It can be clearly seen that 1% Zn doped SnO<sub>2</sub> nanoparticles have different morphology from undoped SnO<sub>2</sub> nanoparticles. This may affect the photocatalytic activity of the produced nanoparticles.

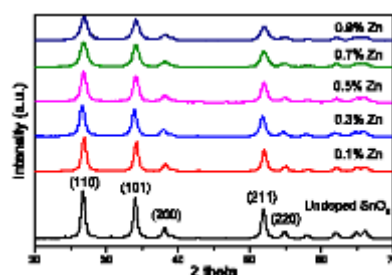


**Figure 1:** XRD patterns of the undoped and Zn doped SnO<sub>2</sub> nanoparticles produced by FSP.

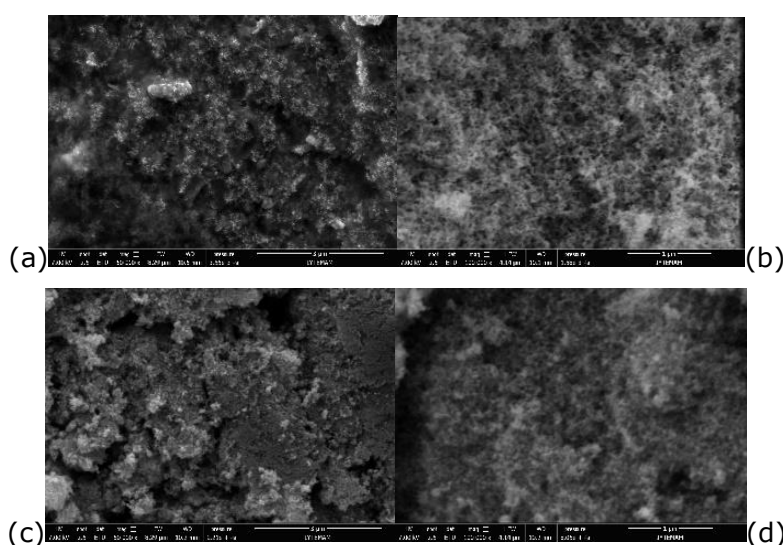


**Figure 2:** SEM images of the undoped and 9% at. Zn doped SnO<sub>2</sub> nanoparticles with low (a-c) and high magnifications (b-d).

The photocatalytic activities of undoped and Zn doped SnO<sub>2</sub> nanoparticles were investigated by the degradation of MB solution. It was observed that the suspension mixed with 1% Zn doped SnO<sub>2</sub> nanoparticles was decolorized higher than undoped SnO<sub>2</sub>. Figure 3 plotted the photocatalytic degradation of MB with irradiation time for 120 min, compared with undoped and 1-9% Zn doped SnO<sub>2</sub>. As shown in Figure 3, both undoped and 1% Zn doped SnO<sub>2</sub> nanoparticles decolorized MB effectively, nevertheless 1% Zn doped SnO<sub>2</sub> nanoparticles exhibited the enhanced photocatalytic activity than undoped SnO<sub>2</sub>.

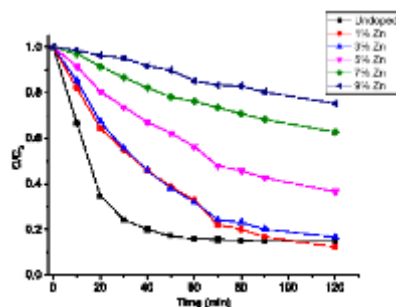


**Figure 3:** Photocatalytic degradations the undoped and Zn doped SnO<sub>2</sub> nanoparticles produced by FSP.

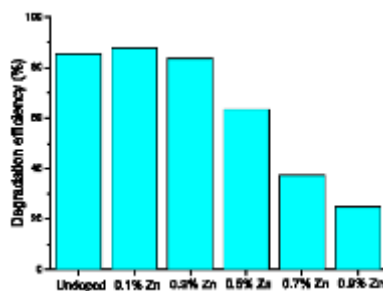


**Figure 4:** Photocatalytic efficiencies of the undoped and Zn doped SnO<sub>2</sub> nanoparticles produced by FSP.

The degradation efficiency of the photocatalysts was given in Figure 4. The degradation efficiency of the 0.1% Zn doped SnO<sub>2</sub> nanoparticles was 87,6%, whereas that of the undoped SnO<sub>2</sub> nanoparticles was 85.2%. With Zn doping exceeds 1% at., the photocatalytic activity of the SnO<sub>2</sub> nanoparticles began to decrease, which probably is attributed to the increased recombination of photoexcited electrons and holes.

## CONCLUSION

In this study, we successfully performed flame spray pyrolysis synthesis of the undoped and Zn doped SnO<sub>2</sub> nanoparticles. The sample 1% Zn doped SnO<sub>2</sub> has the best photocatalyst for degradation of the organic dye, MB. It can be seen that the photocatalytic activity of the SnO<sub>2</sub> nanoparticles increased after Zn doping, and the optimum amount for Zn doped nanoparticles was 1%. With further increasing amount of Zn, photocatalytic performance was gradually decreased. The best dopant concentration exhibiting maximum photocatalytic activity can be explained by space charge creation and rate of charge carrier recombination thanks to Zn doping into SnO<sub>2</sub>.

**REFERENCES**

- Ang GT, Toh GH, Bakar MZA, Abdullah AZ, Othman MR. High sensitivity and fast response SnO<sub>2</sub> and La-SnO<sub>2</sub> catalytic pellet sensors in detecting volatile organic compounds. *Process Saf Environ Prot.* Institution of Chemical Engineers; 2011;89(3):186–92.
- Dave N, Pautler BG, Farvid SS, Radovanovic P V. Synthesis and surface control of colloidal Cr<sup>3+</sup>-doped SnO<sub>2</sub> transparent magnetic semiconductor nanocrystals. *Nanotechnology.* 2010;21(13):134023.
- Huang H, Tian S, Xu J, Xie Z, Zeng D. Needle-like Zn-doped SnO<sub>2</sub> nanorods with enhanced photocatalytic and gas sensing properties.
- Jia T, Wang W, Long F, Fu Z, Wang H, Zhang Q. Synthesis, Characterization, and Photocatalytic Activity of Zn-Doped SnO<sub>2</sub> Hierarchical Architectures Assembled by Nanocones. 2009;9071–7.
- Liu J, Gu F, Hu Y, Li C. Flame Synthesis of Tin Oxide Nanorods: A Continuous and Scalable Approach. *J Phys Chem C.* 2010;114(13):5867–70.
- Paulauskas IE, Modeshia DR, Obaid Y, Basahel SN, Al-ghamdi AA, Sartain FK. Photocatalytic Activity of Doped and Undoped Titanium Dioxide Nanoparticles Synthesised by Flame Spray Pyrolysis. 2013;(1):32–43.
- Rahman MM, Jamal A, Khan SB, Faisal M. Highly sensitive ethanol chemical sensor based on Ni-doped SnO<sub>2</sub> nanostructure materials. *Biosens Bioelectron.* Elsevier B.V.; 2011;28(1):127–34.
- Shanmugam N, Sathya T, Viruthagiri G, Kalyanasundaram C, Gobi R, Ragupathy S. Photocatalytic degradation of brilliant green using undoped and Zn doped SnO<sub>2</sub> nanoparticles under sunlight irradiation. *Appl Surf Sci.* Elsevier B.V.; 2016;360:283–90.
- Yildirim S, Yurddaskal M, Dikici T, Aritman I. Structural and luminescence properties of undoped, Nd<sup>3+</sup> and Er<sup>3+</sup> doped TiO<sub>2</sub> nanoparticles synthesized by flame spray pyrolysis method. *Ceram Int.* Elsevier; 2016;42(9):10579–86.



## ENHANCED PHOTOCATALYTIC PROPERTIES OF Sn-DOPED ZnO NANOPARTICLES BY FLAME SPRAY PYROLYSIS UNDER UV LIGHT IRRADIATION

Metin Yurddaskal<sup>1,2</sup> , Serdar Yildirim<sup>1,2</sup> , Tuncay Dikici<sup>3</sup>, Melis Yurddaskal<sup>4</sup>, Mustafa Erol<sup>3</sup> , Idil Aritman<sup>1,2</sup>  and Erdal Celik<sup>2,5,6</sup>

*(This article first appeared in PPM2017 and was accepted as a non-peer-reviewed manuscript to be published in JOTCSA)*

<sup>1</sup> Dokuz Eylul University, The Graduate School of Natural and Applied Sciences, 35390, Izmir, Turkey

<sup>2</sup> Dokuz Eylul University, Center for Fabrication and Applications of Electronic Materials (EMUM), 35390, Izmir, Turkey

<sup>3</sup> Izmir Katip Celebi University, Department of Materials Science and Engineering, 35620, Izmir, Turkey

<sup>4</sup> Celal Bayar University, Department of Mechanical Engineering, 45140, Manisa, Turkey

<sup>5</sup> Dokuz Eylul University, Department of Metallurgical and Materials Engineering, 35390, Izmir, Turkey

<sup>6</sup> Dokuz Eylul University, Department of Nanoscience and Nanoengineering, 35390, Izmir, Turkey

**Abstract:** Zinc oxide (ZnO) is widely used in different areas thanks to its unique photocatalytic, optic and electrical properties. Sn doped ZnO nanoparticles were synthesized through flame spray pyrolysis (FSP) technique. The Sn dopant concentrations were 1, 3, 5, 7 and 9 at. % in produced ZnO nanoparticles. The structural analysis of the produced powders was performed by X-Ray Diffraction (XRD) methods. The surface morphology and particle size distribution of the nanoparticles were identified using scanning electron microscopy (SEM), and dynamic light scattering (DLS) techniques. In addition to this, produced photocatalysts were evaluated for degradation of aqueous methylene blue (MB) solutions under UV light irradiation. Sn-doped nanoparticles have superior photocatalytic activity compared to un-doped ZnO.

**Keywords:** ZnO, Sn-doped, nanoparticles, photocatalysis, flame spray pyrolysis,

**Cite This:** Yurddaskal M, Yildirim S, Dikici T, Yurddaskal M, Erol M, Aritman İ, et al. ENHANCED PHOTOCATALYTIC PROPERTIES OF Sn-DOPED ZnO NANOPARTICLES BY FLAME SPRAY PYROLYSIS UNDER UV LIGHT IRRADIATION. Journal of the Turkish Chemical Society, Section A: Chemistry. 5(sp. is. 1):15-22.

**Corresponding Author. E-mail:** [metin.yurddaskal@deu.edu.tr](mailto:metin.yurddaskal@deu.edu.tr).

## INTRODUCTION

Doped or non-doped metal oxide nanostructures are preferred in the electronic materials category due to their superior physical, chemical and photocatalytic properties. Studies have demonstrated that broadband semiconductor photocatalysts such as ZnO can reduce various organic contaminants that offer great potential for completely removing toxic chemicals under UV radiation [Sun *et al.*, 2011, Wu *et al.*, 2011, Jia *et al.*, 2011 and Al-Hadeethi *et al.*, 2017]. In many photocatalytic reactions, ZnO has been reported to have high photocatalytic activity in the degradation of various organic contaminants in both acidic and basic media. The greatest advantage of ZnO is the absorption of more light quanta than other semiconductors by absorbing a larger portion of the UV spectrum [Postica *et al.*, 2017, Kumar *et al.*, 2016 and Ismail *et al.*, 2016]. The suppression of recombination of photon-electron-hole pairs in semiconductors is necessary to increase the photocatalytic activity. Doping is a very useful way to improve load separation in semiconductor systems [Andolsi *et al.*, 2017 and So *et al.*, 2017]. In particular, tin (Sn) is considered one of the most important doping elements to improve the photocatalytic activity of ZnO. Among the additive elements, Sn is compatible with the cage structure due to the similarity of ionic radius with zinc. As a result, Sn doping in ZnO is expected to affect the response or sensitivity of these materials for various gases [Aydin *et al.*, 2015, Chahmat *et al.*, 2014, Zegadi *et al.*, 2014 and Li *et al.*, 2012]. Different methods have been used in the literature for the synthesis of doped and undoped ZnO or other metal oxides; such as hydrothermal synthesis, sol-gel, solid state synthesis, liquid emulsion method, and magnetron sputtering. Flame spray pyrolysis (FSP) method is preferred method due to low grain size and homogeneous grain distribution compared to other production methods. Moreover, studying at low temperatures makes FSP safer and cheaper than solid state synthesis [Bae *et al.*, 2005, Height *et al.*, 2006, Salman *et al.*, 2017 and Rherari *et al.*, 2017]. In this study, Sn doped ZnO nanoparticles were easily produced by FSP. Structural, microstructural and photocatalytic properties of the produced nanoparticles were investigated and compared with the studies done in the literature and the results were evaluated.

## EXPERIMENTAL

Undoped and Sn-doped zinc oxide (ZnO) nanoparticles were produced by flame spray pyrolysis (FSP) equipment (Tethis, Np 10, Italy). The liquid precursor solution was fed into the flame from syringe pump with a feed rate of 5 ml/min. The supporting methane/oxygen flow rate was kept constant with 5 l/min and oxygen/fuel ratio of 1.5/3.

Undoped, 1, 3, 5, 7 and 9 at.% Sn doped ZnO nanoparticles with diameters of below 200 nm were produced using this method.

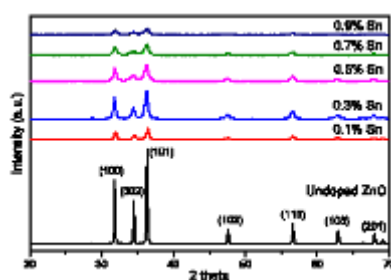
Phase identification and crystal structures of the samples were performed by means of a Thermo Scientific ARL- K $\alpha$  X-ray diffractometer (XRD). This instrument works with voltage and current settings of 45 kV and 44 mA, respectively. The Cu-K $\alpha$  has been used as the radiation source (1.5405 Å). Diffraction patterns were acquired in the range of 20° to 70° with a scanning rate of 2°/min. The surface morphology and microstructure of the samples were characterized by a scanning electron microscope (SEM, Zeiss Carl Ultra Plus).

To simulate the color change due to photocatalytic decomposition (color change of dye component such as methylene blue, MB), an experimental setup was established. 10<sup>-5</sup> M MB (Sigma Aldrich) and distilled water solution were prepared. Produced undoped and Sn doped ZnO nanoparticles were dispersed in this solution. The photodegradation of the MB experiments were practiced up to 180 min. The distance between the light source and the suspension beaker was kept as 20 cm. The absorption of the MB solutions was analyzed by a UV-1240 (Shimadzu) spectrophotometer based on the characteristic absorption of MB peak at 664 nm.

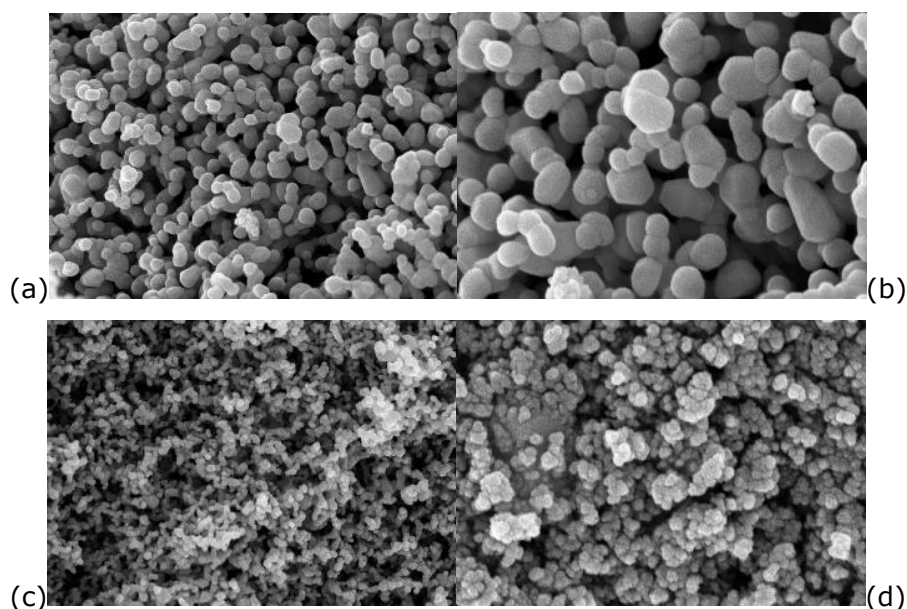
## RESULTS AND DISCUSSION

Figure 1 depicts the X-ray diffraction analysis (XRD) of the undoped and 1-9 at.% Sn doped ZnO nanoparticles produced by FSP technique. It was observed that all peaks of the ZnO phases corresponding to 31.8, 34.4, 36.3, 47.6, 56.6, 62.9 and 67.9° at 2 $\theta$  values were assigned to (100), (002), (101), (102), (110), (103) and (201) of ZnO nanoparticles in accordance with the zincite pattern COD 9004180. These results indicate that the samples were polycrystalline wurtzite structure. No other peak for the cubic phases of ZnO or any other ZnO structures such as ZnO<sub>2</sub> or Zn(OH)<sub>4</sub> was seen and no characteristic peaks of any impurities were detected.

The surface morphology plays an important role in photocatalytic activity. Figure 2a and c illustrates structures of the nanoparticles in general view for undoped and 1% Sn doped ZnO, respectively. In addition, Figure 2b and d represents the detailed structure and morphology of the nanoparticles with 200k magnification. In contrast to undoped ZnO nanoparticles, 1% Sn doped ZnO nanoparticles have higher surface area. It can be inferred that Sn doping into the ZnO at a certain amount improved the photocatalytic properties due to increasing surface area.



**Figure 1:** XRD patterns of the undoped and Sn doped ZnO nanoparticles produced by FSP.



**Figure 2:** SEM images of the undoped and 1% at. Sn doped ZnO nanoparticles with low (a-c) and high magnifications (b-d). (a,c) 1  $\mu$ m. (b,d) 100 nm.

As mentioned before, the MB dye was used to assess the photocatalytic performance of the undoped and %1-9 Sn doped ZnO nanoparticles. Fig. 3 shows the photocatalytic degradation of MB by the produced nanoparticles. Considering the doping amount into the ZnO nanoparticles, the sample 1% Sn doped ZnO has the best photocatalytic activity. 1% Sn doped ZnO exhibited a very good photoactivity compared to all other samples. At the end of 180 minutes, MB was degraded more than 99% thanks to Sn doping into ZnO. The degradation efficiency of the 0.1% Sn doped ZnO nanoparticles was 99.1%, whereas that of the undoped ZnO nanoparticles was 61.3%.

The degradation efficiency of the photocatalysts was given in Fig. 4. Further observation showed that photocatalytic activity gradually decreased with increasing amount of Sn in the nanoparticles. The 0.1% Sn doped ZnO photocatalyst exhibited the highest

photocatalytic activity for 180 min. The increasing of the photocatalytic performance with 1% Sn doped ZnO can be explained by inhibition of recombination centers (Demirci *et al.*, 2017).

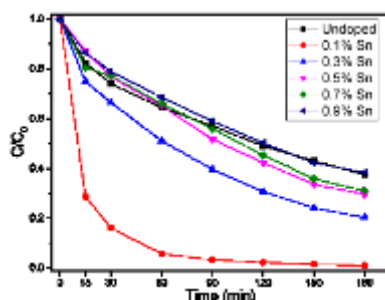


**Figure 3:** Photocatalytic degradations the undoped and Sn doped ZnO nanoparticles produced by FSP.

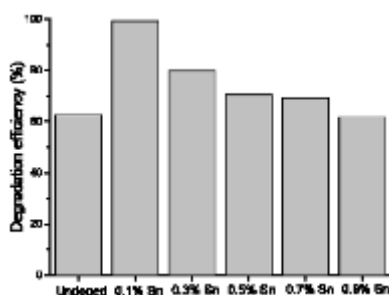


**Figure 4:** Photocatalytic efficiencies of the undoped and Sn doped ZnO nanoparticles produced by FSP.

## CONCLUSION

In summary, undoped and Sn doped ZnO nanoparticles were produced by flame spray pyrolysis method successfully. The sample 1% Sn doped ZnO is the best photocatalyst for degradation of MB. It was observed that the photocatalytic activity of ZnO nanoparticles increased after Sn doping, and the optimal Sn doped content was 1%. With further increasing amount of Sn, photocatalytic performance was gradually decreased. The best dopant concentration exhibiting maximum photocatalytic activity is explained based on space charge creation and rate of charge carrier recombination thanks to Sn doping into ZnO.

## REFERENCES

- Al-Hadeethi, Y., Umar, A., Al-Heniti, S. H., Kumar, R., Kim, S. H., Zhang, X., & Raffah, B. M. (2017). 2D Sn-doped ZnO ultrathin nanosheet networks for enhanced acetone gas sensing application. *Ceramics International*, 43(2), 2418-2423.
- Andolsi, Y., Chaabouni, F., & Abaab, M. (2017). Sn doping effects on properties of ZnO thin films deposited by RF magnetron sputtering using a powder target. *Journal of Materials Science: Materials in Electronics*, 28(12), 8347-8358.
- Aydin, H., El-Nasser, H. M., Aydin, C., Al-Ghamdi, A. A., & Yakuphanoglu, F. (2015). Synthesis and characterization of nanostructured undoped and Sn-doped ZnO thin films via sol-gel approach. *Applied Surface Science*, 350, 109-114.
- Bae, S. Y., Na, C. W., Kang, J. H., & Park, J. (2005). Comparative structure and optical properties of Ga-, In-, and Sn-doped ZnO nanowires synthesized via thermal evaporation. *The Journal of Physical Chemistry B*, 109(7), 2526-2531.
- Chahmat, N., Souier, T., Mokri, A., Bououdina, M., Aida, M. S., & Ghers, M. (2014). Structure, microstructure and optical properties of Sn-doped ZnO thin films. *Journal of Alloys and Compounds*, 593, 148-153.
- Demirci S., Dikici T., Yurddaskal M., Gultekin S., Toparli M., Celik E., Synthesis and characterization of Ag doped TiO<sub>2</sub> heterojunction films and their photocatalytic performances *Appl. Surf. Sci.*, 390 (2016), pp. 591-601.
- Height, M. J., Mädler, L., Pratsinis, S. E., & Krumeich, F. (2006). Nanorods of ZnO made by flame spray pyrolysis. *Chemistry of Materials*, 18(2), 572-578.
- Ismail, A. S., Mamat, M. H., Sin, N. M., Malek, M. F., Zoolfakar, A. S., Suriani, A. B., & Rusop, M. (2016). Fabrication of hierarchical Sn-doped ZnO nanorod arrays through sonicated sol-gel immersion for room temperature, resistive-type humidity sensor applications. *Ceramics International*, 42(8), 9785-9795.
- Jia, X., Fan, H., Afzaal, M., Wu, X., & O'Brien, P. (2011). Solid state synthesis of tin-doped ZnO at room temperature: characterization and its enhanced gas sensing and photocatalytic properties. *Journal of hazardous materials*, 193, 194-199.
- Kumar, E. S., Mohammadbeigi, F., Boatner, L. A., & Watkins, S. P. (2016). High resolution photoluminescence spectroscopy of Sn-doped ZnO single crystals. *Journal of Luminescence*, 176, 47-51.
- Li, X., Chang, Y., & Long, Y. (2012). Influence of Sn doping on ZnO sensing properties for ethanol and acetone. *Materials Science and Engineering: C*, 32(4), 817-821.
- Postica, V., Hoppe, M., Gröttrup, J., Hayes, P., Rübisch, V., Smazna, D., ... & Lupan, O. (2017). Morphology dependent UV photoresponse of Sn-doped ZnO microstructures. *Solid State Sciences*, 71, 75-86.
- Rherari, A., Addou, M., Sofiani, Z., Jbilou, M., & Diani, M. (2017). Effect of lithium on linear and nonlinear optical properties of Sn-doped zinc oxide prepared by spray pyrolysis. In *IOP Conference Series: Materials Science and Engineering* (Vol. 186, No. 1, p. 012002). IOP Publishing.
- Salman, S. A., Hazza, S. Q., & Abbas, S. J. (2017). Effect of Sn Doping on Structural and Electrical Properties of ZnO Thin Films Prepared by Chemical Spray Pyrolysis Method.
- So, H. S., Hwang, S. B., Jung, D. H., & Lee, H. (2017). Optical and electrical properties of Sn-doped ZnO thin films studied via spectroscopic ellipsometry and hall effect measurements. *Journal of the Korean Physical Society*, 70(7), 706-713.

Sun, J. H., Dong, S. Y., Feng, J. L., Yin, X. J., & Zhao, X. C. (2011). Enhanced sunlight photocatalytic performance of Sn-doped ZnO for Methylene Blue degradation. *Journal of Molecular Catalysis A: Chemical*, 335(1), 145-150.

Wu, C., Shen, L., Yu, H., Huang, Q., & Zhang, Y. C. (2011). Synthesis of Sn-doped ZnO nanorods and their photocatalytic properties. *Materials Research Bulletin*, 46(7), 1107-1112.

Zegadi, C., Abdelkebir, K., Chaumont, D., Adnane, M., & Hamzaoui, S. (2014). Influence of Sn Low Doping on the Morphological, Structural and Optical Properties of ZnO Films Deposited by Sol Gel Dip-Coating. *Advances in Materials Physics and Chemistry*, 4(05), 93.





## Colour Removal from Biologically Treated Textile Dyeing Wastewater with Natural and Novel Pre-Hydrolysed Coagulants

G.Yildiz Tore\*, R.Ata, S.Özden Çelik, Ş. Kırhan Sesler

*(This article first appeared in PPM2017 and was accepted as a non-peer-reviewed manuscript to be published in JOTCSA)*

Namık Kemal University, Çorlu Engineering Faculty, Environmental Engineering Department 59860 Çorlu-TEKİRDAĞ/TURKEY

**ABSTRACT:** In this paper, natural (chitosan and starch) and novel pre-hydrolysed coagulants (PACl, PAFCl, PFS and PFC) were performed with coagulant aid for colour removal from a biologically treated textile wastewater including multiple dyes (indigo and reactive). According to the experimental results, optimum coagulant dosages which provide the best colour removal for PACl, PAFCl, PFS (%10) and PFC (%10), were determined as 80 mg/L, 10 mg/L, 3 mg/L and 40 mg/L, respectively, at pH 4 and pH 6,98 (natural pH of studied wastewater, pH<sub>nww</sub>). Maximum colour removal was determined as 97% for PAFCl, minimum removal was 23% for PFC at pH 4, while it was calculated as 75% and 52% at pH<sub>nww</sub>. COD removal was observed as 45% at pH 4 and 55% at pH<sub>nww</sub> for maximum colour removal. Sludge production rate was measured as 71 kg/d while this rate was found as 60 kg/d at pH<sub>nww</sub>. On the other hand colour removal efficiencies were determined in the range of 55-88% at pH<sub>nww</sub> and pH 3 for chitosan while it was calculated as 52% for starch at pH<sub>nww</sub> and pH 9. According to the results, PAFCl and chitosan were found as the best coagulants for colour removal of investigated textile wastewater. According to the economic analysis results, the best colour efficiency were found as 97% with PAFCl and the second best colour removal were found as 88% with Chitosan. Due to lower sludge production than PAFCl and lower chemical costs; Chitosan can be considered as a reasonable alternative for this wastewater.

**Keywords:** Natural and Novel pre-hydrolysed coagulant, Colour removal, Textile wastewater, PAFCl, Chitosan.

**Cite this:** Yıldız Töre G, Ata R, Özden Çelik S, Kırhan Sesler Ş. Colour Removal from Biologically Treated Textile Dyeing Wastewater with Natural and Novel Pre-Hydrolysed Coagulants. JOTCSA. 2017;5(sp. is. 1):23–36.

**\*Corresponding author.** E-mail: gyildiztore@nku.edu.tr.

## INTRODUCTION

Textile industry use huge amount of water and complex hazardous chemicals at various processing stages of the textile materials. The unused parts of these chemicals are discharged as wastewater that is high in temperature, biochemical oxygen demand (BOD), chemical oxygen demand (COD), colour, pH, turbidity and toxic chemicals. Conventional chemical and biological treatment methods are widely applied in the textile and other coloured wastewater. Although these systems are successful to remove the conventional parameters, textile influents containing especially different types of dyes which have high molecular weight and complex structures, show very low biodegradability in terms of colour removal and so, they are insufficient to provide the discharge standards for receiving bodies (1). In this context, it is very important to decide which approach is the most suitable for colour removal from textile wastewater in terms of environment. Generally, wastewater containing dyes is difficult to treat due to the nature of the dye. Most of the dyes are stable against to light and oxidizing agents and are resistant to biologic degradation. The most used technologies to treat wastewater containing dyes are based on physical-chemical and/or biological processes. Coagulation and sedimentation processes are known to be effective in eliminating the colours of insoluble dyes such as disperse ones. However, these are not conditions for soluble dyes including reactive dyes (2). The well-known conventional coagulants such as alum, polyaluminum chloride, iron(II) sulfate and lime are widely used in textile wastewater treatment. More than 90% of colour removal from acid dyes could be achieved by activated carbon. However, it is not effective coagulant for basic and direct dyes (3). Chemical coagulation has a complex structure involving various interacted parameters, therefore it must be defined how well coagulant will function under given conditions. On the basis of colour removal, chemical coagulants can be categorised as hydrolysing metallic salts, pre-hydrolysing metallic salts and synthetic cationic polymers, respectively (4). Recently, the usage of natural (chitosan, starch derivatives, guar gum, tannins, alginates ext.) and novel hydrolysed polymers (polyaluminium chloride (PACl), polyaluminium ferric chloride (PAFCl), polyferrous sulphate (PFS) and polyferric chloride (PFCl)) in wastewater treatment application have increased rapidly (1,5,6). It is reported in the literature that these polymers are more efficient than conventional inorganic coagulants for especially colour removal due to the synergistic effect of two different coagulant substances in a single substance (6). The literature studies have reported that novel pre-hydrolysed coagulants such as polyaluminium chloride (PACl), polyaluminium ferric chloride (PAFCl), polyferrous sulphate (PFS) and polyferric chloride (PFCl) have an advantage that good colour removal even at low temperature. Another advantage

of these coagulant is to produce lower volume of sludge compared to conventional coagulants. In this context, the effectiveness of various novel pre-hydrolysing coagulants for the treatment of textile wastewater have been studied in the literature recently. These studies mostly reported that both they don't need pH correction, additional coagulant aid etc. (1,4,7). When the literature studies done with PACL are examined; it has been found that PACI provides stronger and rapidly settleable floc formation, which causes faster flocculation than that of alum at the same dose (7,8). Studies, run in textile wastewaters with PAFCl are very limited in the literature. In the study performed by Gao *et al.* in 2001, it was found that PAFCl is more effective in colour and turbidity removal than PACI and PFS for the wastewater of the petrochemical industry at pH 7.0-8.4. It is shown that floc formation occurred faster than the other coagulants. The coexistence of aluminum and iron ions in PAFCl has been found to result in faster floc formation, sedimentation and hence more efficient colour removal (8). In a study conducted by Wang *et al.* (2008) on textile wastewater with PFS; in the case of 150 mg/L PFS applied to wastewater at pH 9, it was found that 71% COD, 56% BOD, 62% AKM and >50% colour removal were achieved (9). When literature studies done with PFCI are examined; in studies published by Wang *et al.* in 2010, ferric chloride ( $\text{FeCl}_3$ ), PFCI and polydimethyldiallylammonium chloride (PDMDAAC) flocculants in textile wastewaters were compared for colour removal. It has been found that the combined use of the flocculants in the study gives more successful results. It has been reported that the combination of  $\text{FeCl}_3$  - PDMDAAC and PFCI - PDMDAAC is more effective in colour removal than conventional use (10). A study done by Chen *et al.* for a synthetic dyed textile wastewaters in 2010, PFCI and polyamine (EPI-DMA) were investigated for colour removal and flocking performance at different concentrations. Colour removal for direct yellow 201 and remazol red 24 were obtained as 98% and 19% with PFCI at pH 7.5. It was found that in the combination of PFCI / EPI-DMA, the colour removal were found 97.5% for remazol red 24 and direct yellow 201 at pH 6.0 and flock formation has been found to give better results (11). In the study conducted by Wei *et al.*, the effects of different dosages of PFCI/PDMDAAC combinations on the colour removal and flocculation dynamics of reactive and disperse dyeing textile wastewaters were investigated. 60% of reactive dyes, 95.5% of colour removal in disperse dyes and the highest rate of floc formation were determined with 30 mg/L PFCI/PDADMAAC application (12).

Many natural plant and non-plant derived polymers such as chitosan, starch, guar gum, arabic gum, moringa, tannin, cactus etc. are known as natural coagulants. There are limited studies carried out with starch for coagulation of industrial wastewater. In a study conducted by Hasçakır in 2003 with starch coagulation; 85-90% and 20%

COD removal have been achieved for paper industry wastewater and domestic wastewater, respectively. In the same study, 70-75% COD removal and 30-35% COD removal in domestic wastewater were detected when starch was used as a flocculant together with alum, lime and ferric chloride, but no study was made on the formation and amount of sludge (13). Chitosan is obtained from the fleece material based on the shells of red-crusted crabs and shrimps and proved an adsorbent and/or coagulant characteristics. Chitosan has high cationic charge density with long polymer chains leading to bridging of aggregation and precipitation behave as a biological cationic polymer. Numerous works have demonstrated that chitosan can be a potential alternative to conventional coagulation/flocculation application for waste water treatment to remove both particulate and dissolved substances. However, more studies are required to optimize the process. Sanghi and Bhattacharya (2005) showed that chitosan is very effective as a coagulant aid to remove acidic and direct dyes. They also reported that reactive dyes with anthraquinone groups were the most difficult to remove with chitosan and PAC (14). Gandjidoust *et al.* (1997) reported that chitosan resulted in the higher removal in both colour and TOC than synthetic polymers (poly(acrylmide) or PAM, poly(ethyleneimine) or PEI) and a chemical coagulant (alum) (15). Similar results were reported by Rodrigues *et al.* (2008) and Wang *et al.* (2007) for the treatment of pulp and paper mill wastewater. These groups have also proposed modified chitosan-based biopolymers as adsorbents and/or coagulants for the removal of SS, COD and colour from pulp and paper mill effluent (16, 17). In addition, these coagulants, which will not interfere with biological treatment due to the fact that the coagulant residue can serve as a nutrient for microorganisms and novel properties of natural coagulants having the biodegradable nature of non-toxic biodegradable properties, can be regarded as promising coagulant and coagulant aid for the treatment of textile wastewater, especially for the first stage.

The aim of this study is to evaluate the colour removal efficiency of biologically treated textile dyeing wastewater, including multiple dyes (indigo and reactive), with natural and novel pre-hydrolysed coagulants and to describe optimum conditions (pH, coagulant dosage, sludge volume etc.) based on the economically achievable best removal efficiency.

## MATERIAL AND METHODS

### Materials

This study was carried out in the wastewater treatment system treating denim washing (70%) and reactive dyeing (30%) wastewater located in Çorlu town of Tekirdağ. Treatment system has a 1500 m<sup>3</sup>/d capacity composed of physical and biological treatment units including conventional activated sludge processes. Treated wastewater has been discharged in a receiving body called Sinanlı stream. Experimental studies were carried out on treated wastewater samples to characterize wastewater for one year. For wastewater characterisation; between 2013/ November-December and 2014/January, daily composite samples were taken from the biological treatment effluent, which were called 'raw wastewater' in chemical experimental study results.

### Coagulants and Coagulation/ Flocculation test procedure (Jar Test)

All natural and novel pre-hydrolysed coagulants were supplied as analytical grade. Only PFCI was prepared according to the method used by Jincheng Wei *et.al.* (18). All coagulation/ flocculation experiments were conducted in one liter glass beakers using a conventional Jar-test apparatus (VELP Scientifica, FC6S) equipped with four beakers. 1000 mL stock solutions of each polymer were prepared 10 % w/w. 1 mL (2 mg/L) anionic polyelectrolite was used as coagulant aids for each coagulant. The solutions were stirred rapidly at 200 rpm for 2 min during the addition of coagulants, followed by slow stirring at 45 rpm for 15 min and settling for 30 min. After settling, supernatant samples were collected and filtered using coarse filter for further analysis. Optimum conditions were assessed for colour and COD removal before treatability experiments were started. Jar test trials were made at efficient pH intervals (acidic, basic and real ww), mixing rate and flocculant dosage which is determined in treatability pre-studies for each coagulant. The pH of the samples were adjusted to acidic and basic conditions by adding 1N HCl or NaOH solutions for all coagulants. After then, supernatant and sludge characterisation were carried out on the samples for the determination of best options.

### Analytical Methods

All analyses were performed according to the standard methods [Standart Methods, 1998] except COD and colour parameters. The COD and colour were measured according to ISO 6060 Method [ISO 6060, 1986] and ISO 7887 method [ISO 7887, 1987], respectively. The adjustment of pH was carried out using a (WTW pH315i) pH meter. The colour of the supernatant after jar test was determined by the spectral absorption coefficient (SAC) method. Percentage of SAC removal was calculated based

on absorbance measurements by the spectrophotometer at three different wavelengths ( $\lambda = 436, 525$  and  $620$ ).

## RESULTS AND DISCUSSION

### Effluent Characterisation

Wastewater characterisation is given at Table 1. It shows that colour parameter as a pollution parameter does not achieve the discharge criteria defined in the European Standard EN ISO 7887 for receiving environment although organic content and pH values are enough low for receiving body. So, it needs to further chemical treatment to achieve the discharge standards determined in Turkey.

Table 1: Wastewater characterisation of investigated treatment plant.

Parameters	Unit	Raw	Effluent	Discharge Criteria**
Total COD	mg/L	495	106	300
Soluble COD (0,45 $\mu$ )	mg/L	450	80	-
Suspended Solid (SS)	mg/L	85	6	100
Conductivity	$\mu$ mho/cm	-	2843	-
Colour	CN*	-	26,2	7
436 nm				
525 nm	CN*	-	23,3	5
620 nm	CN*	-	23,7	3
pH	-	6,3	6,98	6-9

\*CN: Colour number, ( $m^{-1}$ ) \*\*WPCR: Water Pollution Control Regulation, \*\*\* discharge criteria defined in the European Standard EN ISO 7887 for receiving environment.

### Jar Test results

Optimum conditions were determined for colour and COD removal, and sludge production were evaluated under these optimum conditions. Comparative results of jar tests were given at Table 2. According to the jar test results, carried out at the determined optimum dosages, maximum colour removal was calculated as 97% for PAFCl, while minimum removal determined as 23% at pH4 with. For maximum colour removal, sludge production rate was measured as 71 kg/d while this rate was found as 60 kg/d at pH<sub>nww</sub>. On the other hand, COD removal was measured as 55 % at this maximum colour removal. Maximum colour removal was calculated almost close together at pH<sub>nww</sub> as  $\approx 75\%$  for PAFCL and PACl. Tun et al. (2007) studied at pH:7.5 and similar colour removal efficiencies (75%) have been obtained with the dose of PACl as high as 800 mg/L (19).

**Table 2:** Comparative removal efficiencies and sludge production.

<b>COLOUR REMOVAL</b>											
80 mg/L PACI (10%)+ 1 ml (1/500) A.P.E		10 mg/L PAFCl (10%) + 1 ml (1/500) A.P.E		3 mg/L (10%) PFS+ 2 ml 1/500 A.P.E		40 mg/L PFCl+ 1 ml 1/500 A.P.E		600 mg/L Starch + 0.3 ml 1/500 A.P.E		4.5 mg/L chitosan+ 0.1 ml 1/500 A.P.E	
pH4	pHnw w	pH4	pHnw w	pH4	pHnw w	pH4	pHnw w	pHnw w	pH9	pHnw w	pH3
76 %	74%	97 %	75%	79 %	48%	23 %	52%	52%	52 %	55%	88 %
<b>COD REMOVAL</b>											
80 mg/L PACI (10%)+ 1 ml (1/500) A.P.E		10 mg/L PAFCl (10%) + 1 ml (1/500) A.P.E		3 mg/L (10%) PFS+ 2 ml 1/500 A.P.E		40 mg/L PFCl+ 1 ml 1/500 A.P.E		600 mg/L Starch + 0.3 ml 1/500 A.P.E		4.5 mg/L chitosan+ 0.1 ml 1/500 A.P.E	
pHnw		pH4	pHnw w	pH4	pHnw w	pH4	pHnw w	pHnw w	pH9	pH3	
53%		55 %	45%	47 %	67%	67 %	63%	60%	65 %	56%	
<b>SLUDGE PRODUCTION (kg/day)</b>											
80 mg/L PACI (10%)+ 1 ml (1/500) A.P.E		10 mg/L PAFCl (10%) + 1 ml (1/500) A.P.E		3 mg/L (10%) PFS+ 2 ml 1/500 A.P.E		40 mg/L PFCl+ 1 ml 1/500 A.P.E		600 mg/L Starch + 0.3 ml 1/500 A.P.E		4.5 mg/L chitosan+ 0.1 ml 1/500 A.P.E	
pH4	pHnw w	pH4	pHnw w	pH4	pHnw w	pH4	pHnw w	pHnw w	pH9	pHnw w	pH3
56	79	71	60	31	14	123	148	509	560	123	24

Maximum COD removal efficiencies were obtained at pHnw with PFS and PFCl as 67% and 63%, respectively. Minimum COD removal was determined as 45% at the same pH. Wang et al. (2008) obtained similar results with high dose of PFS (150 mg/L) at pH 9. Wang et al. (2008) studied with denim washing wastewater and obtained 71% COD, 56% BOD and 50 % colour. In our study, similar colour removal results were obtained at pHnw, while relatively higher colour removal (79%) has been obtained with as low as 3 mg/L of PFS dose at pH 4 (9).

Comparative results obtained in present study were given in Fig. 1-6.

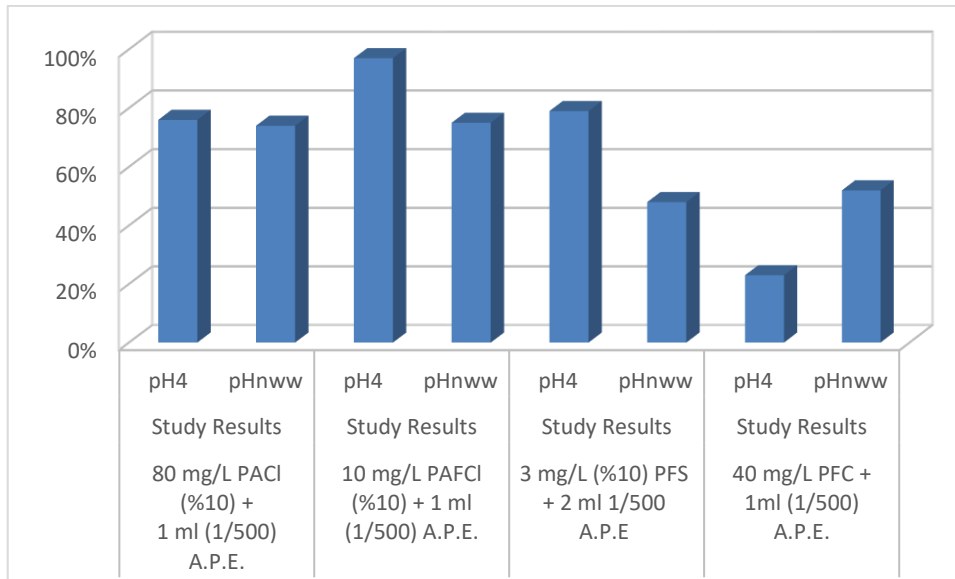


**Figure 1:** Comparative Colour Removal Results Obtained with Pre-hydrolyzed Metal Salts.

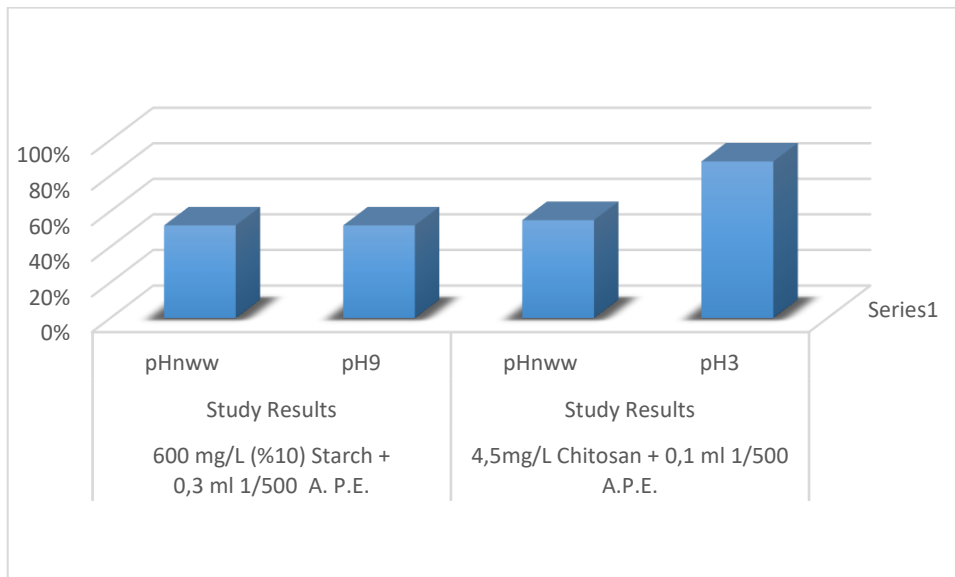


**Figure 2:** Comparative Colour Removal Results Obtained with Natural Coagulant.

Colour removal efficiency was determined as 52 % for PFCI at pHnww. Chen et al. (2010) evaluated yellow 201 and remazol red removal from synthetic wastewater at pH 7.5 and obtained 98% and 19% colour removal, respectively (11). Our results obtained with PFCI is relatively lower, can be attributed to usage of real wastewater. In addition, Wei et al. (2009) obtained 95.5 % of colour removal with disperse dye, while only 60% of colour removal can be achieved with reactive dye (12). Considering the reactive consistency of the given wastewater used in our study, our results are similar to the literature.

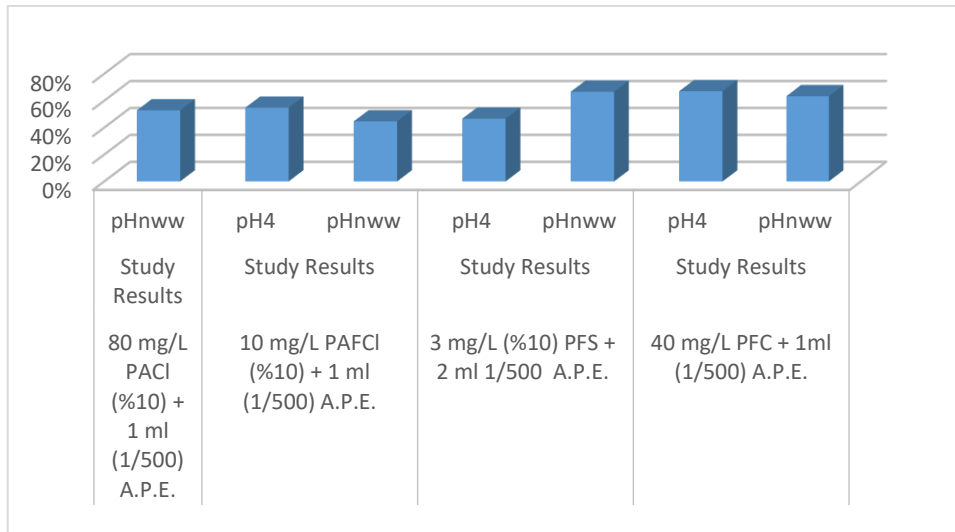


**Figure 3:** Comparative COD Removal Results Obtained with Pre-hydrolyzed Metal Salts.

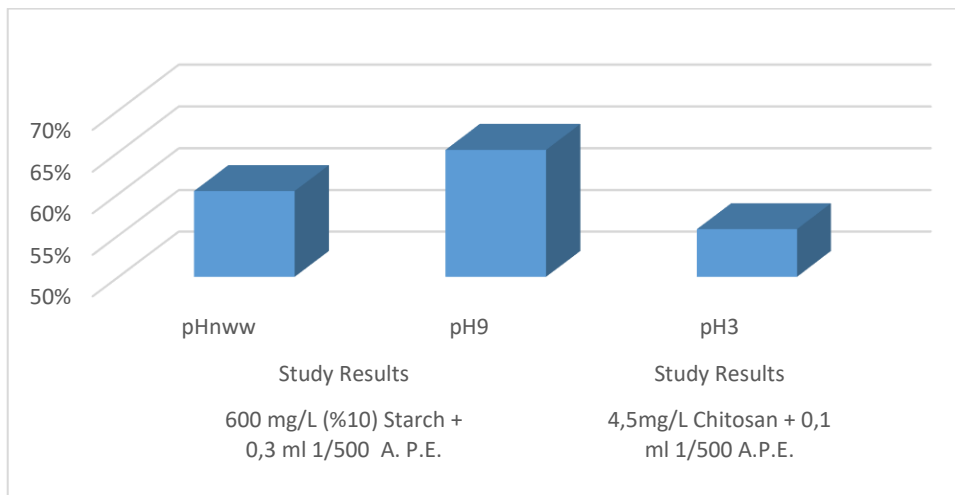


**Figure 4:** Comparative COD Removal Results Obtained with Natural Coagulant.

In this study 88% colour removal was obtained with 4,5 mg/L chitosan at pH 3. This removal rate obtained in accordance with the literature. Szygula *et al.* (2009) obtained 99% colour removal for Acid Blue 92 with 100 mg/L chitosan at pH 9 (20). Mahmoodi *et al.* (2011) reported 75% and 95 % colour removal for Acid Green 25 and Direct Red 23 at pH 2 (21).

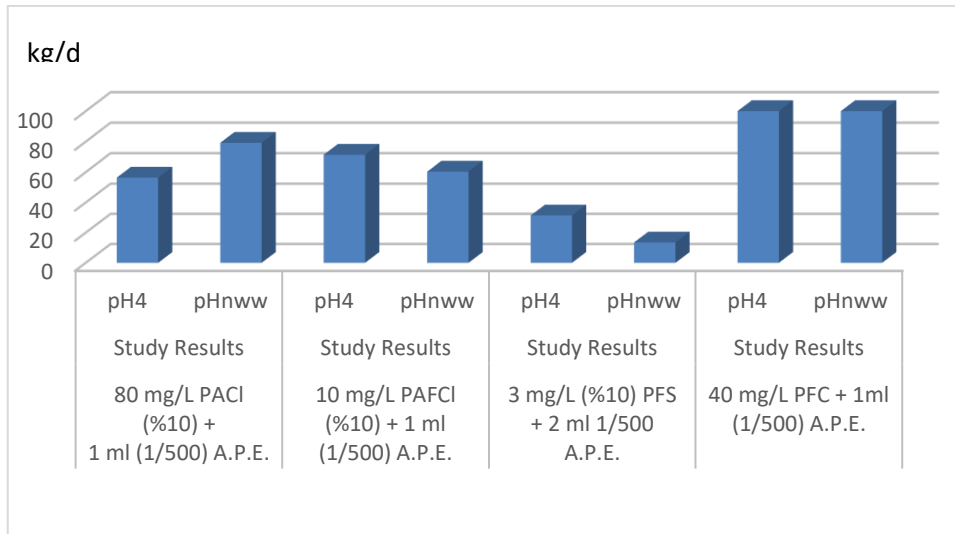


**Figure 5:** Comparative Sludge Production Potential Obtained with Pre-hydrolyzed Metal Salts.

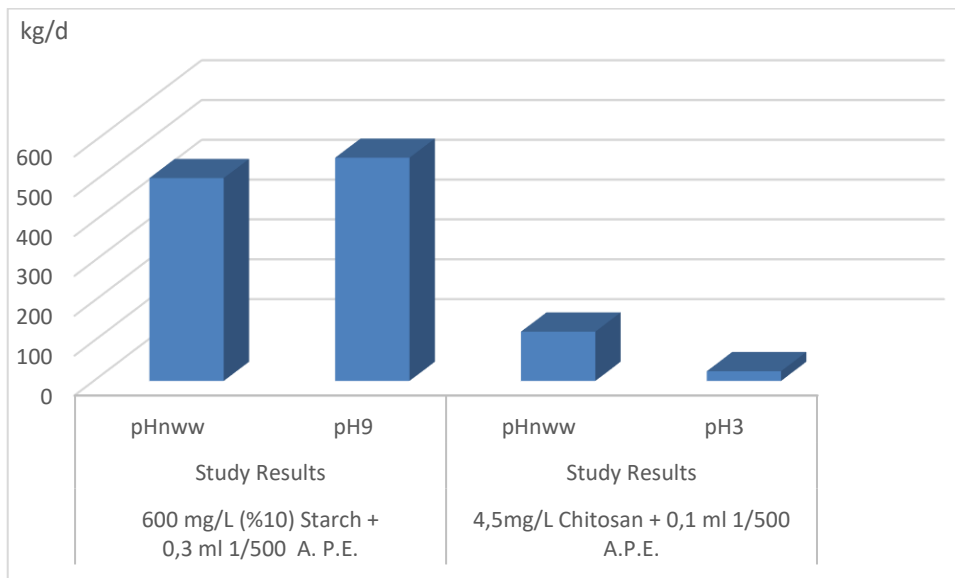


**Figure 6:** Comparative Sludge Production Potential Obtained with Natural Coagulants.

On the basis of daily sludge production, maximum sludge production was observed for starch at pH 9, while minimum was measured for PFS at pHnww. While colour removal efficiencies were determined as 52% for starch both at pHnww and pH9, very important difference was found for chitosan between at pHnww and pH 3. However, although pH 3 seems very efficient condition for colour removal with chitosan, this efficiency range was found to be lower than the maximum removal efficiency obtained for PAFCl as novel-prehydrolysed coagulant and also after coagulation, there is need a neutralisation. It should be considered that this results in an increase in the operating cost.

### Economic Analysis

According to the economic analysis results, daily cost with PACI was determined as 81 \$/d at pH<sub>nww</sub>. Daily cost were 81 \$/d at same pH, while it increased to 27 \$/d at pH 4 for PAFCI. This difference results from the addition of pH adjustment cost. Daily cost with PFS was found as 7 \$/d and 20 \$/d for pH<sub>nww</sub> and pH 4, respectively. While daily cost with PFCI is calculated as 16 \$/d and 29 \$/d for pH<sub>nww</sub> and pH 4, respectively. Starch produce 1 \$/d as coagulant cost, similarly chitosan produce 0,01 \$/d coagulant cost for pH<sub>nww</sub>, while, 14\$/d coagulant cost was calculated for chitosan at pH 3. As it clearly shown that most of the cost is originate from the requirement of pH adjustment. Pollutant removal may be the major criteria for the selection of appropriate coagulant, pH adjustment should not be excluded. Nevertheless, sludge disposal costs were excluded in this study, therefore this situation should also be considered for total cost.

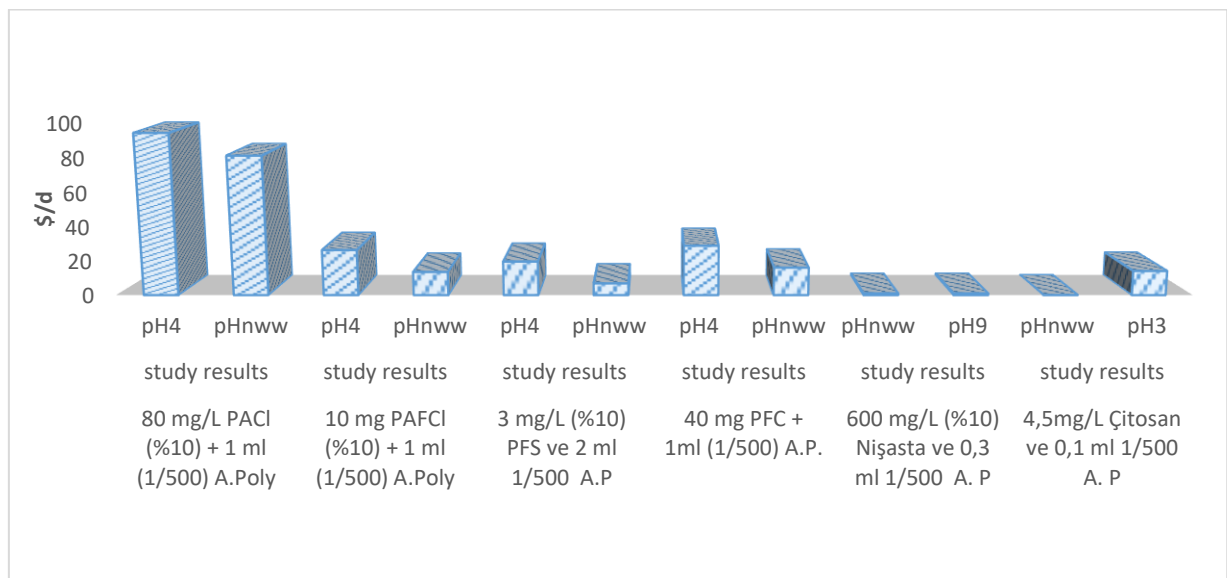


**Figure 7:** Comparative Coagulant Cost.

### CONCLUSION

The effectiveness of various novel pre-hydrolysing coagulants (PACI, PAFCI, PFS and PFCI) for the treatment of textile wastewater have been studied in this study. Chitosan as a biological cationic polymer and as a natural coagulant, has also been investigated for textile wastewater. The results of this study may be drawn as follows:

- Maximum colour removal (97%) was obtained with PAFCI at pH 4, while PFCI gave the minimum colour removal (23%) at same pH. Chitosan yielded the second maximum colour removal as 88% at pH 3. 55% and 56 % COD removal was obtained at pH 4 and pH 3 for PAFCI and chitosan, respectively.

- Maximum COD removal (67%) was obtained with PFS and PFCI, at pH<sub>nww</sub> and pH 4, respectively.
- It was shown that PACI, PAFCI, PFS and chitosan caused considerably lower sludge production. It has been found that as novel pre-hydrolysed and natural coagulant materials, PAFCI and chitosan are the best coagulants in terms of colour removal for investigated textile wastewater. Both of these coagulant are able to provide the receiving bodies discharge standards (for colour and COD removal efficiencies determined in Turkish regulations) at both natural and adjusted pH samples, like reported in the literature for textile wastewaters. Sludge production rates were measured for these coagulants as 60 kg/d and 24 kg/d, respectively. PFS gave minimum sludge production (14 kg/d) at pH<sub>nww</sub>, while maximum sludge production was observed with starch (560 kg/d) at pH 9.
- According to the economic analysis results, the best colour efficiency were found as 97% with PAFCI and the second best colour removal were found as 88% with Chitosan. Due to lower sludge production than PAFCI and lower chemical costs; Chitosan can be assessed as the optimum chemical for this wastewater.
- When the operating cost is evaluated on the basis of daily coagulant requirement, PACI gave the maximum cost at pH 4. Minimum daily coagulant cost obtained as 0,01 \$/d with chitosan for pH<sub>nww</sub>. PAFCI gave 14 \$/d at natural wastewater pH.
- So, in the future, it is necessary to evaluate the cost of residual sludge disposal of both coagulants in order to be able to decide the most suitable colour removal method for investigated wastewater.

## ACKNOWLEDGEMENT

This paper was produced by associated with a Msc. Thesis titled as 'Determination of the best available coagulation/flocculation technologies for colour removal from a treated textile industrial wastewater originated from the processes including indigo fabric washing together with cotton fabric dyeing' funded by the Scientific Research Council of Namık Kemal University via Grant No. NKU BAP.00.17.YL.14.02

## REFERENCES

1. Yıldız Töre G, Çelik S.Ö, Gürkan R, Kırhan Sesler Ş. Determination of the Best Available Coagulation/Flocculation Technology with novel pre-hydrolysed coagulants for colour removal from biologically treated textile wastewater. Journal of Selçuk University. 2014; 1-12.

2. Robinson T, McMullan G, Marchant R, Nigam P. Remediation of dyes in textile effluent: a critical review on current treatment technologies with a proposed alternative. *Bioresource Technology*. 2001; 77: 247–255.
3. Shin C.H. and Bae J.S. A stability study of an advanced co-treatment system for dye wastewater reuse. *J. Ind. Eng. Chem.* 2012; 18: 775–779.
4. Akshaya K.V, Rajesh R. D, Puspendu B. A review on chemical coagulation/flocculation technologies for removal of colour from textile wastewaters. *Journal of Environmental Management*. 2012; 93: 154-168.
5. Mohammed A.D, Hendriks J. Effective Removal of Heavy Metal Ions Using Glycerol and Starch Xanthate. *JOTCSA*. 2017; 4(3): 1031-1044.
6. Jiang J.Q. and Graham N.J.D. Pre-polymerised inorganic coagulants and phosphorus removal by coagulation-a review. *Water SA*. 1998; 24: 237-244.
7. Gregory J, Rossi L. Dynamic testing of water treatment coagulants. *Water Science and Technology*. 2001; 1: 65-72.
8. Gao B, Yue Q, Miao J. Evaluation of polyaluminium ferric chloride (PAFC) as a composite coagulant for water and wastewater treatment. *Water Science and Technology*. 2001; 47 (1): 127-132.
9. Wang X, Zeng G, Zhu, J. Treatment of jean-wash wastewater by combined coagulation, hydrolysis/acidification and Fenton oxidation. *J Hazard Mater*. 2008;153(1-2):810-6.
10. Wang R.M, Wang Y, He Y.F, Li F.Y, Zhou Y, He N.P. Preparation of solid composite polyferric sulfate and its flocculation behavior for wastewater containing high concentration organic compounds. *Water Science and Technology*. 2010; 61(11):2749 – 2757.
11. Chen T, Gao B, Yue Q, 2010. Effect of dosing method and pH on colour removal performance and floc aggregation of polyferricchloride-polyaminedualcoagulant in synthetic dyeing wastewater treatment. *Colloids and Surface A: Physicochemical and Engineering Aspects*. 2010; 355: 121-129.
12. Wei J, Gao B, Yue Q, Wang, Y. Effect of dosing method on colour removal performance and flocculation dynamics of polyferric-organic polymer dual-coagulant in synthetic dyeing solution. *Chemical Engineering Journal*. 2009; 151 (1–3):176-182.
13. Hascakir B, Utilization Of Natural Polyelectrolytes In Wastewater Treatment. İzmir. Master thesis. Graduate School of Natural and Applied Sciences of Dokuz Eylül University. 2003.
14. Sanghi R. and Bhattacharya B. Comparative evaluation of natural polyelectrolytes psyllium and chitosan as coagulant aids for decolourisation of dye solutions. *Water Quality Research Journal of Canada*. 2005; 40: 97-101.
15. Ganjidoust H, Tatsumi K, Yamagishi T, Gholian RN. Effect of synthetic and natural coagulant on lignin removal from pulp and paper wastewater. *Wat. Sci. Technol*. 1997; 35: 291–296.

16. Rodrigues AC, Boroski M, Shimada NS, Garcia JC, Nozaki J, Hioka N. Treatment of paper pulp mill wastewater by coagulation– flocculation followed by heterogenous photocatalysis. *J. Photochem Photobiol A Chem.* 2008; 194: 1–10.
17. Wang JP, Chen YZ, Ge XW, Yu HQ. Optimization of coagulation– flocculation process for a paper-recycling wastewater treatment using response surface methodology. *Colloids Surf A Physicochem Eng Aspects.* 2007; 302: 204–210.
18. Jincheng Wei, A, Baoyu G, Qinyan Y, Yanfstarch W. Effect of dosing method on colour removal performance and flocculation Dynamics of polyferric-organic polymer dual-coagulant in synthetic dyeing solution. *Chemical Engineering Journal.* 2009; 151: 176–182.
19. Tun L.L, Baraoidan W.A, Gaspillo P.D, Suzuki M. A study on the relative performance of different coagulants and the kinetics of COD in the treatment of a textile bleaching and dyeing industrial wastewater. *ASEAN Journal of Chemical Engineering.* 2007; 7: 49-60.
20. Szyguła A, Guibal E, Ariño Palacín M, Ruiz M, Sastre AM. Removal of an anionic dye (Acid Blue 92) by coagulation-flocculation using chitosan. *J Environ Manage.* 2009 J;90(10):2979-86.
21. Mahmoodi NM, Salehi R, Arami M, Bahrami H. Dye Removal from Coloured Textile Wastewater Using Chitosan in Binary Systems. *Desalination.* 2011; 267(1): 64-72.



## FENTON-LIKE OXIDATION OF REACTIVE BLACK 5 IN THE PRESENCE OF $\text{LaBO}_3$ (B: Fe, Co, Mn, Ni) PEROVSKITE CATALYSTS

Burcu Palas<sup>1\*</sup>, Gülin Ersöz<sup>2</sup> and Süheyda Atalay<sup>3</sup>

1,2,3. Ege University, Department of Chemical Engineering, İzmir, TURKEY

*(This article first appeared in PPM2017 and was accepted as a non-peer-reviewed manuscript to be published in JOTCSA)*

**Abstract:** The catalytic performances of  $\text{LaBO}_3$  (B: Fe, Co, Mn, Ni) perovskite catalysts in Fenton-like oxidation of the textile dye, Reactive Black 5 were compared, and, the optimum reaction conditions were investigated in the presence of the most efficient catalyst. Reactive Black 5 was selected as the model dye due to its complex chemical structure, high water solubility and common usage in the textile industry. The performances of the catalysts in Reactive Black 5 degradation and decolorization were compared by testing different catalyst loadings. According to the catalyst screening experiments,  $\text{LaFeO}_3$  showed the highest catalytic performance whereas  $\text{LaCoO}_3$ ,  $\text{LaMnO}_3$ , and,  $\text{LaNiO}_3$  were not effective in the degradation and decolorization of Reactive Black 5. A parametric study was carried out in the presence of  $\text{LaFeO}_3$  catalyst in order to determine the most suitable reaction conditions. In the parametric study, the effect of catalyst loading, pH and the initial  $\text{H}_2\text{O}_2$  concentration were investigated. The initial dye concentration and the reaction temperature were kept constant at 100 ppm and  $50^\circ\text{C}$ , respectively. The most suitable reaction conditions were determined as 0.1 g/L of catalyst loading, 3 and 1 mM of  $\text{H}_2\text{O}_2$ , and, 96.9% degradation, and complete decolorization were achieved under these conditions.

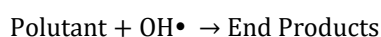
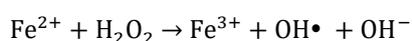
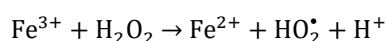
**Keywords:** Reactive Black 5, Fenton-like oxidation, Perovskite catalysts.

**Cite this:** Palas B, Ersöz G, Atalay S. FENTON-LIKE OXIDATION OF REACTIVE BLACK 5 IN THE PRESENCE OF  $\text{LaBO}_3$  (B: Fe, Co, Mn, Ni) PEROVSKITE CATALYSTS. JOTCSA. 2017;5(sp. is. 1):37-44.

**\*Corresponding author.** E-mail: [burcu.palas@ege.edu.tr](mailto:burcu.palas@ege.edu.tr).

## INTRODUCTION

Textile dyes are one of the most commonly used organic compounds constituting a threat to the environmental health. A remarkable fraction of the dyes is nonfixed during the dyeing process and released into the textile effluents [Akpan and Hameed, 2009]. Most of the conventional wastewater treatment methods generate great amounts of sludge and solid waste which need further treatment before disposal. Advanced oxidation process including the Fenton-like oxidation is one of the most environmentally friendly and effective method for the degradation of the dyes. The following Fenton like reactions are proposed for the formation of hydroxyl radicals and the removal of industrial pollutants [Sun *et al.*, 2007]:



In the literature, there are many studies on decolorization of textile dyes by Fenton like oxidation. However, neither of these studies focused on the comparison of the catalytic performances of the Lanthanum based perovskite type of catalysts in Fenton like oxidation of textile dyes. Therefore, this study has an innovative approach due to the investigation of the Fenton like oxidation performances of perovskites in both of the degradation and decolorization of textile dyes. In this regard, the main objective of this study is the removal of the reactive azo dye, Reactive Black 5 (RB5) by Fenton-like oxidation in the presence of perovskite type of catalysts. The perovskite catalysts have been attracted interest due to their thermal stability, high oxidation activity, and inexpensive prices [Labhassetwar *et al.*, 2015]. In the context of this study, four types of Lanthanum based perovskites ( $\text{LaFeO}_3$ ,  $\text{LaCoO}_3$ ,  $\text{LaNiO}_3$ ,  $\text{LaMnO}_3$ ) were prepared by sol-gel citrate method and their catalytic performances were compared. The most suitable reaction conditions were also determined in the presence of the selected perovskite catalyst.

## EXPERIMENTAL

### Catalyst Preparation

Four types of Lanthanum based perovskite catalysts including  $\text{LaFeO}_3$ ,  $\text{LaNiO}_3$ ,  $\text{LaCoO}_3$ , and  $\text{LaMnO}_3$  were prepared by sol-gel citrate method. Equimolar amounts of  $\text{La}(\text{NO}_3)_3 \cdot 6\text{H}_2\text{O}$  and the transition metal nitrate were dissolved in distilled water. Excess amount of citric acid was added into the mixture of lanthanum nitrate and metal nitrate in order to form a cross linked structure. The mole of citric acid was equal to 3/2 times of the summations of moles of metal nitrates. The mixture is heated at 80-90°C under vigorous stirring until the gel form was obtained. The gel was dried at 150°C for 6 h and calcined at 750°C for 5 h to remove the nitrates.

### Experimental Set-up and Procedure

The experiments were carried out in 250 mL three necked volumetric flasks for 2 hours using a temperature controlled hot-plate. dye solutions of 100 ppm were prepared and the pH was adjusted to the desired value using diluted H<sub>2</sub>SO<sub>4</sub> or NaOH solutions. When the temperature reached the set value, certain amounts of catalyst and hydrogen peroxide were added into the reaction medium. Samples were taken periodically to analyze the degradation and the decolorization efficiencies.

### Experiments

In order to determine which perovskite catalyst showed the highest catalytic performance on Fenton like oxidation of RB5, catalyst screening experiments were performed. In these experiments, the initial dye concentration, the initial H<sub>2</sub>O<sub>2</sub> concentration and the initial pH were fixed at 100 ppm, 4 mM and 3, respectively, while the catalyst loading and the reaction temperature were between 0.25-0.5 g/L and 50-70 °C, respectively. A parametric study was carried out in the presence of the selected catalyst to investigate the effect of the catalyst loading, initial pH and the initial H<sub>2</sub>O<sub>2</sub> concentration on Reactive Black 5 removal.

### Analysis

The decolorization and degradation efficiencies of Reactive Black 5 were analyzed by using a UV-VIS spectrophotometer. The absorbance values of the samples were measured at 390 and 597 nm which were associated with the degradation of the aromatic part and color removal, respectively. The spectrum of the Reactive Black 5 was presented in Figure 1.

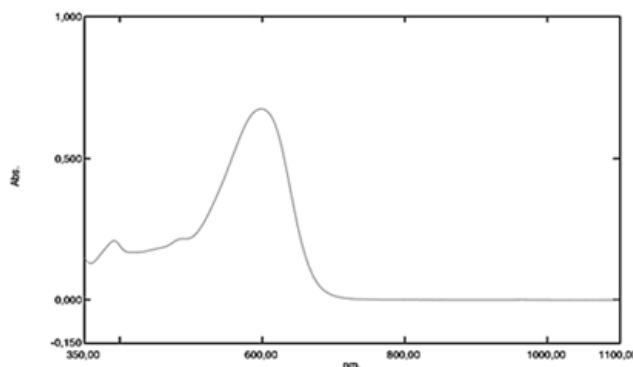


**Figure 1:** UV-Vis spectrum of the Reactive Black 5.

The decolorization and degradation efficiencies were calculated using the following equation:

$$\%Degradation = \left[ \frac{A_0|_{@390 \text{ nm}} - A_t|_{@390 \text{ nm}}}{A_0|_{@390 \text{ nm}}} \right] \times 100$$

$$\%Decolorization = \left[ \frac{A_0|_{@597 \text{ nm}} - A_t|_{@597 \text{ nm}}}{A_0|_{@597 \text{ nm}}} \right] \times 100$$

where  $A_0$  is the initial absorbance,  $A_t$  is the absorbance at time  $t$ .

## RESULTS AND DISCUSSION

### Catalyst Screening

The Fenton like oxidation performances of  $\text{LaBO}_3$  (B: Fe, Mn, Ni, Co) catalysts were assessed under various reaction conditions and the results are shown in Figure 2.

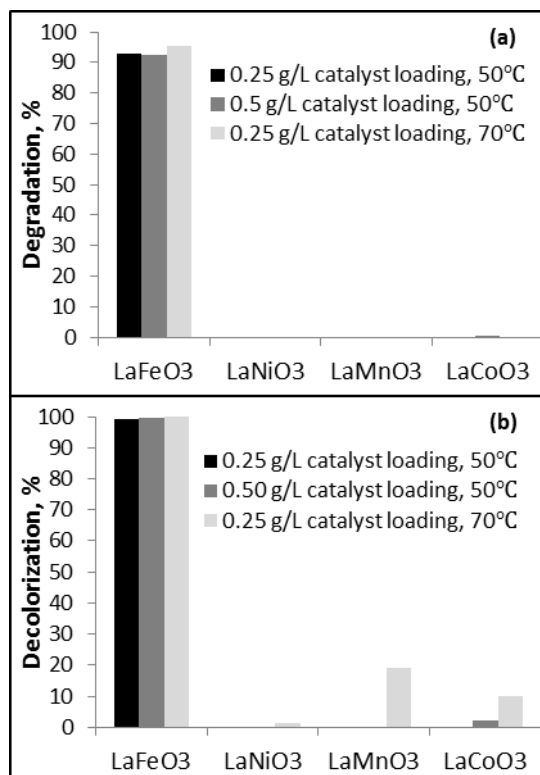


**Figure 2:** Comparison of the catalytic performances of the perovskites at various catalyst loading and temperature values. Reaction conditions:  $[\text{RB5}]_0=100$  ppm,  $\text{pH}=3$ ,  $[\text{H}_2\text{O}_2]_0=4$  mM.

According to the catalyst screening results, degradation could not be achieved in the presence of  $\text{LaMnO}_3$ ,  $\text{LaNiO}_3$  and  $\text{LaCoO}_3$  whereas the decolorization efficiencies were below 20% even at high reaction temperatures. Nevertheless,  $\text{LaFeO}_3$  was very effective in both degradation and decolorization of Reactive Black 5 under all the reaction conditions tested. Almost complete decolorization was accomplished and the degradation efficiencies were above 92% in the presence of  $\text{LaFeO}_3$ . Similarly, Taran *et al.* concluded that  $\text{LaMnO}_3$ ,  $\text{LaNiO}_3$  and  $\text{LaCoO}_3$  catalysts were ineffective in Fenton-like oxidation of an organic pollutant whereas high degradation rates were accomplished in the presence of  $\text{LaFeO}_3$  and  $\text{LaCuO}_3$  [Taran *et al.*, 2016]. The most suitable reaction conditions were determined in the parametric study by using  $\text{LaFeO}_3$  catalyst since it was remarkably more effective than the other perovskites.

## Parametric Study

### Effect of the catalyst loading

The influence of the catalyst loading on RB5 removal was investigated in the presence of  $\text{LaFeO}_3$  by varying the catalyst loading between 0.1 and 0.5 g/L. Additionally a set of experiments were performed in the absence of catalyst. The results are presented in Figure 3. The results showed that the presence of catalyst was crucial for dye degradation. Only 21.9% decolorization was achieved and no degradation was accomplished in the absence of catalyst. As the catalyst loading increased the dye removal rates were enhanced due to the availability of more catalyst active sites resulting in acceleration of the hydroxyl radical production on the catalyst surface [Gan and Li, 2013]. Additionally, the decolorization rates are faster than the degradation rates since nitrogen double bonds are degraded more easily when compared to the aromatic rings [Wu *et al.*, 2008]. Though the highest degradation and decolorization rates were achieved by using 0.5 g/L of catalyst loading, 0.1 g/L could be proposed as the most suitable loading since nearly the same dye removal efficiencies were obtained at the end of the oxidation reaction.

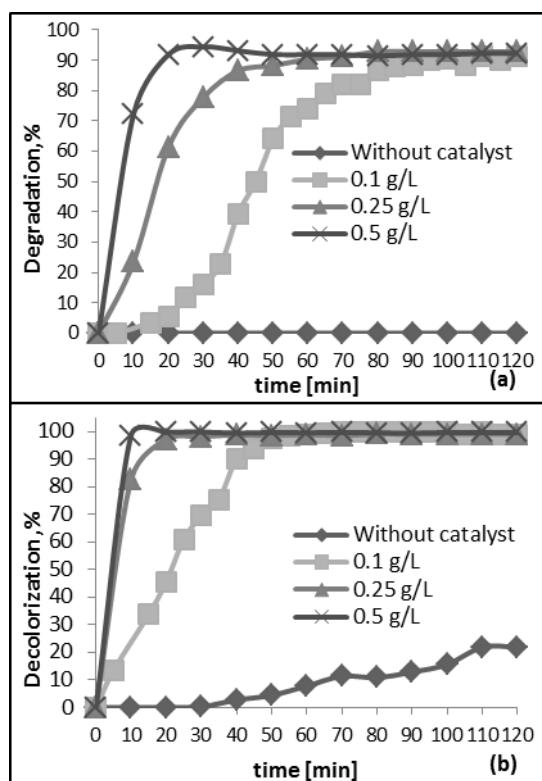


**Figure 3:** Influence of the catalyst loading on RB5 degradation (a) and decolorization (b).

Reaction conditions:  $[\text{RB5}]_0 = 100$  ppm,  $\text{pH} = 3$ ,  $[\text{H}_2\text{O}_2]_0 = 4$  mM,  $T = 50^\circ\text{C}$ .

### Effect of the initial pH

The impact of the initial pH on the degradation and decolorization of RB5 was studied under pH 3, 4, 5 and 7, and the results are shown in Figure 4.

Figure 4 depicts that both of the degradation and decolorization efficiencies diminished with the increasing pH. When the initial pH was set 4, only 6.6% degradation and 31% decolorization was achieved. Above pH 4, the dye removal efficiencies were approximately zero. The hydroxyl radicals are generated efficiently under acidic conditions since at lower pH the catalyst surface is positively charged [Panda *et al.*, 2011] which enhances the adsorption of the negatively charged RB5 molecules. pH 3 was selected as the most suitable initial pH value since the highest RB5 removal occurred at this pH.

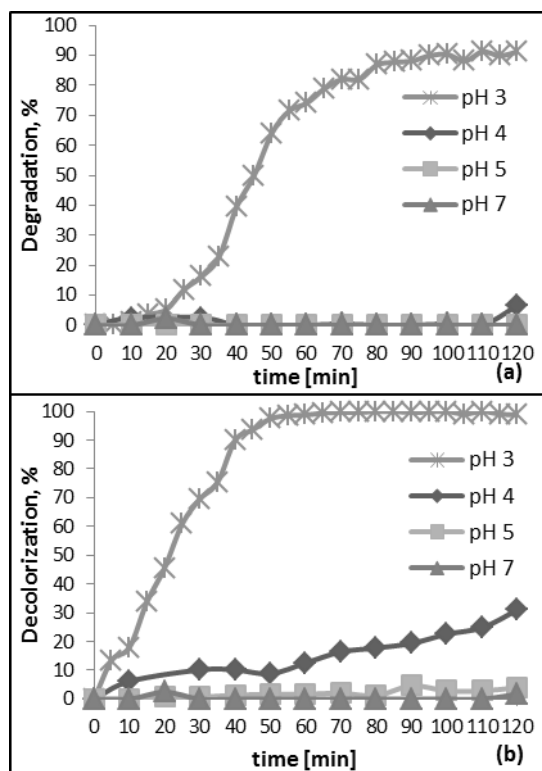


**Figure 4:** Influence of the initial pH on RB5 degradation (a) and decolorization (b). Reaction conditions:  $[RB5]_0=100$  ppm, 0.1 g/L of catalyst loading,  $[H_2O_2]_0=4$  mM,  $T=50^\circ C$ .

#### *Effect of the initial hydrogen peroxide concentration*

The role of the initial  $H_2O_2$  concentration on dye removal was investigated by changing the oxidant concentration between 0.5 and 4 mM. In addition, a set of experiments was performed without using  $H_2O_2$ . The dye degradation and decolorization profiles obtained at different  $H_2O_2$  concentrations are presented in Figure 5.

According to Figure 5, the presence of the  $H_2O_2$  was essential for an efficient Fenton-like oxidation because neither degradation nor decolorization was observed in the absence of the oxidant. As the oxidant concentration was increased from 0.5 to 1 mM the dye removal was improved significantly. However, a further increase in  $H_2O_2$  concentration (up to 4 mM) decreased the dye removal efficiencies remarkably due to the scavenging effect resulting from the reaction between the excess  $H_2O_2$  molecules and the hydroxyl radicals [Kasiri *et al.*, 2008]. Therefore, 1 mM oxidant concentration was determined as the optimum condition.

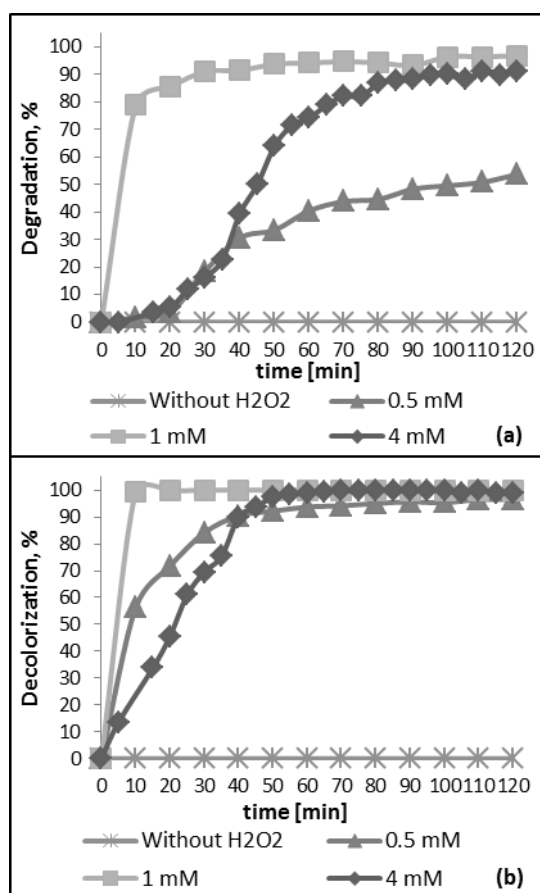


**Figure 5:** Influence of the initial hydrogen peroxide concentration on RB5 degradation (a) and decolorization (b). Reaction conditions:  $[RB5]_0=100$  ppm, 0.1 g/L of catalyst loading, pH=3,  $T=50^\circ\text{C}$ .

## CONCLUSIONS

The textile dye, Reactive Black 5, was effectively degraded and decolorized by the Fenton-like oxidation in the presence of  $\text{LaFeO}_3$  perovskite catalyst which showed the highest catalytic performance among the  $\text{LaBO}_3$  (B: Fe, Co, Mn, Ni) perovskites.

The most suitable reaction conditions were determined as 0.1 g/L of catalyst loading, 3 and 1 mM of  $\text{H}_2\text{O}_2$  when the initial dye concentration and the reaction temperature were 100 ppm and  $50^\circ\text{C}$ , respectively. Under the most suitable reaction conditions, 96.9% degradation and complete decolorization were achieved in 2 hours of reaction time.

## ACKNOWLEDGMENT

This study was supported by Ege University Scientific Research Project Fund [15-MUH-030].

## REFERENCES

- Akpan, U.G. and Hammed, B.H., 2009. Parameters affecting the photocatalytic degradation of dyes using TiO<sub>2</sub>-based photocatalyst, *J. Hazard. Mater.*, 170, 520.
- Gan, P.P., Li and S.F.Y., 2013. Efficient removal of Rhodamine B using a rice hull-based silica supported iron catalyst by Fenton-like process, *Chem. Eng. J.*, 229, 351.
- Kasiri, M.B., Aleboyeh, H. and Aleboyeh, A., 2008. Degradation of Acid Blue 74 using Fe-ZSM5 zeolite as a heterogeneous photo-Fenton catalyst, *Appl. Catal. B: Environ.*, 84(1-2), 9.
- Labhasetwar, N., Saravanan, G., Megarajan, S.K., Manwar, N., Khobragade, R., Doggal, P. and Grasset. F., 2015. Perovskite-type catalytic materials for environmental applications, *Sci. Technol. Adv. Mater.*, 16, p. 036002, 13 pp.
- Panda, N., Sahoo, H. and Mohapatra S., 2011. Decolourization of Methyl Orange using Fenton-like mesoporous Fe<sub>2</sub>O<sub>3</sub>-SiO<sub>2</sub> composite, *J. Hazard. Mater.*, 185, 359.
- Sun, J.H., Sun, S.P., Wang, G.L. and Qiao, L.P., 2007, Degradation of azo dye Amido black 10B in aqueous solution by Fenton oxidation process, *Dyes Pigm.*, 74, 647.
- Taran, O.P., Ayusheev, A.B., Ogorodnikova, O.L., Prosvirin, I.P., Isupova, L.A. and Parmon, V.N., 2016. Perovskite-like catalysts LaBO<sub>3</sub> (B = Cu, Fe, Mn, Co, Ni) for wet peroxide oxidation of phenol, *Appl. Catal. B: Environ.*, 180, 86.
- Wu, C.-H., Kuo, C.-Y. and Chang, C.-L., 2008. Decolorization of C.I. Reactive Red 2 by catalytic ozonation processes, *J. Hazard. Mater.*, 153 1052.



## **NANO ZINC BORATE AS A LUBRICANT ADDITIVE**

**Sevdiye Atakul Savrik<sup>1</sup>, Burcu Alp<sup>1</sup>, Fatma Ustun<sup>1</sup>, Devrim Balkose<sup>1,a</sup>**

1 İzmir Institute of Technology Department of Chemical Engineering  
Gulbahce Urla Izmir Turkey

*(This article first appeared in PPM2017 and was accepted as a non-peer-reviewed manuscript to be published in JOTCSA)*

**Abstract:** Lubricants consist of base oils and chemical additives such as dispersants, surfactants, oxidation inhibitors, and antiwear agents. Organic and inorganic boron-based additives increase wear resistance and decreases friction. Hexagonal boron nitride and metal borates are used for this purpose. Zinc borate is a synthetic hydrated metal borate. The production techniques of zinc borate generally include the reaction between zinc source materials (zinc oxide, zinc salts, zinc hydroxide) and the boron source materials (boric acid and borax). The nano zinc borate particles were prepared from zinc nitrate and borax in the present study by using low initial zinc and borate concentrations and low temperature to prevent particle growth. The templates span 60 and PEG 4000 were used to control the particle size. The particles were separated from mother liquor by centrifugation, washed with ethanol, dried and ground and used as additive to base oil. The particles have H<sub>2</sub>O and B(3)-O vibrations in their FTIR spectra. The empirical formula of the nanoparticles was approximately 3ZnO.2B<sub>2</sub>O<sub>3</sub>.4H<sub>2</sub>O from EDX and TGA analysis. X-ray diffraction diagram indicated the particles were in amorphous state. When the nanoparticles were added to light neutral oil the wear scar diameter and friction coefficient was lowered 50% and 20% respectively.

**Keywords:** Base oil, nano zinc borate, lubricant additive.

**Cite this:** Atakul Savrik S, Alp B, Ustun F, Balkose D. NANO ZINC BORATE AS A LUBRICANT ADDITIVE. JOTCSA. 2017;5(sp. is. 1):45–52.

**\*Corresponding author.** E-mail: [devrimbalkose@gmail.com](mailto:devrimbalkose@gmail.com).

## **INTRODUCTION**

Numerous studies have been carried out in recent years on the effects of various metal borate particles as lubricating oil additives on wear and friction [Hu and Dong, 1998; Hu et al., 2000]. Their effectiveness can be related to the formation of a borate glass as a tribochemical film or the deposition of particles on the rubbing surface [Varlot et al., 2001]. The friction reduction and anti-wear behaviors are dependent on the characteristics of nanoparticles, such as size, shape, and concentration.

Zinc borate is a synthetic hydrated metal borate. There are various kinds of crystalline hydrated zinc borate. In these products,  $B_2O_3/ZnO$  mole ratios change from 0.25 to 5 and it determines the characteristics of product. The production techniques of zinc borate generally include the reaction between zinc source materials (zinc oxide, zinc salts, zinc hydroxide) and the boron source materials (boric acid and borax) [Eltepe et al., 2007].

Nanoparticles of zinc borate are a requirement for their use as a lubricant additive. Synthesis of nano particles of zinc borate in inverse emulsions in lubricating oil was possible [Savrik et al, 2011]. Nanoparticle formation by supercritical carbon dioxide ( $CO_2$ ) drying of zinc borate species was investigated to evaluate possible chemical modifications in the product during the drying [Gonen et al, 2010]. Nanometer crystal zinc borate with a particle size of 20–50 nm was prepared using the ethanol supercritical fluid drying technique [Dong and Hu, 1998]. Supercritical ethanol drying of zinc borate species to obtain nanoparticles was also investigated by Gonen et al [2011]. It was found that from zinc borates, zinc oxide and boric acid were formed [Gonen et al, 2011]. A nano-flake-like zinc borate  $2ZnO.2B_2O_3.3H_2O$  was prepared via coordination of homogeneous precipitation method using ammonia, zinc nitrate and borax as raw materials [Ting et al, 2009]. The crystal and hydrophobic zinc borate  $Zn_2B_6O_{11}.H_2O$  nanodiscs and nanoplatelets were successfully prepared by a wet method using  $Na_2B_4O_7.10H_2O$  and  $ZnSO_4.7H_2O$  as raw materials *in situ* aqueous solution, and oleic acid as the modifying agent. It had been found that the as-prepared materials displayed nanodisc morphology with average diameters from 100 to 500 nm and the thicknesses about 30 nm [Tian et al, 2006].

The production and characterization of nano particles of hydrated zinc borate for lubrication was aimed at in the present study. Dilute solutions of borax and zinc nitrate were mixed instantly at room temperature to avoid particle growth and hydrosols were formed. The particles were separated by centrifugation and washed with ethanol and dried at 25 °C under vacuum.

## **EXPERIMENTAL**

Anhydrous borax (Sigma Aldrich), zinc nitrate hexahydrate ( $\text{Zn}(\text{NO}_3)_2 \cdot 6\text{H}_2\text{O}$ ) (Sigma-Aldrich), light neutral oil (TUPRAŞ A.Ş), and sorbitan monostearate (Span 60, Sigma-Aldrich), PEG 4000 (Merck) were used in the preparation of hydrated zinc borate nanoparticles and lubricants.

50 cm<sup>3</sup> of 0.1 mol dm<sup>-3</sup> sodium borate solution was added instantly to 50 cm<sup>3</sup> of 0.1 mol dm<sup>-3</sup> zinc nitrate solution and mixed at 600 rpm for 2 hours at ambient temperature of 23 °C. Experiments were repeated by adding 1 cm<sup>3</sup> of 0.002 M span 60 and 1 cm<sup>3</sup> of 0.4 g PEG 4000 in 100 cm<sup>3</sup> to the mixtures. While hydrosols have been mixed, their temperature and pH values were recorded. Since the particles passed through the Whatman filter paper, they were separated from the aqueous phase by centrifugation. They were separated by centrifugation using Rotofix 32 centrifuge at 2000 rpm for 10 minutes, washed with ethanol and centrifuged again at 2000 rpm for 10 minutes. The gelatinous precipitates were dried under vacuum at 10 kPa for 18 hours at 25°C to obtain nanoparticles. Since the nanoparticles were in an agglomerated state they were ground in a porcelain mortar and pestle before use.

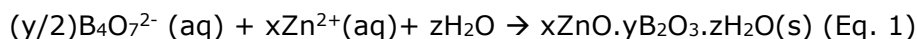
The morphologies of the samples were examined using QUANTA 250F Scanning Electron Microscope (SEM). EDX analysis was carried out using the same instrument. The particle size of the powders were measured by Malvern 2000 zetasizer. X-ray diffraction diagrams were obtained by Phillips x'pert pro X-ray diffractometer employing Ni-filtered Cu K<sub>α</sub> radiation. FTIR spectra of the samples were taken with SHIMADZU FTIR-8400S using KBr disc technique. TG analysis was performed by using SETARAM labsys TGA to determine changes in weight with heating under nitrogen flow at 40 cm<sup>3</sup> min<sup>-1</sup> rate and at a heating rate of 10 °C min<sup>-1</sup> up to 600 °C.

25 cm<sup>3</sup> of light neutral oil, 0.25 g of Span 60 and 0.25 g of the nanoparticles of zinc borate with Span 60 were mixed thoroughly at 600 rpm rate and at 160 °C for one hour on a magnetic hot plate (Ika RH Digital KT/C) and left to cool down to room temperature by continuous stirring. A four ball tester (Ducom) was used to determine the friction coefficient and wear scar diameter. The tests were performed according to ASTM D 4172-94 at 392 N and the test duration was 1 h at 75 °C. The upper ball was rotated at 1200 rpm. Test balls were made from AISI standard steel No. E-52100 and had 12.7 mm diameter. Microphotographs of the wear scars of the three fixed and one rotating test balls were taken by using Olympos BX 60 equipped with Canon Powershot 590IS camera.

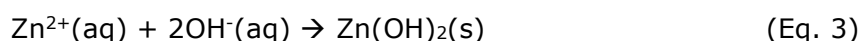
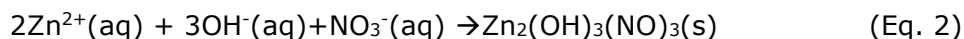
The visible spectrum of base oil separated by centrifugation from base oil was taken by using Perkin Elmer UV-Vis spectrophotometer by using base oil without any additive as thereference.

**RESULTS AND DISCUSSION****Reaction of aqueous borax and zinc nitrate solutions**

The zinc borate precipitation reaction is expected to occur as given in Equation 1



There are other simultaneous reactions in the reaction medium, such as

**Functional groups by FTIR spectroscopy and TG analysis**

The FTIR spectra of the samples without any template and with templates span 60 and PEG 4000 are very similar to each other as seen in Figure 1. There is a broad peak at  $3358 \text{ cm}^{-1}$  due to hydrogen-bonded O-H group vibrations. Asymmetric B(3)-O vibrations were observed at  $1383 \text{ cm}^{-1}$  and at  $1350 \text{ cm}^{-1}$ . H-O-H bending vibration was observed at  $1624 \text{ cm}^{-1}$ . At  $1014 \text{ cm}^{-1}$  a peak for symmetric B(3)-O vibration was present. Out of plane bending vibration of B(3)-O gave a small peak at  $694 \text{ cm}^{-1}$ .

TG curves of the samples were very similar to each other as depicted in Figure 2.

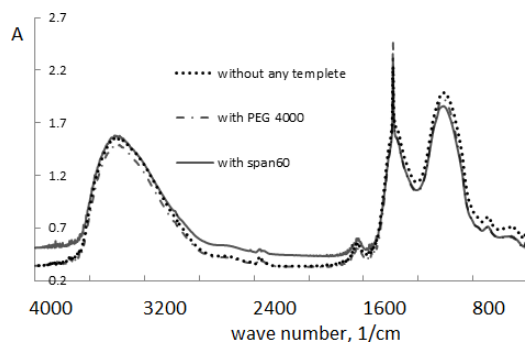


**Figure 1:** FTIR spectra of the zinc borates.

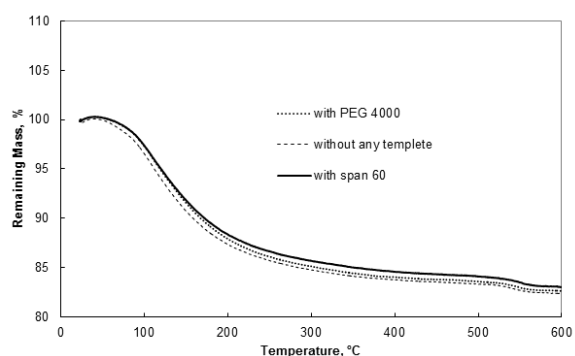


**Figure 2:** TG curves of the zinc borates.

On heating the samples only water is eliminated from the samples. All the samples contained very similar amount of water, around 17 % . The total amount of water was less than the zinc borate samples prepared from at higher initial borax and zinc nitrate concentrations. Savrik [2010] has determined the samples prepared at 70°C from 1 mol dm<sup>-3</sup> initial concentration contained around 20.6 % water with the same FTIR spectra of the samples in the present study.

### **Chemical Analysis by Energy Dispersive X-ray Spectroscopy (EDX)**

The energy dispersive spectroscopy was used to determine the elemental composition of zinc borates. The EDX spectrum of the samples are very similar for each zinc borate. The EDX spectrum of zinc borate with span 60 template is seen in Figure 3.

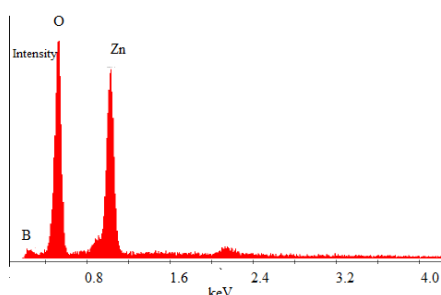


**Figure 3:** EDX spectrum of the zinc borate with span 60.

The chemical composition of the samples are similar to each other. The empirical formula of the nanoparticles was approximately 3ZnO.2B<sub>2</sub>O<sub>3</sub>.4H<sub>2</sub>O from EDX analysis. However it could be a mixture of zinc borate and zinc hydroxide due to parallel reactions.

### **Morphologies of the powders**

The SEM micrographs of the dried samples are shown in Figure 4. The dried powders consisted of agglomerates of primary particles of 40 nm, 50 nm and 80 nm for samples without template, with span 60 and with PEG 4000 respectively. The particles were attracted to each other due to capillary forces during drying. Water in the wet samples was replaced with ethanol which has a lower surface tension to decrease the attractive forces between the particles due to capillarity. However they were also agglomerated even drying of the ethanolic hydrogel.

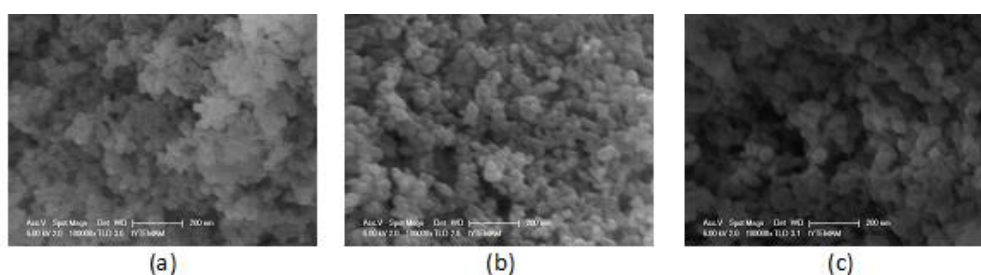


**Figure 4:** SEM micrograph of the sample a. without template b. with span 60 c. with PEG 4000.

### **Particle Size Distribution of the initially formed hydrated zinc borates in solution**

The size distribution of particles were monodisperse with number average sizes of 35.3 nm and 234 nm respectively for zinc borates without any template and with span 60 respectively. However the particle size distribution of particles with PEG 4000 were bidisperse, the average size was 228.5 nm and 969.7 nm for 94.6% and 5.4 % of the particles. While the primary particles were dispersed in zinc borate without any template, these particles were agglomerated in the presence of surface active agents span 60 and PEG 4000.

### **X-ray Diffraction Analysis (XRD)**

Only a broad peak are observed at  $2\theta$  value of  $28^\circ$  in X-ray diffraction diagram of the samples indicating that they were amorphous. The small size of the crystals formed in the present study caused broadening of the diffraction lines . The crystal growth occurs in time at high temperature and at high initial concentration and an x-ray diagram with sharp diffraction peaks is obtained. Savrik *et al.* [2011] obtained sharp diffraction peaks for zinc borate obtained from  $1 \text{ mol dm}^{-3}$  initial concentrations at  $70^\circ\text{C}$  in two hours. Diffraction peaks for  $\text{Zn}(\text{B}_3\text{O}_3(\text{OH})_5)\text{H}_2\text{O}$  (JPDS PDF File Number 721789) were observed by Savrik *et al.*[ 2011].

### **The precipitates as lubricant additives**

Previous studies also had shown the lowering of the friction coefficient when zinc borate nanoparticles were added to the base oil [Dong and Hu, 1998, Tian et al, 2006]. The results of the four ball tests are shown for the lubricating oil prepared in the present study. The wear scar diameter for ball 1, 2 and 3 are  $662 \mu\text{m}$ ,  $704 \mu\text{m}$  and  $701 \mu\text{m}$  respectively. The average wear scar diameter was  $689 \mu\text{m}$ .

The change of the friction coefficient with time during the test is 0.079. The wear scar diameter was lowered from  $1402 \mu\text{m}$  to  $689 \mu\text{m}$  and the friction coefficient was lowered from 0.099 to 0.079 by adding nanozinc borate to light neutral oil. The wear scar diameter and friction coefficient was lowered 50% and 20% respectively. Compared to inverse emulsion case the friction coefficient was 11 % lower, but the wear scar diameter was 15.6 % higher for the nanozinc borate case.

The visible spectrum of the lubricant before and after four ball tests indicated that the yellow color of the oil was darkened during the tests that was made at  $75^\circ\text{C}$ . The absorbance of the lubricating oil at 414 nm increased from 0.06 to 0.84 after the test. This discoloration was due to oxidation and crosslinking reactions in base oil. Thus it is necessary to add antioxidants other than zinc borates to the lubricant to avoid oxidation.

## **CONCLUSIONS**

The nano zinc borate particles were prepared in the present study by using low initial zinc and borate concentrations and low temperature to prevent particle growth. The templates span 60 and PEG 4000 has increases the aggregation state of nanoparticles of zinc borate in their mother liquor. The empirical formula of the nanoparticles was approximately  $3\text{ZnO} \cdot 2\text{B}_2\text{O}_3 \cdot 4\text{H}_2\text{O}$  from EDX analysis. However it could be a mixture of zinc borate and zinc hydroxide. X-ray diffraction diagram indicated the particles were in amorphous state. When the nanoparticles were added to light neutral oil the wear scar diameter and friction coefficient was lowered 50% and 20% respectively. However the oil color was darker after the four ball tests indicating addition of antioxidants is necessary. Further studies should be made in synthesis, characterization of zinc borate nano particles and their use in nanoparticle state as lubricant additives and formulating lubricants.

## **ACKNOWLEDGEMENT**

The authors thank to OPET A.Ş. for four ball tests.

## **REFERENCES**

Dong, J. X. , Hu Z. S., 1998. A study of the anti-wear and friction-reducing properties of the lubricant additive, nanometer zinc borate, *Tribology International* 31(5), 219

Eltepe, H. E, Balkose, D. , Ulku S., Effect of temperature and time on zinc borate species formed from zinc oxide and boric acid in aqueous medium. *Industrial & Engineering Chemistry Research*, 46(8), 2367

Gonen, M. , Balkose, D.,Gupta R., Ulku S.,2010 Supercritical Carbon Dioxide Drying of Methanol-Zinc Borate Mixtures, *Industrial & Engineering Chemistry Research*, 48(14), 6869-6876.

Gonen, M.,Balkose, D. , Ulku, S., 2011 Supercritical ethanol drying of zinc borates of  $2\text{ZnO} \cdot 3\text{B}_2\text{O}_3 \cdot 3\text{H}_2\text{O}$  and  $\text{ZnO} \cdot \text{B}_2\text{O}_3 \cdot 2\text{H}_2\text{O}$ . *Journal of Supercritical Fluids*, 59,43

Hu, Z.S., Dong, J.,X., 1998. Study on Antiwear and Reducing Friction Additive of Nanometer Titanium Borate. *Wear*. 216, 87.

Savrik, S.A., 2010. Enhancement of tribological properties of mineral oil by addition of sorbitan monostearate and zinc borate, PhD Dissertation, Graduate School of Engineering and Sciences of İzmir Institute of Technology

Savrik, S. A, Balkose, D. , Ulku S., 2011. Synthesis of zinc borate by inverse emulsion technique for lubrication, *Journal of Thermal Analysis and Calorimetry*,104(2), 605

Tian, Y. M, Y. P. Guo, Y.P., Man Jiang,M., Ye Sheng, Y., Bala H.,B., Guangyu Z.,G.,Yanqiu J, Y., Bing Z., Z., Yanchao Z.,Y., Zichen W.Z.,2006. Synthesis of hydrophobic zinc borate nanodiscs for lubrication *Materials Letters* 60(20), 2511.

Atakul Savrik S, Alp B, Ustun F, Balkose D. JOTCSA. 2017; 5(sp. is. 1); 45-52. **RESEARCH ARTICLE**

Ting, C., D. Jian-Cheng D., Long-Shuo W., Gang, F., 2009. Preparation and characterization of nano-zinc borate by a new method., *Journal of Materials Processing Technology*, 209(8), 4076

Varlot, K., Kasrai, M., Bancroft, G.M., Yamaguchi, E.S., Ryason, P.R., Igarashi, J., 2001, X-Ray Absorption Study of Antiwear Films Generated from ZDDP and Borate Micelles. *Wear*. 249, 1029-1035.



## Enhancement of Cerium exchange with Ultrasound

Fehime Çakıcıoğlu-Özkan<sup>\*1</sup>, Yasemin Erten-Kaya<sup>2</sup>,

<sup>1</sup>Izmir Institute of Technology, Department of Chemical Engineering,  
Urla, İzmir, Turkey

<sup>2</sup>General Directorate of İzmir Water and Sewerage Department, Material Available and  
Package Treatment Branch Manager, 35251, İzmir, Turkey

*(This article first appeared in PPM2017 and was accepted as a non-peer-reviewed manuscript to be published in JOTCSA)*

**Abstract:** In this study the effect of ultrasound of the cerium exchange was studied. The results were compared to those obtained from traditional batch exchange method. Contact time, initial cation concentration (fold equivalent excess) and the types of the ultrasound were studied. Ultrasonic probe, which is the most effective method, enhanced the replacement of Na<sup>+</sup> ion with Ce<sup>3+</sup> ion in the extra-framework of zeolite up to 73 % by applying 5 consecutive ion exchanges. The cerium in the solution caused to be formed cerium oxides on the crystal surface occluding the pores. Thus the specific surface area of cerium exchanged zeolite was decreased due to formation of cerium complexes on the surface and into the pores.

**Keywords:** NaX zeolite; Ultrasound; Ion exchange; Characterization.

**Cite this:** Çakıcıoğlu-Özkan F, Erten-Kaya Y. Enhancement of Cerium exchange with Ultrasound. JOTCSA. 2017;5(sp. is. 1):53–64.

**\*Corresponding author:** E-mail address: [yaseminerteniyte@gmail.com](mailto:yaseminerteniyte@gmail.com) Tel.: +902322936704; Fax: +902322936705

## INTRODUCTION

Ion exchange generally is performed by using traditional batch exchange method. However, ultrasound can be an alternative method to apply ion exchange in zeolites. In this work, zeolite NaX was used to perform ion exchange by using both methods. Zeolites are microporous, crystalline aluminosilicate minerals with a cage like structure of  $\text{AlO}_4$  and  $\text{SiO}_4$  tetrahedra bound by shared oxygen atoms. The crystal structure consists of sodalite cages through double six-rings (D6R) and supercage accessible by a three-dimensional 12-ring pore system (Figure 1). As a consequence, different sites are observed. The principle sites of zeolite X are; site I in the center of the hexagonal prism, site II and site III in the single six-membered ring (S6R) and near the four-ring windows of the supercage [1]. Zeolite X can accommodate variety of cations, such as  $\text{Na}^+$ ,  $\text{K}^+$ ,  $\text{Ca}^{2+}$ ,  $\text{Mg}^{2+}$  and others at these sites in the unit cell of X zeolite structure. These cations are mobile and can readily be exchanged for others in a contact solution [2, 3]. The trivalent cation,  $\text{Ce}^{3+}$  ion, prefer to locate site I, the most stable site rather than site II as stated by Jasra *et al.* [4]. Location of  $\text{Ce}^{3+}$  ions determine the application field of zeolite in industry.

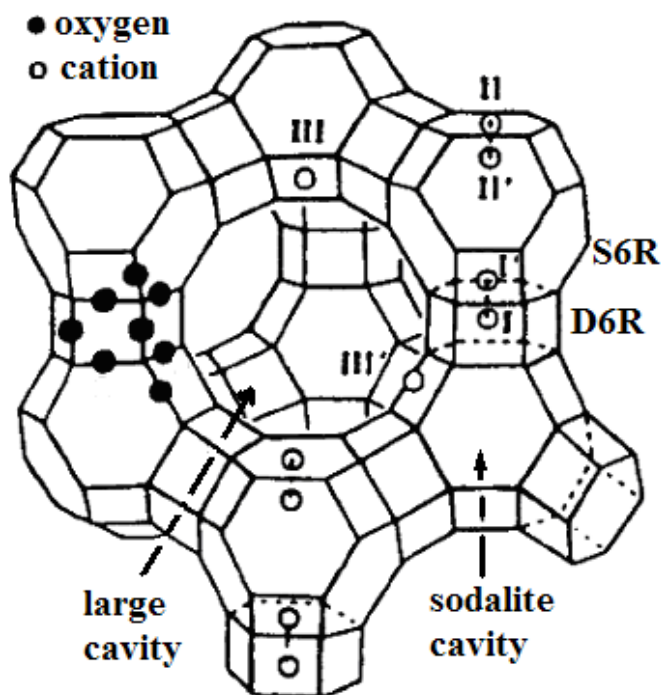


**Figure 1:** Unit cell structure of NaX zeolite with cation sites [1].

Ultrasound is a source of high energy vibrations that produces ultrasonic waves with frequencies. There are three main types of ultrasonic (US) sources; gas driven, liquid driven and electromechanical. Electromechanical sources are based on the piezoelectric and magnetostrictive effects used when homogenization and efficient mixing are required. Piezoelectric transducer is the most commonly used in power bath and probe-

type sonicators which are used generally by analytical chemists and operated at a fixed frequency; 20 kHz for common probe systems and 40 kHz for baths. Ultrasonic probes are generally preferred in order to use in analytical chemistry comparing to the ultrasonic baths [5]. The origin of the ultrasonic effect is the collapse of millions of micro bubbles created by ultrasonic irradiation. By this way, the mechanism of ultrasound can contribute to mass transfer enhancement [3].

The goal of this work is to investigate the effect of the ultrasound type on  $\text{Ce}^{3+}$  ion replacement kinetics in Zeolite NaX. This study is designed to understand the effect of ultrasonic source on the mass transfer.

## EXPERIMENTAL

Zeolite NaX (13X) in the crystal size of 2  $\mu\text{m}$  was used in binderless form (Aldrich). Cerium ( $\text{CeCl}_3 \cdot 7\text{H}_2\text{O}$ ) salts with high purity of 99.6 % was used in the ion exchange experiment. The ion exchange experiments were carried out by contacting NaX zeolite with  $\text{CeCl}_3 \cdot 7\text{H}_2\text{O}$  solution (0.08M) including 3, 5, 6 and 9 fold excess  $\text{Ce}^{3+}$  ions, theoretically needed amount to completely exchange the  $\text{Na}^+$  ions, in solution ( $\text{pH} = 5.5 \pm 0.25$ ) at 70 °C. The exchange solutions were centrifuged (Rotofix 32, Hettich) and washed several times to obtain  $\text{Cl}^-$  free Zeolite.

The ultrasound processor (Sonics-Vibra Cell 505) with  $20 \pm 0.050$  kHz frequency and 25 and 40 % of acoustic power (500 W) were used in the experiments. The processor has the replaceable probe tip having  $\frac{1}{2}$ " (13 mm) diameter. The probe was dipped to a depth of 15 mm and the temperature of the solution sonicated was maintained at 70 °C with circulating water (Figure 2). Ultrasonic bath at 35 kHz and 320 W was also used in order to perform the ion exchange at different frequency and power. The experimental conditions in the ion exchange by using ultrasound; ultrasonic probe and ultrasonic bath are tabulated in Table 1. Traditional batch ion exchange experiments were performed in the water bath shaker (GFL 1092) at 70 °C and 130 rpm. All experiments were provided for a sufficient time to enable the system to approach equilibrium. The experiments were repeated at least two times. Inductively Coupled Plasma Atomic Emission Spectroscopy (ICP-AES 96, Varian) was used to determine the cation content of the aqueous solution centrifuged.

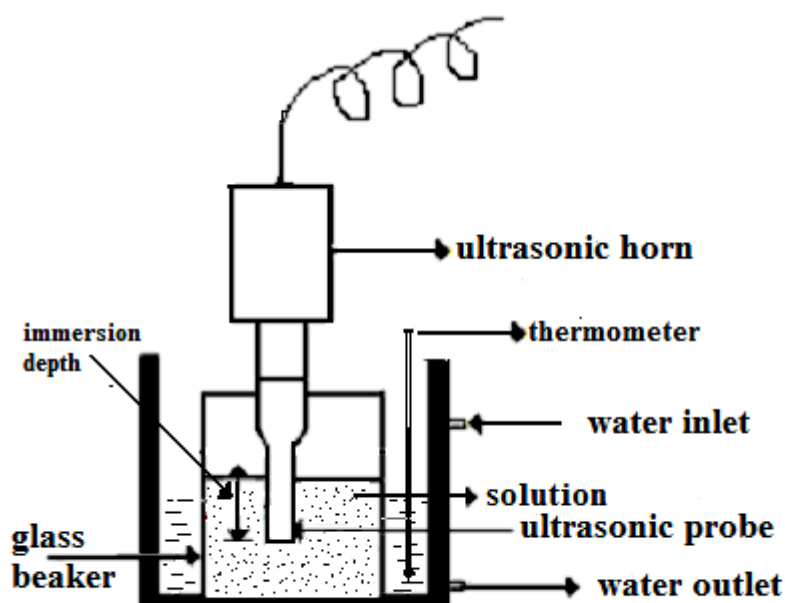


**Figure 2:** Experimental set-up of ultrasonic probe.

**Table 1:** Experimental conditions of the types of ultrasound used in the ion exchanges.

Codes*	Types of Ultrasound	Power	Frequency (kHz)
U-125W	Probe	125	20
U-200W	Probe	200	20
UB-320W	Bath	320	35

\* U: ultrasonic probe; UB: ultrasonic bath

Consecutive ion exchange experiments in which the solution was refreshed five times for each 30 min was applied to obtain fully exchanged zeolite.  $Ce^{3+}$  ion solutions with 5 fold equivalent excess were used in all consecutive ion exchange experiments.

In the codes the numbers (3, 5, 6 or 9) and the following letters (T:traditional, U: ultrasonic probe and UB: ultrasonic bath) were used for the fold excess and the methods, respectively. In the characterization of the Ce-rich zeolites obtained with the five consecutive ion exchange experiments; X-ray diffraction (XRD), scanning electron microscopy (SEM) and volumetric adsorption were used. Crystallinity of the zeolites were determined by X-ray diffraction (Philips X-Pert Pro Diffractometer) using  $CuK\alpha$  radiation at 45 kV and 40 mA in the  $2\theta : 5^\circ - 70^\circ$  with  $0.2^\circ$  step size. The micrographs of the zeolite crystals were taken by using scanning electron microscopy (SEM, Philips XL 30S) with LFD and ETD detector at 5.00 and 3.00 kV under vacuum conditions. Textural properties of zeolites such as surface area were determined by using volumetric

adsorption instrument (Micromeritics, ASAP 2010). Prior to adsorption, the samples were degassed for 24 h under vacuum better than  $10^{-5}$  mbar at 350 °C.

## RESULTS AND DISCUSSION

### Kinetic studies

The effect of fold equivalent excess of the  $Ce^{3+}$  ion solution to be introduced in the presence of ultrasonic probe (125 W), in the ion exchange were examined kinetically. The results were compared with those obtained from traditional batch method.

The ion exchange performed in this study ;



where  $M^{z+}$  is the counter ion, namely  $Ce^{3+}$ . Assuming that  $Ce^{3+}$  ions were exchanged with only  $Na^{+}$  ions into zeolite, the exchange percent of  $Na^{+}$  ion ( $\eta_{Na}$ ) was calculated;

$$\eta_{Na} = \left( \frac{q_o - q_{Na}}{q_o} \right) \times 100 \quad (1)$$

where  $q_o$  and  $q_{Na}$  ( $mg\ g^{-1}$ ) are the amount of  $Na^{+}$  ions into X zeolite initially and at any time t, respectively.

As seen from the kinetic curves of  $Ce^{3+}$  ion exchange (Figure 3), ion exchange was very fast initially and thereafter it slowed down. Ultrasound enhanced the exchange percent by means of transient cavitation bubbles with the theory of "hot spots" [5]: Hot spots increase the temperature and pressure near the surface of the Zeolite NaX causing enhancement in the cation exchange [6] compared to the traditional method [7,8]. As seen from Figure 3, the excess amount of  $Ce^{3+}$  ion in the solution causes to increase the equilibrium exchange percent up to %65 for 5 fold excess when ultrasonic probe was used, whereas the exchange percent is increased gradually in case of the traditional method. The difference between the methods disappeared at 9 fold excess. As stated in the literature [9], cerium has a tendency to hydrolyze with increasing concentration which prevents  $Ce^{3+}$  ions to enter the zeolite framework. As a result, ultrasonic method may have accelerated the hydrolysis of  $Ce^{3+}$  ions after the 5-fold excess compared to the traditional method.

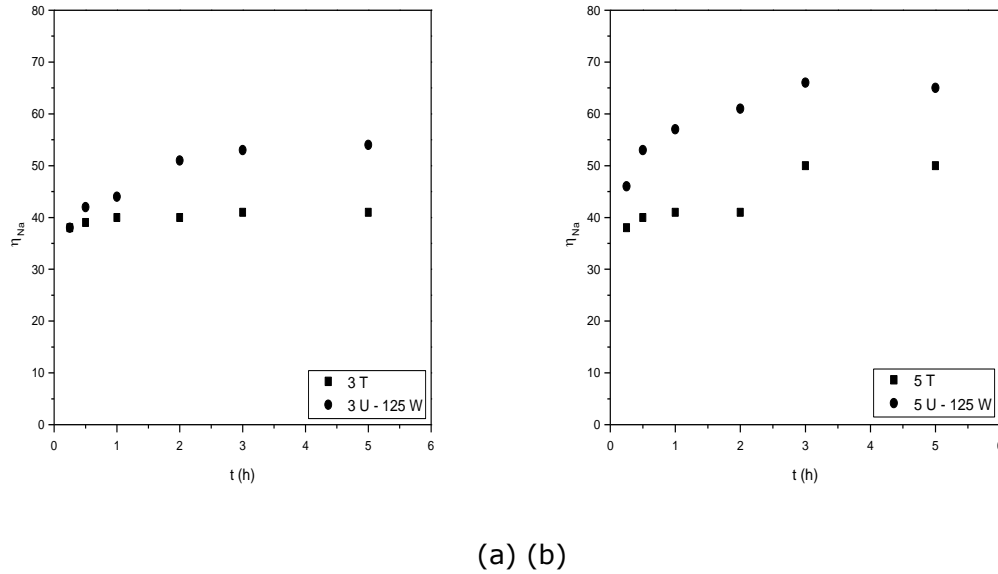


**Figure 3:** Kinetic curves of  $Ce^{3+}$  ion exchange (fold excess: (a) 3 (b) 5 c) 6 (d) 9).

### Effect of ultrasonic types

Two types of ultrasound method (ultrasonic probe and ultrasonic bath) were used in ion exchange experiments to investigate the effect of their frequency and power on ion exchange experiments. As seen from the kinetic curves of  $Ce^{3+}$  ion exchange (Figure 4), ultrasonic probe method is more effective than ultrasonic bath method. Although ultrasonic probes deliver their energy on a localized zone, it provides a great many transient cavitation bubbles not only in the fluid phase surrounding the particles but also in the solution within the porous particles. Therefore it was observed that ultrasonic probe method enhanced the exchange compared with the traditional method and ultrasonic bath method. The exchange percent was changed depending on the method and the type of the ultrasound used:  $U-125W > U-200W > T \geq UB-320W$ .

The higher exchange amount was obtained as the lower power was applied. It can be explained with the frequency and power used. Because acoustic power through the liquid causes large number of cavitation bubbles many of which coalesce into larger, longer lived bubbles that will give rise to hinder the acoustic energy through the liquid as stated by Castro and Capote (2007). If the frequency used in ion exchange increased, cavitation bubbles became initially difficult since the frequency affects the threshold intensity and performance of the ultrasound in ion exchange. Therefore, suitable power and frequency should be selected according to the process.

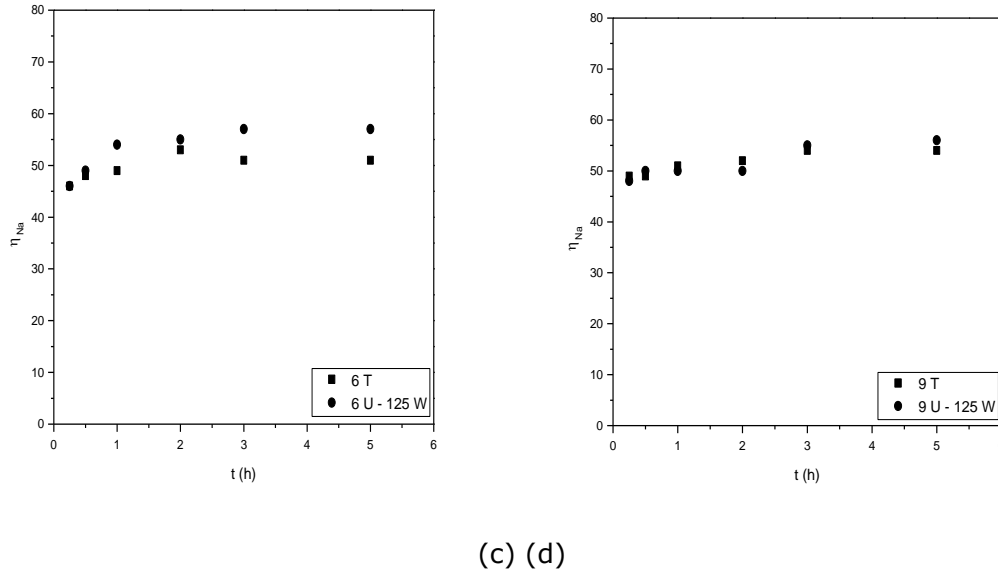


**Figure 4:** Comparison of kinetic curves obtained for 5 fold excess cerium.

#### Enhancement of Exchange with consecutive ion exchange

Equilibrium experiments were conducted by refreshing the counter ion ( $\text{Ce}^{3+}$ ) in the solution. As seen from Figure 5, ultrasonic probe (125 W) was used in consecutive ion exchanges and compared with traditional batch method in 5 fold excess cerium solutions. Figure shows the change in the exchange percent of  $\text{Na}^+$  ion with number of consecutive ion exchange. The highest exchange of  $\text{Na}^+$  ions was observed with the 1<sup>st</sup> consecutive ion exchange experiment. On the other hand almost no exchange in the 5<sup>th</sup> consecutive ion exchange was obtained. However the effect of the method is evident in  $\text{Ce}^{3+}$  ion exchange; 62 % from traditional method and 73 % from ultrasonic method. As a conclusion, the cerium is partially exchanged due to other effects such as agglomeration of cerium oxide on the crystal surface with the consecutive exchanges. Hence fully cerium exchanged zeolite X cannot be obtained.

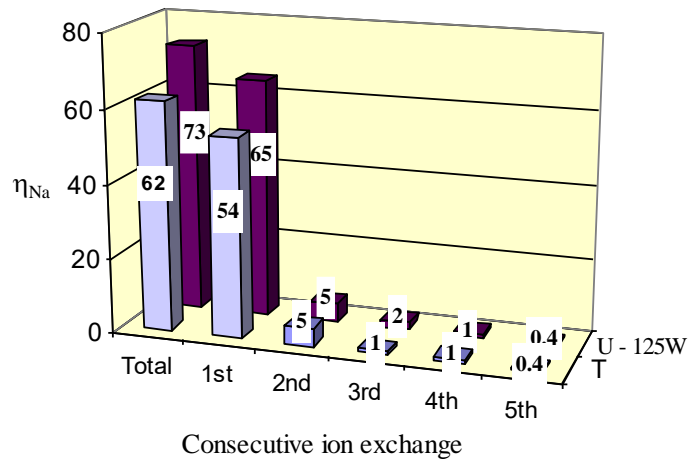


**Figure 5:** The effect of consecutive ion exchange on the exchange Na amount (%) for; traditional (T) and ultrasonic probe (U-125W) methods.

### Characterization Studies

The characterization studies were applied to Ce-exchanged zeolite obtained after 5 consecutive ion exchange experiments. The structural and textural properties of the zeolites were investigated by using volumetric adsorption system, X-Ray diffractometer (XRD) and scanning electron microscope (SEM).

$N_2$  adsorption isotherms of the zeolites are shown in Figure 6. According to the IUPAC classification,  $N_2$  adsorption isotherms of the NaX zeolite and Ce-rich zeolite obtained from traditional and ultrasonic probe methods are of Type I. The U-125 W zeolite with microporous structure has the lowest adsorption amount at 77 K and 1 atm. The isotherm data obtained were evaluated for the textural properties of the zeolites and tabulated (Table 2). The specific surface area and micropore volume was decreased when the  $Na^+$  ions are exchanged with  $Ce^{3+}$  ions. Because cerium oxides block the accessible pores, complexes have formed.

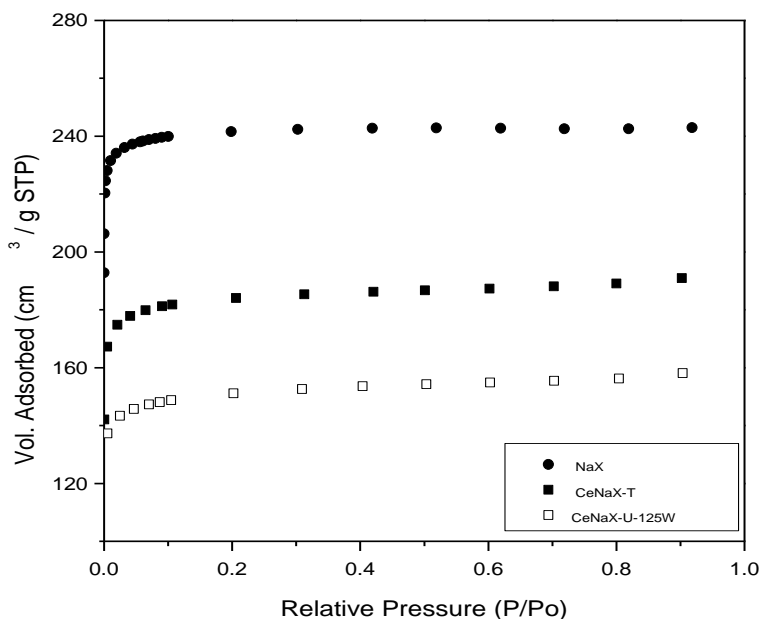


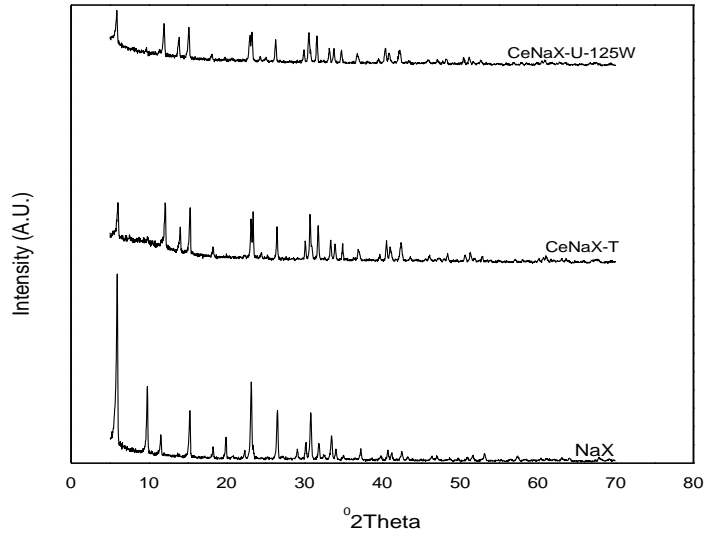
**Figure 6:** N<sub>2</sub> adsorption isotherms of NaX, and cerium exchanged zeolite with traditional (CeNaX-T) and ultrasonic probe (CeNaX-U-125W) methods.

**Table 2:** Textural properties of the zeolites obtained with consecutive ion exchanges.

Zeolite Codes	Exchange amount (%)	Area <sup>L</sup> (m <sup>2</sup> g <sup>-1</sup> )	V <sub>mic</sub> (cm <sup>3</sup> g <sup>-1</sup> )	D <sub>Median</sub> (Å)
NaX	---	1058	0.37	5.67
T	62	809	0.28	7.29
U-125W	73	666	0.23	8.28

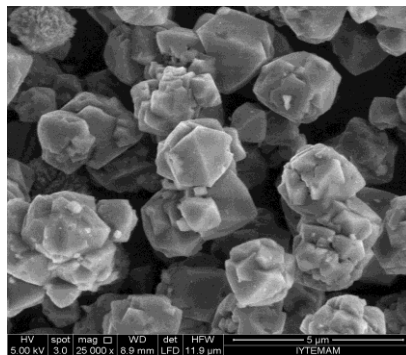
A<sup>L</sup>: Surface area from Langmuir method; D<sub>Median</sub> and V<sub>mic</sub>: Median diameter and micropore pore volume calculated from Horvath-Kawazoe Method

Figure 7 shows the X-ray diffractogram of the zeolites. The cation exchange resulted in the missing of some peaks due to the cerium oxide occluded on the crystal surface as mentioned in the literature [11, 12]. This means that X-ray diffraction studies of the zeolites in powders confirm the migration of cerium to the extra-framework sites of Zeolite X.

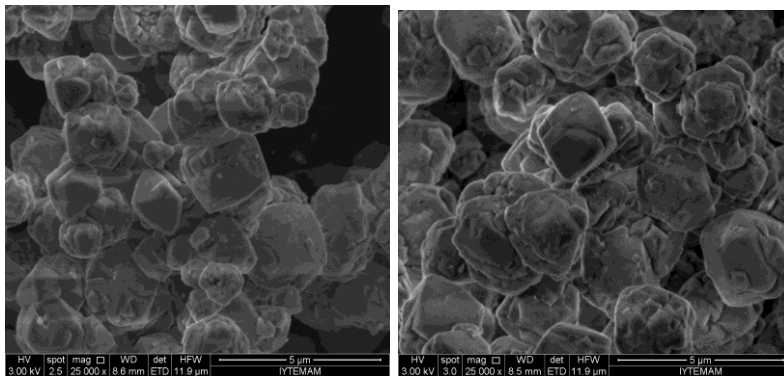


**Figure 7:** X-ray diffraction patterns of NaX and cerium exchanged zeolite with traditional (CeNaX-T) and ultrasonic probe (CeNaX-U-125W) method.

SEM images of the zeolite surfaces shows the changes in the crystals of cerium rich zeolite X conforming the occlusion of cerium oxide on the crystal..



(a)



(b) (c)

**Figure 8:** SEM images of zeolites: (a) NaX (b) T (c) U-125W.

## CONCLUSION

The effect of the ultrasonic irradiation on the  $Ce^{3+}$  ion exchange was investigated. The present study shows that the use of ultrasonic probe with 125 W during ion exchange significantly affects the exchange amount at equilibrium which acted like a co-driven force of concentration of  $Ce^{3+}$  ions in solution due to cavitation effect of ultrasonic field and increased the exchange amount in ion exchange process. This situation did not accelerate the exchange of  $Na^+$  with  $Ce^{3+}$  ions, as observed in  $Na^+$  exchange with  $Li^+$  ions in our previous paper, but enhance the amount of exchange. The cerium in the solution caused to be formed cerium oxides on the crystal surface occluding the pores and partially exchange was obtained. Thus the specific surface area of cerium exchanged zeolite was decreased due to formation of cerium complexes on the surface and into the pores.

## ACKNOWLEDGEMENT

The authors would like to thank Izmir Institute of Technology (Project number: 2006IYTE31) and State Planning Organization of Turkey (DPT) for financial support.

## REFERENCES

- [1] N.D. Hutson, S.U. Rege, R.T. Yang, Mixed cation zeolites:  $Li_xAg_y-X$  as a superior adsorbent for air separation, *Separations* 45 (1999) 724-734.
- [2] V.H. Bekkum, E.M. Flanigen, P.A. Jacobs, J.C. Jansen, *Introduction Zeolite Science and Practice*, second completely revised and expanded edition, Elsevier Science, 2001.
- [3] Y. Erten-Kaya, F. Cakicioglu-Ozkan, Effect of ultrasound on the kinetics of cation exchange in NaX zeolite, *Ultrasonics Sonochemistry*, 19 (2012) 701-706.
- [4] R.V. Jasra, N.V. Choundary, S.G.T. Bhat, Correlation of sorption behaviour of Nitrogen, Oxygen, and Argon with cation locations in zeolite X, *Ind.Eng.Chem.Res.* 35 (1996) 4221-4229.
- [5] M.D. Castro, F.P. Capote, *Techniques and Instrumentation in Analytical Chemistry: Analytical Applications of Ultrasound*, Volume 26, Elsevier B.V., 2007.
- [6] M.H. Entezari, M. Tahmasbi, Water softening by combination of ultrasound and ion exchange, *Ultrasonic Sonochem.* 16 (2009) 356-360.
- [7] J. Ji, X. Lu, Z. Xu, Effect of ultrasound on adsorption of Geniposide on polymeric resin, *Ultrasonics Sonochemistry* 13 (2006) 463-470.
- [8] J. Ji, X. Lu, M. Cai, Z. Xu, Improvement of leaching process of Geniposide with ultrasound, *Ultrasonics Sonochemistry* 13 (2006) 455-462.

- [9] H. Faghihian, M.K. Amini, A.R. Nezamzadeh, Cerium uptake by zeolite A synthesized from natural clinoptilolite tuffs, *Journal of Radio Analytical and Nuclear Chemistry* 264 (2005) 577-582.
- [10] S.A. Peter, A.S. Moharir, V.R. Jasra, Selective adsorption of oxygen over argon in alkaline-earth-metal cation-exchanged zeolite X, *Ind. Eng. Chem. Res.* 49 (2010) 7524-7529.
- [11] R.V. Jasra, B. Tyagi, Y.M. Badheka, V.N. Choudary, T.S.G. Bhat, Effect of clay binder on sorption and catalytic properties of zeolite pellets, *Ind. Eng. Chem. Res.* 42 (2003) 3263-3272.
- [12] J.-Ch. Buhl, M. Gerstmann, W. Lutz, A. Ritzmann, Hydrothermal stability of the novel zeolite type LSX in comparison to the traditional 13X modification, Hannover, Institut für Mineralogie, 2003.



## Binder Effect on Electrochemical Performance of Zinc Electrodes For Nickel-Zinc Batteries

<sup>1</sup>Gizem CİHANOĐLU, <sup>1,a</sup> Özgenc EBİL

Department of Chemical Engineering, İzmir Institute of Technology, İzmir, Turkey

*(This article first appeared in PPM2017 and was accepted as a non-peer-reviewed manuscript to be published in JOTCSA)*

**Abstract:** Polyethylene glycol (PEG) and polyvinyl alcohol (PVA) were used as a zinc electrode binder at different concentrations to enhance the electrochemical behavior of zinc electrodes for nickel-zinc (NiZn) batteries. ZnO powders synthesized by mechanochemical and hydrothermal precipitation methods were mixed with lead oxide, calcium hydroxide and binder to prepare zinc electrodes in pouch cell NiZn batteries. Scanning Electron Microscopy (SEM) and X-Ray Diffraction (XRD) analysis reveal that initial morphology of zinc electrode changes drastically regardless of the binder type and its loading after charge/discharge process, and even the charge/discharge process is not complete. The results show that the presence of PEG causes better discharge capacity compared to that of PVA as a binder. Zinc electrode prepared using commercial ZnO powder and 3 wt.% PEG gives the optimum discharge capability, with a specific capacity of approximately 311 mAhg<sup>-1</sup>, while zinc electrodes prepared using ZnO powder synthesized from ZnCl<sub>2</sub> and Zn(NO<sub>3</sub>)<sub>2</sub>·6H<sub>2</sub>O and 6 wt.% PEG exhibit high specific energy of 255 and 275 mAhg<sup>-1</sup>, respectively. The results suggest a relationship between binder loading and battery capacity, but in-situ analysis of microstructural evolution of zinc electrode during charge/discharge process is needed to confirm this relationship.

**Keywords:** Zinc electrode, NiZn secondary batteries, PEG, PVA.

**Cite this:** Cihanođlu G, Ebil Ö. Binder Effect on Electrochemical Performance of Zinc Electrodes For Nickel-Zinc Batteries. JOTCSA. 2017;5(sp.is.1):65-84.

**\*Corresponding author.** E-mail. [ozgencebil@iyte.edu.tr](mailto:ozgencebil@iyte.edu.tr)

## INTRODUCTION

The nickel-zinc battery is one of the most significant energy storage systems for various electrical applications due to moderate specific energy (55–85 Whkg<sup>-1</sup>), high power density (140–200 Whkg<sup>-1</sup>), high open circle potential (1.705 V), and a nominal cell voltage of 1.6 V [1-2]. Nickel-zinc batteries have attractive advantages such as being low cost, environmentally friendly and having abundant resources for raw materials. However, these kind of batteries have not reached their full potentials mostly due to critical problems. These problems are attributed to shape change of zinc electrode with increasing charge/discharge cycle count, zinc electrode passivation, and dendritic zinc growth leading to short-circuiting of the battery. During discharge process, zincate ion (Zn(OH)<sub>4</sub><sup>2-</sup>) in the alkaline electrolyte is formed before zinc oxide precipitates. During charging process, the concentration of zincate ions near the bottom of the electrode decreases and zincate ions are precipitated as zinc oxide when the limit of solubility is reached. This process leads shape change and the formation of dendrite of zinc as well as the protrusion on the surface of zinc electrode with increasing number of charge/discharge cycles. Passivation is also another serious problem for deterioration of zinc-based batteries. The passivation of zinc electrode occurs when the solubility of zincate is exceeded in electrolyte close to the surface of the zinc electrode, and an insulating ZnO barrier layer is formed on electrode surface [3-5]. As a result of these issues, short cycle life and/or poor electrochemical performance have limited the wide-range application of NiZn batteries. Many attempts have been made to overcome these problems. One approach is to use additives in either electrode [6-9] or electrolyte [10-12]. Another one is to fabricate an electrode including different morphology and size of zinc oxide [13-15]. Some of oxide additives used in zinc electrode, such as Ca(OH)<sub>2</sub> [16,17], Bi<sub>2</sub>O<sub>3</sub> [18], PbO [19], TiO<sub>2</sub> [20], and In<sub>2</sub>O<sub>3</sub> [21] are convenient to decrease the concentration of the zinc oxidation products and improve electronic conductivity and current distribution [17]. Binders or gels, such as sodium silicate [22], tapioca [23], polytetrafluoroethylene [24, 25], carbopol gel [26, 27], and sago [28], are ways to improve the active material utilization and effective surface area in zinc electrode.

Many organic additives in alkaline solutions are used as zinc corrosion inhibitors. Polyethylene glycol (PEG) is suitable for binding agent in electrode preparation to inhibit zinc corrosion. Ein-Eli and co-workers investigated the effect of PEG with a molecular weight 600 kgkmol<sup>-1</sup> and polyoxyethylene alkyl phosphate ester acid (GAFAC RE600) on zinc metal electrode [29]. The results showed that the electrochemical studies represented PEG in alkaline solution had much more efficient inhibition capability compared to GAFAC RA600 [29].

Additionally, poly(vinylalcohol) (PVA) which is one of the alkaline polymers are also used as a binder to enhance ionic conductivity of electrolyte and electrode. The influence of PVA and KOH in polymer electrolytes on ionic conductivity of electrolyte was investigated by Mohamad *et al.* [17]. The result of this study indicated that the capacity was found to be 5.5 mAh at the end of

100 cycles [17]. In another study, polymer gel electrolyte with 60:40 ratio in zinc-carbon cell was examined by Saleem et al. [30]. It was observed that the current charge/discharge efficiency was found to be 57 % [30]. Wu and co-workers focused on the PVA-KOH-TiO<sub>2</sub> alkaline polymer solid electrolyte in NiZn batteries [31]. It was reported that the specific capacity of PVA-KOH-TiO<sub>2</sub> polymer electrolyte, 250 mAhg<sup>-1</sup>, was higher in comparison with the specific energy of PVA-KOH polymer electrolyte, 190 mAhg<sup>-1</sup> [31].

In our previous paper, we reported the preparation of prismatic NiZn batteries with various initial zinc electrode morphologies [32]. ZnO powders were synthesized from different precursors, ZnCl<sub>2</sub> and Zn(NO<sub>3</sub>)<sub>2</sub>.6H<sub>2</sub>O to fabricate zinc electrodes for prismatic NiZn batteries. It was found that initial morphology of zinc electrode had an effect on electrode discharge capacity. The resulting ZnO electrodes with ZnO powders synthesized from ZnCl<sub>2</sub> and Zn(NO<sub>3</sub>)<sub>2</sub> demonstrated average battery energy densities varying between 92 Whkg<sup>-1</sup> and 109 Whkg<sup>-1</sup> whereas with conventional ZnO powder gave higher energy density of 118 Whkg<sup>-1</sup> [32].

Herein, we present zinc electrode prepared using binder, PEG or PVA, with different concentrations for the pouch cell NiZn batteries. The various zinc oxide structures were also prepared by different processes. Additionally, the various loadings of binders for porous zinc electrode (3, 6 and 12 wt.%) to achieve the battery performance were explored. The aim of this work was to fabricate a nickel-zinc battery by employing PEG and PVA as the binder for the porous zinc electrode and to determine the optimum composition of binder. Morphological studies of zinc oxide as active material for the porous electrode were used to promote the findings.

## MATERIALS AND METHODS

### Preparation of ZnO powders

ZnO powders with different morphologies were synthesized from ZnCl<sub>2</sub> and Zn(NO<sub>3</sub>)<sub>2</sub>.6H<sub>2</sub>O precursors following the method reported previously [32]. Nanosized spherical and plate-like shaped ZnO particles were prepared by simple precipitation method. Briefly, in the first precipitation method, 100 mL solution containing 0.2 M KOH and 0.02 M triethanolamine (TEA) was mixed with 100 mL of 0.1 M ZnCl<sub>2</sub> solution under ultrasonic treatment (WUC-D06H, Wids) at 50°C. The precipitate was separated by centrifuging (Sigma, 3-16 PK) at room temperature. The solid phase was washed with 0.1 M NH<sub>4</sub>OH solution three times. Finally, the solid phase was dried at 50°C, then baked at 200°C in oven.

In precipitation method for nanosized plate-like shaped ZnO, 100 ml of 1 M Zn(NO<sub>3</sub>)<sub>2</sub>.6H<sub>2</sub>O solution, 27.85 ml of 8 M NaOH and 22.15 mL of ultrapure water were mixed to obtain a desired pH value. NaOH solution and ultrapure water were added into Zn(NO<sub>3</sub>)<sub>2</sub>.6H<sub>2</sub>O solution while stirring in a magnetic stirrer at 20°C. As-prepared solution was aged at 20°C for 30 minutes. The

precipitate was separated by centrifuging. The solid phase was washed with ultrapure water three times. Finally, the solid phase was dried at 50°C, and then baked at 200°C in oven.

The morphologies of commercial ZnO powder (KIMETSAN, 99%), powders produced by mechanochemical methods at elevated temperatures were characterized by powder X-ray diffraction (XRD, Phillips™ Xpert diffractometer with Cu K $\alpha$  radiation) and scanning electron microscope (SEM, FEI Quanta250).

### **Preparation of electrodes for test cells**

In order to minimize the time for electrical characterization and materials use, only 1 gram of zinc oxide powder was used in zinc electrodes in all experiments. Zinc electrodes with different compositions were prepared. Details of zinc electrodes are summarized in Table 1. Zinc electrode paste was prepared by mechanically mixing zinc oxide, calcium hydroxide (3 wt.%), lead oxide (1 wt.%), polyethyleneglycol or polyvinylalcohol as binders (300  $\mu$ L aqueous solution), and 100  $\mu$ L of 10 wt.% KOH solution. The binder loading was varied between 3 and 12 wt. The paste was applied onto a 40  $\mu$ m thick craft paper to form a uniform layer and a copper wire was placed on top as current collector. The craft paper was then folded and sealed to obtain a zinc electrode 2 cm x 2 cm in size. To make sure that there is a good contact between current collector and zinc electrode, electrodes were tightly sealed under pressure.

**Table 1:** Zinc electrode samples.

Sample name	Contents	Composition ratio
A1	ZnO from ZnCl <sub>2</sub> :calcium hydroxide:lead oxide:PEG	93:3:1:3
A2	ZnO from ZnCl <sub>2</sub> :calcium hydroxide:lead oxide:PEG	90:3:1:6
A3	ZnO from ZnCl <sub>2</sub> :calcium hydroxide:lead oxide:PEG	84:3:1:12
A4	ZnO from ZnCl <sub>2</sub> :calcium hydroxide:lead oxide:PVA	93:3:1:3
A5	ZnO from ZnCl <sub>2</sub> :calcium hydroxide:lead oxide:PVA	90:3:1:6
A6	ZnO from ZnCl <sub>2</sub> :calcium hydroxide:lead oxide:PVA	84:3:1:12
B1	ZnO from Zn(NO <sub>3</sub> ) <sub>2</sub> .6H <sub>2</sub> O:calcium hydroxide:lead oxide:PEG	93:3:1:3
B2	ZnO from Zn(NO <sub>3</sub> ) <sub>2</sub> .6H <sub>2</sub> O:calcium hydroxide:lead oxide:PEG	90:3:1:6
B3	ZnO from Zn(NO <sub>3</sub> ) <sub>2</sub> .6H <sub>2</sub> O:calcium hydroxide:lead oxide:PEG	84:3:1:12
B4	ZnO from Zn(NO <sub>3</sub> ) <sub>2</sub> .6H <sub>2</sub> O:calcium hydroxide:lead oxide:PVA	93:3:1:3
B5	ZnO from Zn(NO <sub>3</sub> ) <sub>2</sub> .6H <sub>2</sub> O:calcium hydroxide:lead oxide:PVA	90:3:1:6
B6	ZnO from Zn(NO <sub>3</sub> ) <sub>2</sub> .6H <sub>2</sub> O:calcium hydroxide:lead oxide:PVA	84:3:1:12
C1	commercial ZnO:calcium hydroxide:lead oxide:PEG	93:3:1:3
C2	commercial ZnO:calcium hydroxide:lead oxide:PEG	90:3:1:6
C3	commercial ZnO:calcium hydroxide:lead oxide:PEG	84:3:1:12
C4	commercial ZnO:calcium hydroxide:lead oxide:PVA	93:3:1:3
C5	commercial ZnO:calcium hydroxide:lead oxide:PVA	90:3:1:6
C6	commercial ZnO:calcium hydroxide:lead oxide:PVA	84:3:1:12

2.7 M KOH solution was used as an electrolyte in experimental study. For cell testing, zinc electrodes and nickel electrodes were placed in a beaker filled with 2.7 M KOH electrolyte. Nickel electrodes as an anode are used in commercial NiMH batteries with 2050 mAh capacity in this study. No further treatment or process was applied. Nickel electrode capacity was kept twice the theoretical capacity required for testing by connecting multiple nickel electrodes in parallel.

### Electrochemical tests

The charge/discharge tests were performed using two DC power supplies (RXN 305D) which work either current or voltage limited. All tests were performed at room temperature. Initial charging of the cells was performed at a constant voltage of 2.4 V. Discharge tests were applied by attaching a 10-Ω load to cells. Zinc electrodes after charge-discharge cycles were dried at 30°C under vacuum for evaluation of microstructure during battery operation.

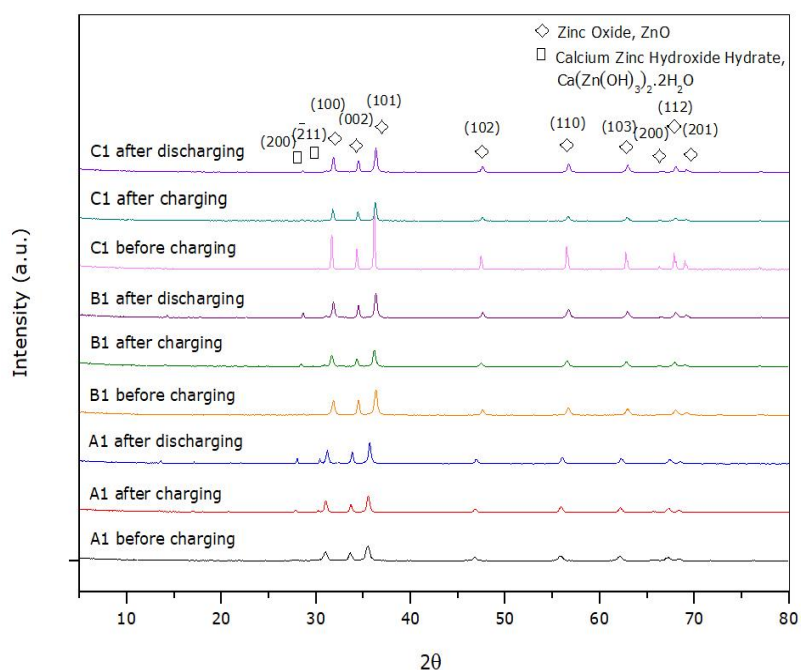
## RESULTS AND DISCUSSION

### The characterization of zinc oxide powder

The characterization of zinc oxide powders which were necessary for the production the zinc electrode were detail given in our previous work [32]. When briefly referring to the results, the XRD analysis showed that the existence of only ZnO in synthesized powders was confirmed, and no peaks related to  $\text{Zn}(\text{OH})_2$  was observed [32]. Based on the results of SEM, it was found that the commercial ZnO powder had greater crystallinity compared to synthesized ZnO powders. Beside this, ZnO powder synthesized from  $\text{ZnCl}_2$  had a homogeneous distribution of spherical particles while ZnO powder synthesized from  $\text{Zn}(\text{NO}_3)_2 \cdot 6\text{H}_2\text{O}$  showed different morphologies with plate-like structures mixed with need-like particles. Also, the commercial ZnO showed a wide range of particle size distribution with most of the particles having needle-like shapes as well as having tripod and nanorod shapes [32].

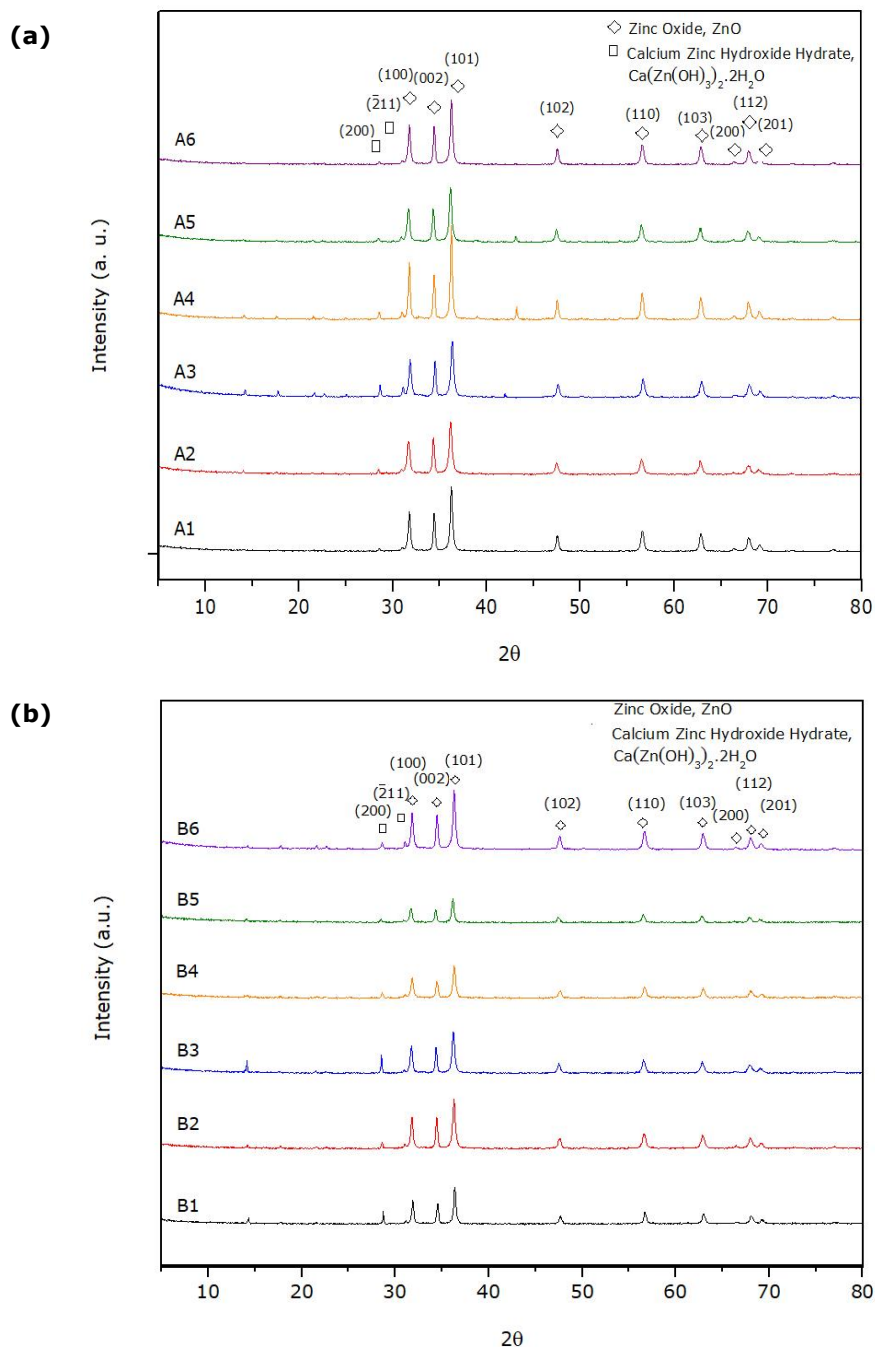
### XRD patterns analysis of zinc electrodes

In order to confirm initial findings related to morphology of the electrode before its first charge, after first charge and first discharge, XRD analysis is performed on each zinc electrode containing different ZnO powders (commercial ZnO powder, ZnO powder synthesized from both  $\text{ZnCl}_2$  and  $\text{Zn}(\text{NO}_3)_2 \cdot 6\text{H}_2\text{O}$ ) and 3 wt.% PEG as a binder, as shown in Figure 1. The XRD patterns show that the content of zinc oxide is dominant for each zinc electrode (JCPDS-2 79-2205, JCPDS-2 24-0222). Compared all the XRD patterns, the course of the baseline indicated that no-impurity phase is observed.



**Figure 1:** XRD spectra of each zinc electrode before charging, after charging and after discharging.

XRD spectra of all zinc electrodes containing binders, either PEG or PVA, with different concentrations are presented in Figure 2. The XRD patterns show that zinc oxide was dominant phase for each zinc electrode after three charge/discharge cycles (JCPDS-2 79-2205, JCPDS-2 24-0222). Figure 2a shows XRD spectra of zinc electrodes containing ZnO synthesized from  $\text{ZnCl}_2$ . Based on XRD spectra of samples A, there are some weak peaks of calcium zincate ( $\text{CaZn}$ ) for sample A2 and A4. The XRD spectra of zinc electrodes containing ZnO synthesized from  $\text{Zn}(\text{NO}_3)_2 \cdot 6\text{H}_2\text{O}$ , as shown in Figure 2b. Similar to samples A, the weak peaks of calcium zincate are detected in all samples B. It can be concluded that is no difference between all zinc electrodes after third discharge and electrode paste before first charge, and the result corresponds to previous report in the literature [32].



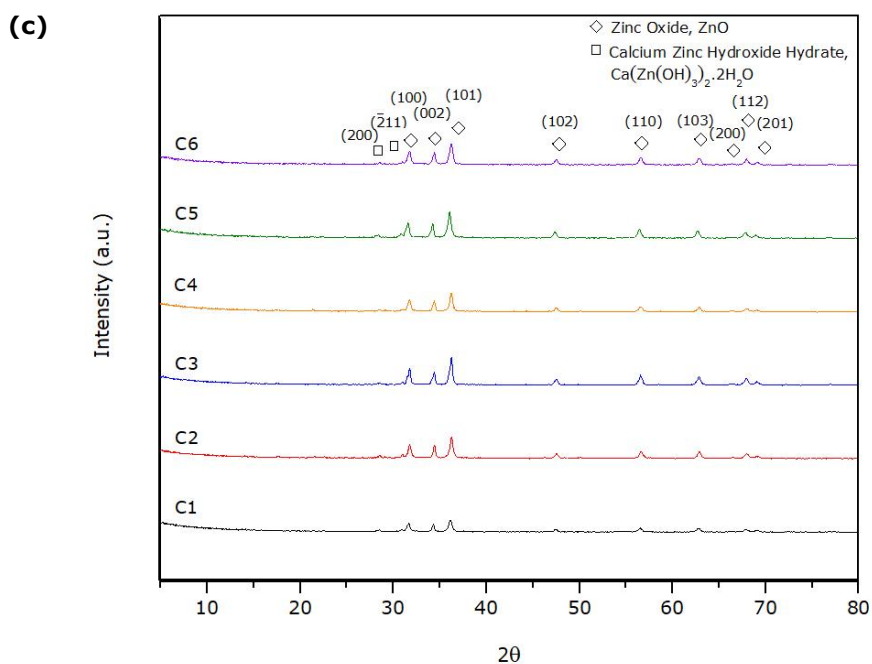


**Figure 2:** XRD spectra of zinc electrode for (a) ZnO synthesized  $\text{ZnCl}_2$ , (b) ZnO synthesized  $\text{Zn}(\text{NO}_3)_2 \cdot 6\text{H}_2\text{O}$ , (c) commercial ZnO.

### Morphology evolution of zinc electrodes

The morphology evolution process of zinc electrode prepared using zinc oxide powder synthesized from  $\text{ZnCl}_2$  and 3 wt.% PEG as a binder before charge, after first charge and first discharge are shown in Figure 3. The microstructure and surface morphology of the paste zinc electrode is shown in Figure 3a. The SEM image of zinc electrode after first charge is shown in Figure 3b. Compared to Figure 3a and Figure 3b, ZnO nanospheres were mostly replaced spindle-like structures, and most of the ZnO crystals were converted into zinc. However, detailed SEM analysis at different locations of the sample also reveals that first charging of these zinc electrode was not performed fully and there were some ZnO particles, which were not converted into metallic zinc. Figure 3c displays the morphology of the same zinc electrode after first discharge. It was observed that regardless of the initial morphology, the electrode showed morphologies almost completely erasing the memory of initial structure even after the first charging procedure.

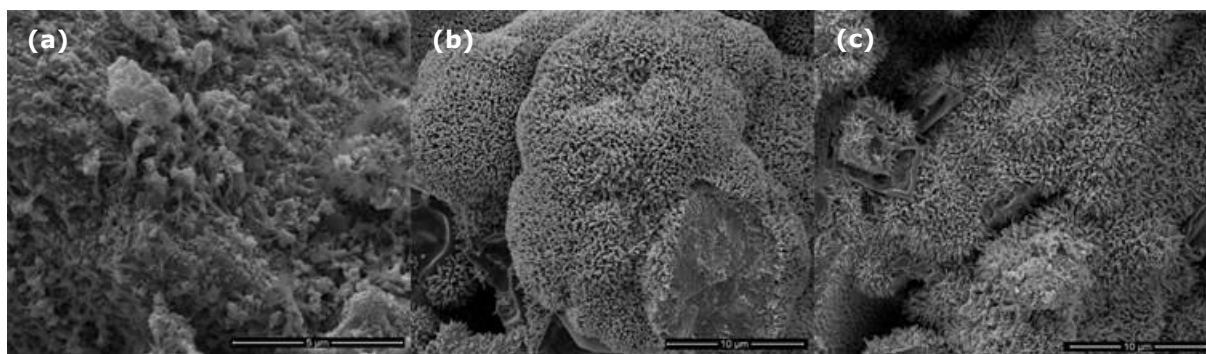


**Figure 3:** Morphology evolution of zinc electrodes for sample A1 (a) before charge, (b) after first charge, (c) after first discharge.

The microstructure evolution process of each zinc electrode containing ZnO synthesized from  $\text{ZnCl}_2$  and selected binders (PEG or PVA) with varying loading from 3wt.% to 12 wt.% is shown in Figure 4. Compared to the initial morphology of ZnO as seen in Figure 4a, ZnO nanospheres were converted to spindle-like structures. Large zinc crystals (flower like growth) with high aspect ratios were observed. However, these large crystals were also accompanied by smaller dendritic structures. From Figure 4a-f, it can be seen that the microstructure and surface morphology of each zinc electrode prepared using ZnO synthesized from  $\text{ZnCl}_2$  did not essentially change with the type of binder, PEG and PVA. With increasing of loading of binder, as shown in Figure 4a-f, the prismatic crystal growth of ZnO slightly decreases.

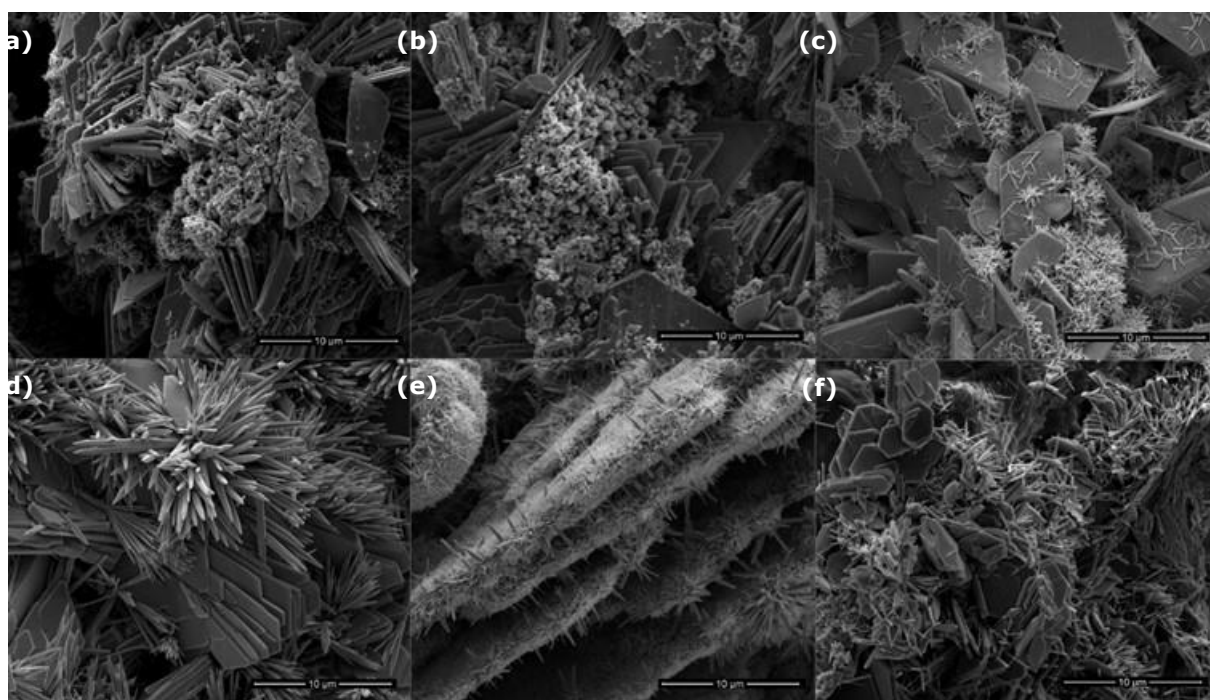


**Figure 4:** Morphology evolution of zinc electrodes for samples (a) A1, (b) A2, (c) A3, (d) A4, (e) A5, (f) A6.

The microstructure evolution process of zinc electrode prepared using ZnO powder synthesized from  $\text{Zn}(\text{NO}_3)_2 \cdot 6\text{H}_2\text{O}$  and 3 wt.% PEG before charge, after first charge and first discharge is shown in Figure 5. After charge/discharge cycle, the morphology of zinc electrode was found to be different than its initial morphology in terms of particle size and shape. Similarly, the morphology of zinc electrode shows spindle-like structures, and most of the ZnO crystals were converted into zinc after first charge, as seen in Figure 5b and Figure 5c.

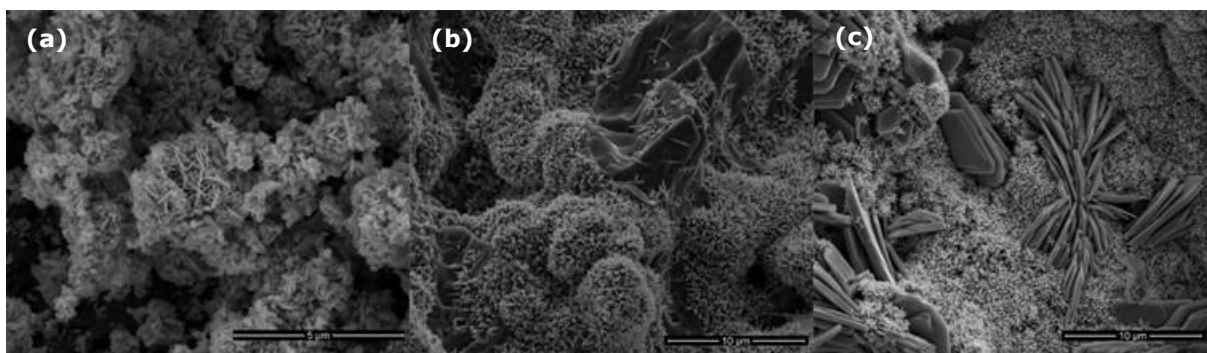


**Figure 5:** Morphology evolution of zinc electrodes for sample B1 (a) before charge, (b) after first charge, (c) after first discharge.

Figure 6 shows the morphology of zinc electrode prepared using ZnO synthesized from  $\text{Zn}(\text{NO}_3)_2 \cdot 6\text{H}_2\text{O}$  and different binders with various concentrations (3, 6 and 12 wt.%) after charge/discharge cycling. The plate-like structure of this kind of zinc electrode was replaced by spindle-like structures. It was observed that the electrodes showed similar morphologies almost completely erasing the memory of initial structure after the third discharging procedure. Based on SEM images, similar morphology change was observed when the loading of binder varied from 3 wt.% to 12 wt.% for both PEG and PVA as binders for zinc electrodes.

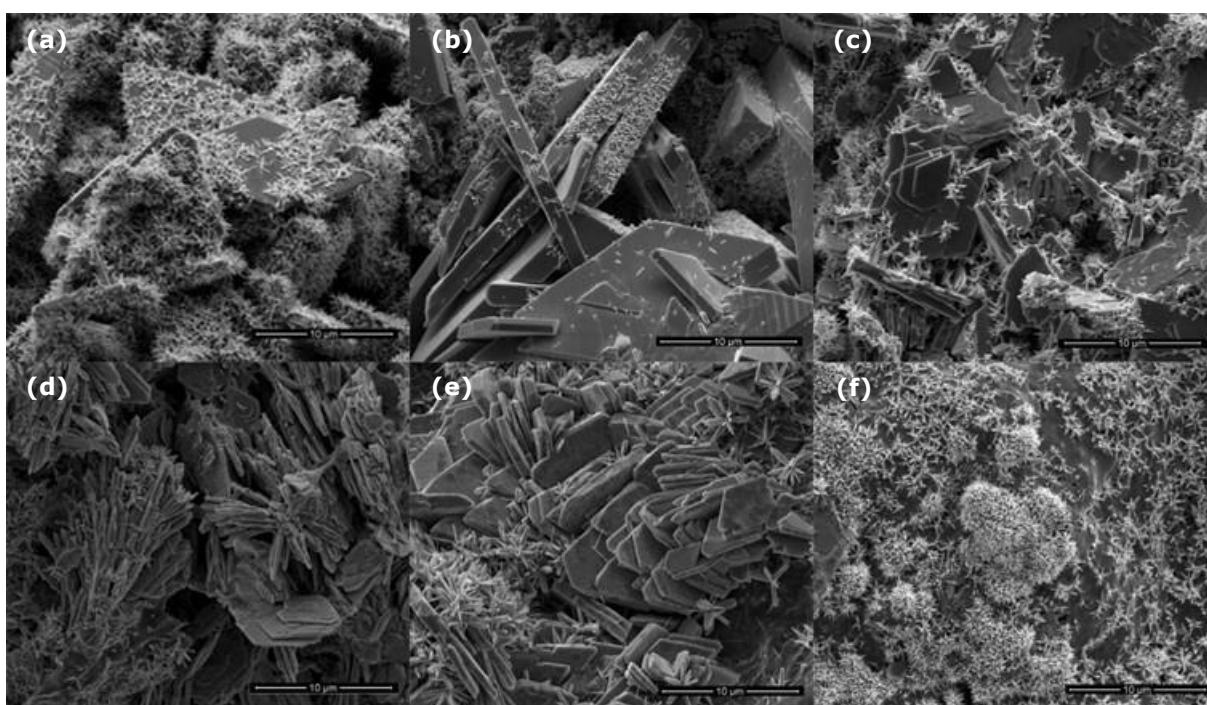


**Figure 6:** Morphology evolution of zinc electrodes for samples (a) B1, (b) B2, (c) B3, (d) B4, (e) B5, (f) B6.

The morphology evolution process of zinc electrode prepared using commercial ZnO powder and 3 wt.% PEG as a binder before charge, after first charge and first discharge are shown in Figure 7. The microstructure and surface morphology of the paste used for zinc electrode is shown in Figure 7a. After first charge/discharge process, the hexagonal structure of ZnO almost

disappeared and turned into dendritic form, as seen in Figure 7b and Figure 7c. However, detailed SEM analysis at different locations of the zinc electrode also reveals that first charging of this kind of zinc electrode was not performed fully and there were some ZnO particles which were not converted into metallic zinc.

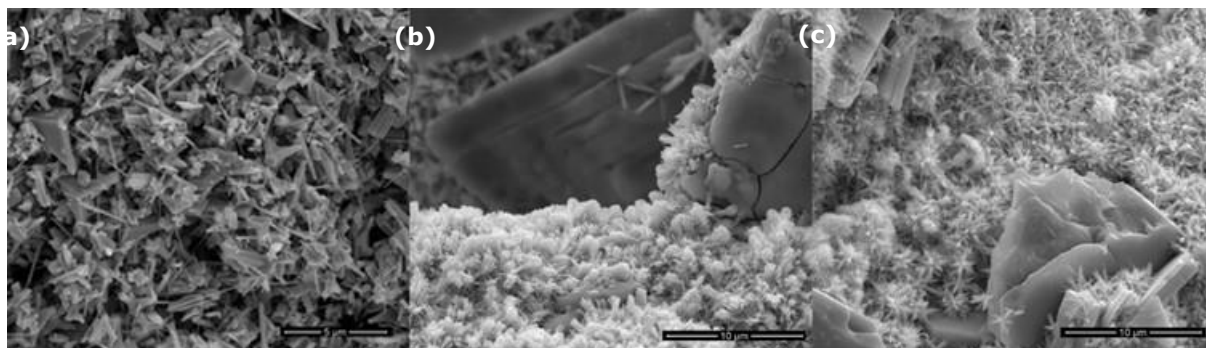


**Figure 7:** Morphology evolution of zinc electrodes for sample C1 (a) before charge, (b) after first charge, (c) after first discharge.

The morphology structures of zinc electrodes prepared using commercial ZnO powder and binder either PEG or PVA with various concentrations are displayed in Figure 8. The change in surface morphology of each zinc electrode related to the deposition of zinc after third discharge is same, as illustrated in Figure 8a-f. Compared to the initial morphology of zinc electrode as seen in Figure 7a, the morphology of hexagonal structure of zinc electrode changed, and replaced with zinc particles in acicular form, namely the dendritic zinc. From Figure 8a-f, it can be seen that the structure of each ZnO did not essentially change with the type of binder, PEG and PVA. With increasing of loading of binders, as shown in Figure 8a-f, the prismatic crystal growth of ZnO slightly decreases. Based on SEM analysis of zinc electrode prepared using commercial ZnO powder, the effect of binder type and binder loading seems to be minimal.

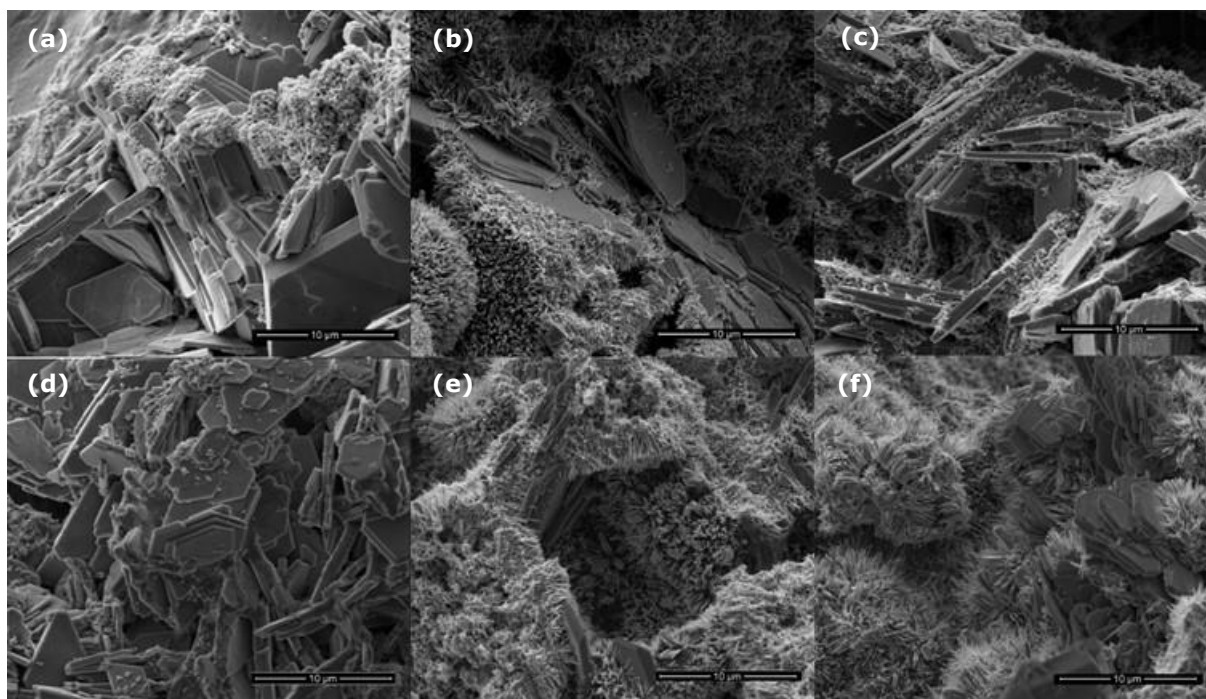


**Figure 8:** Morphology evolution of zinc electrodes for samples (a) C1, (b) C2, (c) C3, (d) C4, (e) C5, (f) C6.

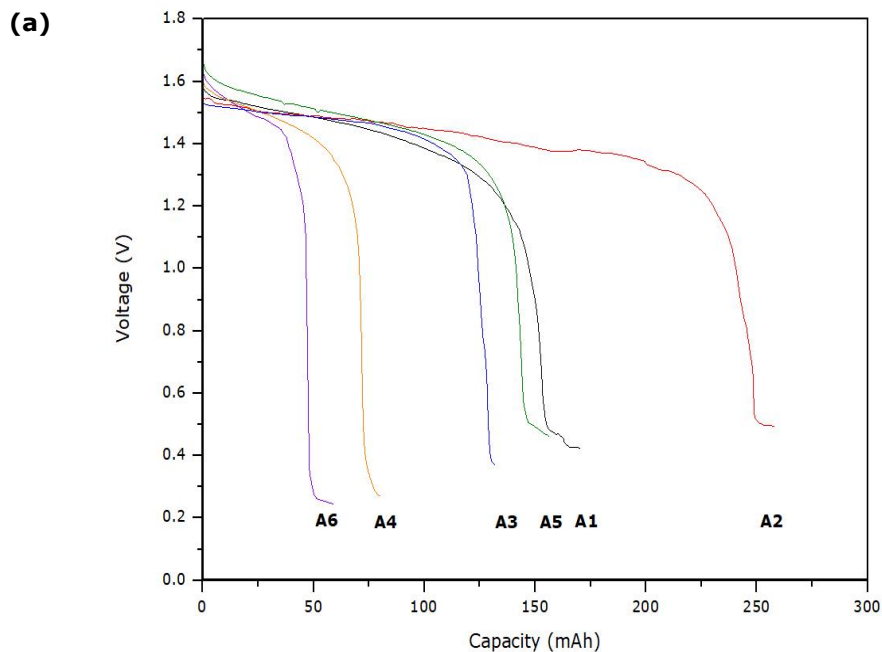
### Electrochemical performance of the zinc electrode

The electrochemical characteristics of pouch cell NiZn batteries were evaluated by charging and discharging batteries until complete battery failure. Initial charging of NiZn batteries were carried out at constant 2.4 V and room temperature. All NiZn batteries were charged until the current of battery reached to about 0.175 A. Fully charged batteries were discharged using a 10-Ohm resistance as load until battery potential reached to about 0.45 V. All charge–discharge tests were performed under the same conditions. The typical discharge curves of NiZn batteries tested at the third cycle are displayed in Figure 9a-c. Since electrolyte concentration, nickel electrode capacity and all other experimental parameters were the same, voltage-capacity curves give valuable information about zinc electrode electrochemical behavior. Compared to cells with zinc electrodes prepared by ZnO powders synthesized from ZnCl<sub>2</sub> and Zn(NO<sub>3</sub>)<sub>2</sub>·6H<sub>2</sub>O, cells with electrodes prepared with commercial ZnO powder shows consistent discharge behavior and higher capacity.

In comparison with PVA-based zinc electrodes, the proposed PEG-based zinc electrode dramatically shows a higher discharge capacity at the same conditions. The discharge curves of NiZn batteries containing ZnO powder synthesized from ZnCl<sub>2</sub> and binder, PEG and PVA, with different concentrations are shown in Figure 9a. These kinds of batteries with PVA as a binder exhibit lower discharge capacity than those with PEG. The zinc electrode containing ZnO powder synthesized from ZnCl<sub>2</sub> and 6 wt.% PEG shows better specific capacity of 255 mAhg<sup>-1</sup> than the other loading of PEG. Similarly, the specific capacity of zinc electrode containing same ZnO powder and 6 wt.% PVA (155 mAhg<sup>-1</sup>) is more than the other loading of PVA. Furthermore, the

discharge plateaus of the batteries with PEG are smoother than those with PVA. The discharge curves of zinc electrode containing ZnO powder synthesized from  $\text{Zn}(\text{NO}_3)_2 \cdot 6\text{H}_2\text{O}$  with different PEG and PVA concentrations are shown in Figure 9b. These kinds of batteries with PVA exhibit lower discharge capacity than with PEG. The zinc electrode containing the same synthesized ZnO powder and 12wt.% PEG reaches higher discharge capacity of  $275 \text{ mAhg}^{-1}$  compared to those with other PEG concentrations, whereas these kind of zinc electrode with 3 wt.% PVA shows higher specific capacity of  $180 \text{ mAhg}^{-1}$  than those with other PVA concentrations. Zinc electrodes using commercial ZnO powder and PEG as a binder show the high discharge plateau, which means high output energy and power, and average discharge capacity of  $311 \text{ mAhg}^{-1}$ , as illustrated in Figure 9c.

The ZnO morphology and selected binders definitely have an impact on the electrochemical performance of the batteries in terms of high discharge capacity.



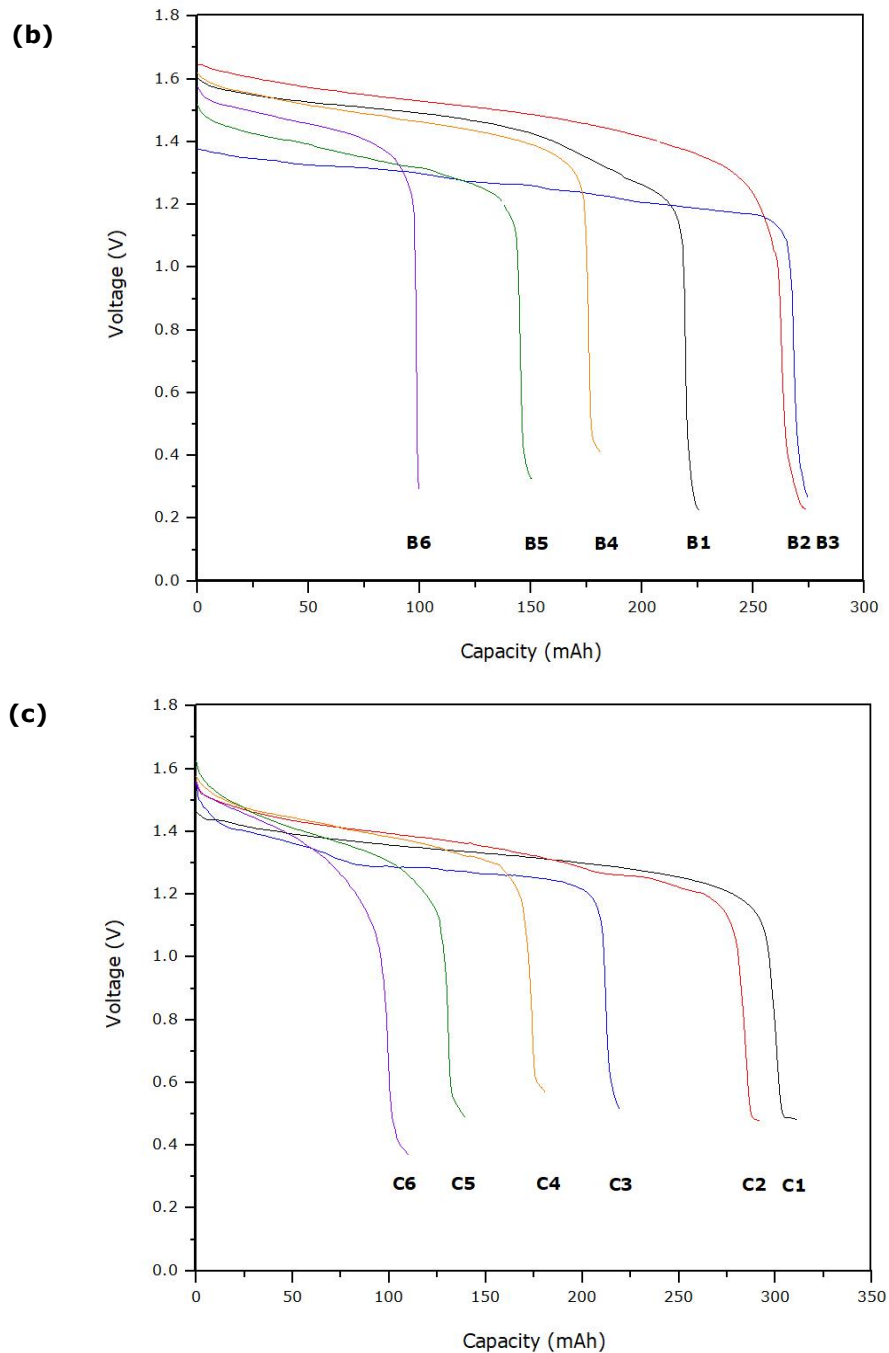


**Figure 9:** The discharge curves of NiZn batteries for (a) ZnO synthesized ZnCl<sub>2</sub>, (b) ZnO synthesized Zn(NO<sub>3</sub>)<sub>2</sub>·6H<sub>2</sub>O, (c) commercial ZnO.

Based on the results of discharge capacity for all NiZn batteries, initial morphology of zinc electrode as well as type and loading of binder material plays a role in battery performance. Additionally, electrode surface area available for electrochemical reactions causes the change in discharge performance of battery. The increase in the surface area of zinc electrode exhibits the increase in materials utilization and power density and the reduction of passivation at high discharge rates in NiZn batteries [23, 32]. High surface area of zinc electrode can improve battery performance due to short ion transport length for both electron and zinc ion transport,

high electrode/electrolyte contact area and easy charge transfer reaction on electrode-electrolyte interface [33-36].

The test setup was based on pouch cells and liquid KOH electrolyte. This setup is far from the ideal battery configuration (AA size or prismatic almost dry cell) however; it still provides valuable information regarding to zinc electrode behavior. Due to high internal resistivity of the cells used this study, voltage and current values measured during testing are far from commercial NiZn batteries. On the other hand, isolation of zinc electrode from nickel electrode in this setup by a large amount of potassium hydroxide solution prevented passivation of zinc electrode at high discharge rates.

## CONCLUSION

In this study, the influence of the binder on the electrochemical behavior of zinc electrode for pouch cell NiZn battery was investigated. By comparison with the types and loading of binders in zinc electrodes, the electrochemical properties of the electrodes were evaluated by charge/discharge cycling test. Clearly, binder loading and binder type have an effect on electrode discharge capacity. Based on these findings related to all zinc electrodes, the following conclusions can briefly be made:

- As investigated the results of zinc electrode including commercial ZnO powder, the PEG loading of 3 wt.% exhibits the maximum discharge capacity of  $311 \text{ mAg}^{-1}$ . The specific discharge capacity of these zinc electrodes decreases gradually accompanied with the increasing loading of PEG. Additionally, the discharge capability of PEG as a binder shows more efficient than that of PVA. Similar to result of PEG behavior, the increase in the PVA loading leads to reduce the discharge capacity of this kind of zinc electrodes.
- Among all results of zinc electrode containing ZnO powder synthesized from  $\text{Zn}(\text{NO}_3)_2 \cdot 6\text{H}_2\text{O}$  as a precursor, the PEG loading of 12 wt.% shows the highest specific discharge capacity of  $275 \text{ mAg}^{-1}$ . At the same time, the discharge capacity of this kind of zinc electrode is approximately the same as that when using a PEG loading of 6 wt.% and 12wt.%. These kinds of zinc electrodes with PVA as a binder exhibit lower discharge capacity than those with PEG. The specific discharge capacity of these zinc electrodes decreases with increasing PVA loading.
- Compared to the results of zinc electrode using commercial ZnO powder and synthesized ZnO powder from  $\text{Zn}(\text{NO}_3)_2 \cdot 6\text{H}_2\text{O}$  as a precursor, the discharge capacity of zinc electrode using synthesized ZnO powder from  $\text{ZnCl}_2$  displays different behavior. For discharge capacity, zinc electrode using synthesized ZnO powder from  $\text{ZnCl}_2$  and 6 wt.% of PEG as a binder exhibits the highest capacity of  $255 \text{ mAg}^{-1}$ , however, other loading of PEG (3 and 12 wt.%) for this kind of zinc electrode give dramatically lower discharge capacity. It could be said that PEG as a binder used in zinc electrode with synthesized ZnO powder from  $\text{ZnCl}_2$  performs better performance than PVA. The discharge capacity delivered by

this kind of zinc electrode with 6 wt.% PVA ( $157 \text{ mAhg}^{-1}$ ) is more than those with other PVA loading (3 and 12 wt.%).

It was concluded that the specific discharge capacity of zinc electrode for pouch cell NiZn battery is not only dependent on the binder loading and type, but also the initial morphology of ZnO powder.

## **ACKNOWLEDGEMENTS**

The authors are thankful Dr. Ogan Ocali and Prof. Dr. Muhsin Çiftçioğlu for their valuable advice, comments and discussions. We thank Ocali A.S. for financial support to perform this work.

## **REFERENCES**

1. Huang H, Zhang L, Zhang WK, Gan YP, Shao H. Preparation and electrochemical properties of ZnO/conductive-ceramic nanocomposite as anode material for Ni/Zn rechargeable battery. *J Power Sources*. 2008 Oct; 184:663-7. DOI: 10.1016/j.jpowsour.2008.01.004.
2. Cheng J, Zhang L, Yang YS, Wen YH, Cao GP, Wang XD. Preliminary study of single flow zinc-nickel battery. *Electrochem Commun*. 2007 Nov; 9:2639-42. DOI: 10.1016/j.elecom.2007.08.016.
3. Zhang XG, editor. *Corrosion and Electrochemistry of Zinc*. Springer; 1996. ISBN: 1475798784.
4. Huggins RA, editor. *Advanced Batteries*. Springer; 2009. ISBN: 9780387764238.
5. Acton QA, editor. *Sulfur Acids-Advances in Research and Application: 2013 Edition*. Scholarly Editions; 2013. ISBN: 978-1-481-69276-2.
6. Müller S, Holzer F, Haas O. Optimized zinc electrode for the rechargeable zinc-air battery. *J Appl Electrochem*. 1998 Sept; 28: 895-8. DOI: 10.1023/A:1003464011815.
7. Yuan YF, Tu JP, Wu HM, Li Y, Shi DQ, Zhao XB. Effect of ZnO nanomaterials associated with  $\text{Ca}(\text{OH})_2$  as anode material for Ni-Zn batteries. *J Power Sources*. 2006 Sept; 159:357-60. DOI: 10.1016/j.jpowsour.2006.04.010.
8. Shivkumar R, Paruthimal Kalaigan G, Vasudevan T. Studies with porous zinc electrodes with additives for secondary alkaline batteries. *J Power Sources*. 1998 Sept; 75:90-100. DOI: 10.1016/S0378-7753(98)00096-2.
9. McBreen J, Gannon E. The electrochemistry of metal oxide additives in pasted zinc electrodes. *Electrochim Acta*. 1981 Oct; 26 1439-46. DOI: 10.1016/0013-4686(81)90015-3.

10. Shivkumar R, Kalaignan GP, Vasudevan T. Effect of additives on zinc electrodes in alkaline battery systems. *J Power Sources*. 1995 May; 55:53-62. DOI: 10.1016/0378-7753(94)02170-8.
11. Adler TC, McLarnon FR, Cairns EJ. Low-zinc-solubility electrolytes for use in zinc/nickel oxide cells. *J Electrochem Soc*. 1993 Oct; 140:289-94. DOI: 10.1149/1.2221039.
12. Iwakura C, Murakami H, Nohara S, Furukawa N, Inoue H. Charge–discharge characteristics of nickel/zinc battery with polymer hydrogel electrolyte. *J Power Sources*. 2005 Dec; 152, 291-294. DOI: 10.1016/j.jpowsour.2005.03.175.
13. Yuan YF, Tu JP, Wu HM, Li Y, Shi DQ. Size and morphology effects of ZnO anode nanomaterials for Zn/Ni secondary batteries. *Nanotechnology*. 2005 Apr; 16:803-8. DOI: 10.1088/0957-4484/16/6/031.
14. Yang JL, Yuan YF, Wu HM, Li Y, Chen YB, Guo SY. Preparation and electrochemical performances of ZnO nanowires as anode materials for Ni/Zn secondary battery. *Electrochim Acta*. 2010 Sept; 55:7050-4. DOI: 10.1016/j.electacta.2010.06.075.
15. Perez MG, O’Keefe MJ, O’Keefe T, Ludlow D. Chemical and morphological analyses of zinc powders for alkaline batteries. *J Appl Electrochem*. 2006 Feb; 37:225-31. DOI: 10.1007/s10800-006-9239-3.
16. Yuan YF, Tu JP, Wu HM, Li Y, Shi DQ, Zhao XB. Effect of ZnO nanomaterials associated with Ca(OH)<sub>2</sub> as anodematerial for Ni–Zn batteries. *J Power Sources*. 2006 Sept; 159:357-60. DOI: 10.1016/j.jpowsour.2006.04.010.
17. Yang CC, Chien WC, Wang CL, Wu CY. Study the effect of conductive fillers on a secondary Zn electrode based on ball-milled ZnO and Ca(OH)<sub>2</sub> mixture powders. *J Power Sources*. 2007; 172:435-45. DOI: 10.1016/j.jpowsour.2007.07.053.
18. Yuan YF, Yu LQ, Wu HM, Yang JL, Chen YB, Guo YB, Tu JP. Electrochemical performances of Bi based compound film-coated ZnOas anodic materials of Ni–Zn secondary batteries. *Electrochim Acta*. 2011 Apr; 56:4378-83. DOI: 10.1016.j.electacta.2011.01.006.
19. Shivkumar R, Kalaignan GP, Vasudevan T. Studies with porous zinc electrodes with additives for secondary alkaline batteries. *J Power Sources*. 1998 Sept; 75:90–100, DOI: 10.1016/S0378-7753(98)00096-2.
20. Lee SH, Yi CW, Kim K. Characteristics and electrochemical performance of the TiO<sub>2</sub>-coated ZnO anode for Ni–Zn secondary batteries. *J Phys Chem C*. 2011 Dec; 115:2572–7, 2011. DOI: 10.1021/jp110308b.
21. Zeng D, Yang Z, Wang S, Ni X, Ai D, Zhang Q. Preparation and electrochemical performance of In-doped ZnO as anode material for Ni–Zn secondary cells. *Electrochim Acta*. 2011 Apr; 56:4075–80. DOI: 10.1016/j.electacta.2011.01.119.

22. Hilder M, Winther-Jensen B, Clark NB. The effect of binder and electrolyte on the performance of thin zinc-air battery. *Electrochim Acta*. 2012 May; 69:308-14. DOI:10.1016/j.electacta.2012.03.004.
23. Masri MN, Nazeri MFM, Ng CY, Mohamad AA. Tapioca binder for porous zinc anodes electrode in zinc-air batteries. *J King Saud University—Engineering Sci*. 2015 July; 27:217-24. DOI: 10.1016/j.jksues.2013.06.001.
24. Lee CW, Eom Sw, Sathiyarayanan K, Yun MS. Preliminary comparative studies of zinc and zinc oxide electrodes on corrosion reaction and reversible reaction for zinc/air fuel cells. *Electrochim Acta*. 2006 Dec; 52:1588-91. DOI: 10.1016/j.electacta.2006.02.063.
25. Müller S, Holzer F, Haas O. Optimized zinc electrode for the rechargeable zinc-air battery. *J Appl Electrochem*. 1998 Sept ; 28:895-8. DOI: 10.1023/A:1003464011815.
26. Wu GM, Lin SJ, Yang CC. Alkaline Zn-air and Al-air cells based on novel solid PVA/PAA polymer electrolyte membranes. *J Membr Sci*. 2006 Sept; 280:802-8. DOI: 10.1016/j.memsci.2006.02.037.
27. Yang CC, Lin SJ. Alkaline composite PEO-PVA-glassfibre-mat polymer electrolyte for Zn-air battery. *J Power Sources*. 2002 Nov; 112:497-503. DOI: 10.1016/S0378-7753(02)00438-X.
28. Masri MN, Mohamad AA. Effect of adding potassium hydroxide to an agar binder for use as the anode in Zn-air batteries. *Corros Sci*. 2009 Dec; 51:3025-9. DOI: 10.1016/j.corsci.2009.08.027.
29. Ein-Eli Y, Auinat M, Starosvetsky D. Electrochemical and surface studies of zinc in alkaline solutions containing organic corrosion inhibitors. *J Power Sources*, 2003 Mar; 114:330-7. DOI: 10.1016/S0378-7753(02)00598-0.
30. Saleem M, Sayyad MH, Karimov KHS, Ahmad Z. Fabrication of investigation of the charge-discharge characterization of Zinc-PVA-KOH-Carbon Cell. *Acta Phys Pol A*. 2009 Dec; 116:1021-4. DOI: 10.12693/APhys/PolA.116.1021.
31. Wu Q, Zhang J, Sang S. Preparation of alkaline solid polymer electrolyte based on PVA-TiO<sub>2</sub>-KOH-H<sub>2</sub>O and its performance in Zn-Ni battery. *J Phys and Chem Solids*. 2008 Nov; 69, 2691-5. DOI: 10.1016/j.jpcs.2008.06.132.
32. Payer G, Ebil Ö. Zinc electrode morphology evolution in high energy density nickel-zinc batteries. *J Nanomater*. 2016 Feb; 2016:1-9. DOI: 10.1155/2016/1280236.
33. Brett CMA, Brett AMO, editor. *Electrochemistry: Principles, Methods, and Applications*. Oxford University Press; 1994. ISBN: 978-0198553885.
34. Gileadi E, editor. *Electrode Kinetic for Chemists, Chemical Engineers, and Materials Scientists*. John Wiley & Sons; 1993. ISBN: 978-0-471-18858-2.

35. Minakshi M, Appadoo D, Martin DE. The anodic behavior of planar and porous zinc electrodes in alkaline electrolyte. *Electrochem Solid-State Lett.* 2010 Jan; 13:A77-80. DOI: 10.1149/1.3387672.

36. Chen T, Pan L, Loh TAJ, Chua DHC, Yao Y, Chen Q, Li D, Qin W, Sun Z. Porous nitrogen-doped carbon microspheres as anode materials for lithium ion batteries. *Dalton Trans.* 2014 Jun; 43:14931-3-5. DOI: 10.1039/C4DT01223B.





## EFFECT OF ANNEALING TEMPERATURES ON THE CRYSTALLIZATION AND PHOTOCATALYTIC ACTIVITY OF MICRO-NANOPOROUS TiO<sub>2</sub> FILMS PRODUCED BY ELECTROCHEMICAL ANODIZATION

Melis Yurddaskal<sup>1\*</sup>, Metin Yurddaskal<sup>2,3</sup>, Tuncay Dikici<sup>3</sup> and Hulya Durmus<sup>4</sup>

<sup>1</sup>Celal Bayar University, Department of Mechanical Engineering, Muradiye, 45140, Manisa, Turkey

<sup>2</sup>Dokuz Eylul University, The Graduate School of Natural and Applied Sciences, Buca, 35390, Izmir, Turkey

<sup>3</sup>Dokuz Eylul University, Center for Fabrication and Applications of Electronic Materials (EMUM), Buca, 35390, Izmir, Turkey

<sup>3</sup> Izmir Katip Celebi University, Department of Materials Science and Engineering, Cigli, 35620, Izmir, Turkey

<sup>4</sup>Celal Bayar University, Department of Metallurgical and Materials Engineering, Muradiye, 45140, Manisa, Turkey

*(This article first appeared in PPM2017 and was accepted as a non-peer-reviewed manuscript to be published in JOTCSA)*

**ABSTRACT:** In this study, micro-nanoporous TiO<sub>2</sub> films were prepared by electrochemical anodization of titanium (Gr-2) in an aqueous solution containing 0.5 wt. % HF solution at a constant potential of 30 V and then annealed in ambient air at 500, 600, 700 and 800 °C for 2 h to obtain crystalline structures. The crystalline phase and surface morphology of the samples were characterized by X-ray diffraction (XRD) and scanning electron microscope (SEM). The photocatalytic performances of the samples were evaluated by the photocatalytic degradation of aqueous methylene blue (MB) solutions under UV light illumination for different periods. XRD results indicated that at annealing temperatures higher than 600°C, anatase started to transform into rutile. Increasing annealing temperatures resulted in reduced micro-nanopores diameter and increased wall thickness. At 800°C, the structure completely disappeared. The results demonstrated that changes in both the crystalline structure and surface morphology have a strong influence on the photoactivity of the nanostructured TiO<sub>2</sub> films.

**Keywords:** Nanostructured TiO<sub>2</sub>; anatase; surface morphology; photocatalytic; methylene blue.

**Cite this:** Yurddaskal M, Yurddaskal M, Dikici T, Durmuş H. EFFECT OF ANNEALING TEMPERATURES ON THE CRYSTALLIZATION AND PHOTOCATALYTIC ACTIVITY OF MICRO-NANOPOROUS TiO<sub>2</sub> FILMS PRODUCED BY ELECTROCHEMICAL ANODIZATION. JOTCSA. 2017;5(sp.is.1):85–92.

**Corresponding author. E-mail:** [melis.yurddaskal@cbu.edu.tr](mailto:melis.yurddaskal@cbu.edu.tr).

## INTRODUCTION

In 1972, titanium dioxide has been considerable investigated as a semiconductor photocatalyst for solar energy conversion and environmental purification since Fujishima and Honda discovered the photocatalytic splitting of water on TiO<sub>2</sub> electrodes in 1972 [Fujishima and Honda, 1972]. Among various oxide semiconductor photocatalytic materials, TiO<sub>2</sub> is widely used for pollution control because of its high physical stability, chemical inertness, low cost, and non-toxicity and strong oxidizing power under UV light irradiation [Fujishima *et al.*, 2000, Linsebigler *et al.*, 1995, Chen and Mao, 2007]. TiO<sub>2</sub> has three nature crystallographic phases: anatase (tetragonal), rutile (tetragonal) and brookite (orthorhombic). Among these crystal structures of TiO<sub>2</sub>, anatase phase is generally considered to be more active than rutile phase for TiO<sub>2</sub> photocatalysts due to its lower surface energy than rutile [Ahmed, 2012]. Rutile is the most thermodynamically stable phase, whereas anatase and brookite are metastable phases and could be transformed into rutile easily by thermal treatment [Beltran *et al.*, 2006].

Nanostructured TiO<sub>2</sub> thin films are usually prepared by sol-gel processing, chemical vapor deposition (CVD), liquid-phase deposition (LPD) methods and ion-beam synthesis methods [Tomandl *et al.*, 2000, Yu *et al.*, 2003, Komarov *et al.*, 2005]. Recently, highly ordered TiO<sub>2</sub> thin films prepared by a simple electrochemical anodization over a titanium substrate in a fluoride containing electrolyte in 2001. This method is a cost effective, versatile, easy, controllable and reproducible technique. This method is also possible to arrange the size and shape of nanopore arrays to the targeted dimensions [Gong *et al.*, 2001, Indira *et al.*, 2012].

Many new types of TiO<sub>2</sub>-based photocatalysts have been reported in recent years, including, nanotubes [Liu *et al.*, 2008], nanofibers [Liu *et al.*, 2007], nanosheets (TNSs) [Matsumoto *et al.*, 2009], porous anodized films [Masahashi *et al.*, 2009], nanowire arrays [Yu *et al.*, 2009], nanograined thin films [Ryu *et al.*, 2008], mesoporous structures [Pan and Lee, 2006] and hierarchical micro- and nanoporous structures [Zhao *et al.*, 2008]. It is known that morphology control of TiO<sub>2</sub>-based photocatalysts is usually one of the important research directions. This study examines the influence of annealing temperatures on the photocatalytic activity of TiO<sub>2</sub> films grown on titanium substrates by anodization, with the aim of achieving a high photocatalytic performance.

Herein, we prepared the micro-nanoporous TiO<sub>2</sub> films by electrochemical anodization of titanium substrates and then annealed in ambient air at 500, 600, 700 and 800 °C. The

effects of annealing temperature on the crystallization, morphology and photocatalytic activity of TiO<sub>2</sub> films were investigated and discussed. The photocatalytic properties were evaluated using MB as the target pollutant.

## EXPERIMENTAL

The commercially pure titanium (Cp-Gr 2) substrates with diameters of 25 mm and 5 mm thickness were used as anode. After polishing process, the samples were cleaned ultrasonically in ethanol, acetone and deionized (DI) water for each 15 min and finally washed by distilled water. Prior to the anodization process, the samples were degreased in a mixture of nitric acid and hydrofluoric acid solutions for ten seconds to remove the air-formed oxide layer.

The anodization was performed in a solution consisting 0.5 wt. % HF solution at 30 V for 30 min in two-electrode configuration connected to a DC power supply at room temperature. After electrochemical anodization, all the anodized films were calcined at 500, 600, 700 and 800 °C in air for 2 h.

X-ray diffraction patterns of all samples were recorded to identify the phase structures with the aid of an X-ray diffractometer having a CuK<sub>α</sub> characteristic radiation source (XRD, Thermo-Scientific, ARL K<sub>α</sub>). Diffraction patterns were acquired in the range of 10° to 80° with a scanning rate of 2°/min. The X-ray radiation of Cu-K<sub>α</sub> was set at 45 kV and 44 mA. The surface morphology and microstructure of the samples were characterized by a scanning electron microscope (SEM, COXEM EM-30 Plus).

The photodegradation of MB experiments were exploited in a homemade reactor which was surrounded a cooling system to keep the photocatalytic reaction system at room temperature. All tests were performed using a light source (Osram, UltraVitalux E27, 300W). The films were placed into beakers containing 30 ml of MB aqueous solution. The initial concentration of MB is 3 mg/L corresponding to 10<sup>-5</sup> M (pH = 8). The distance between the lamp and the beakers was kept at 20 cm for all specimens. During the whole reaction, 3 ml of the MB aqueous solution from each beaker was extracted at an interval of 1 h in order to measure the absorption spectra of MB. The absorption of the MB solutions was conducted and analyzed by a UV-1240 Shimadzu spectrophotometer based on the characteristic absorption of MB peak at 664 nm.

## RESULTS AND DISCUSSION

Fig. 1 depicts the XRD patterns of the micro-nanoporous TiO<sub>2</sub> films annealed at different temperature. It was observed that the microporous layers exhibited mixed crystalline structures consisting of anatase, rutile and metallic Ti from the substrate. It was observed that the main diffraction peaks at 25.38 (101) and 37.96 (004) which correspond to crystal structure of anatase for the samples annealed at 500 °C and 600 °C [Kenanakis, *et al.*, 2015]. When the annealing temperature increased, the intensity of anatase decreased in the samples and crystalline phase of micro-nanoporous TiO<sub>2</sub> films was predominantly rutile. It must also be noted that metallic titanium peaks observed in patterns that can be associated to X-ray penetration into the substrates on which surface modifications were made.

It is known that surface morphology is of great influence on catalysts' photocatalytic activity. Fig.2 shows the SEM micrographs of the micro-nanoporous TiO<sub>2</sub> films. The shapes of TiO<sub>2</sub> micro- and nanopores exhibited a noticeable change with increasing annealing temperature. With further increasing of the annealing temperature to 800 °C, pores were destroyed and started to disappear.

As mentioned before, the MB dye was used to assess the photocatalytic performance of the prepared micro-nanoporous TiO<sub>2</sub> films annealed at different temperature.

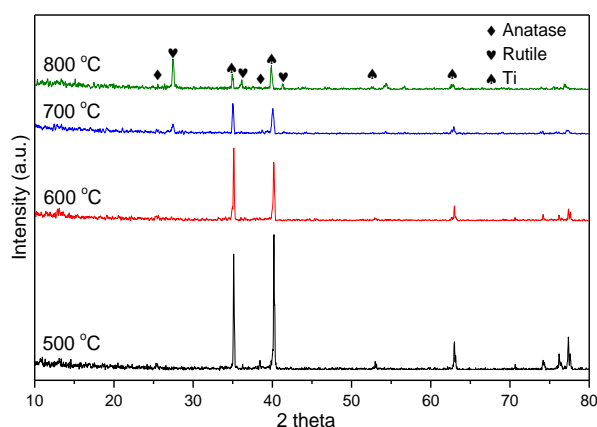


**Figure 1:** XRD patterns of the micro-nanoporous TiO<sub>2</sub> films annealed at different temperatures.

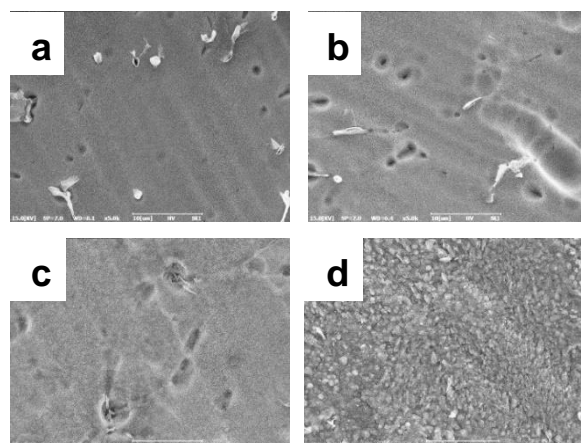


**Figure 2:** SEM images of TiO<sub>2</sub> films annealed at (a) 500 °C (b) 600 °C (c) 700 °C and (d) 800 °C.

Fig. 3 shows the photocatalytic degradation of MB by the micro nanoporous TiO<sub>2</sub> films annealed at different temperatures. Considering the annealing temperatures of the films, the sample annealed at 600 °C has the best photocatalytic activity and SEM photographs support these results. Fig 4 shows the photocatalytic kinetics of the TiO<sub>2</sub> films micro-nanoporous TiO<sub>2</sub> films annealed at different temperatures. Photocatalytic degradation kinetics were calculated from Langmuir–Hinshelwood kinetics model that express the first order reaction kinetics for the samples. With this approach, it can be inferred that the higher the slope of the linear plot, the higher the degradation reaction rate.

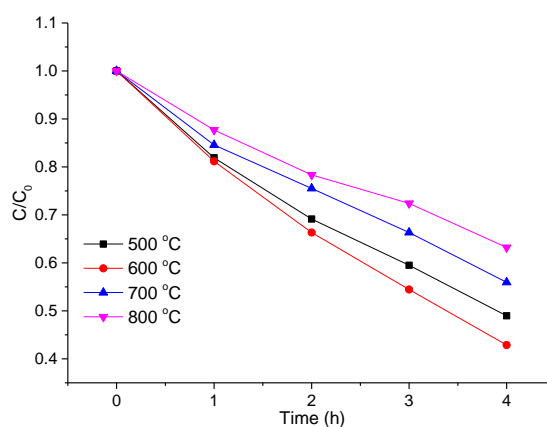


**Figure 3:** Photocatalytic degradations of the TiO<sub>2</sub> films micro-nanoporous TiO<sub>2</sub> films annealed at different temperatures.

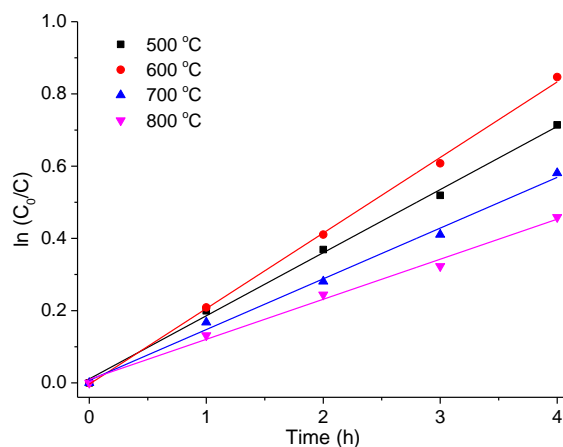


**Figure 4:** Photocatalytic kinetics of the TiO<sub>2</sub> films micro-nanoporous TiO<sub>2</sub> films annealed at different temperatures.

**Table 1:** Photocatalytic parameters of the samples.

Annealing temperature (°C)	Kinetic rate constant (k) (h <sup>-1</sup> )	R <sup>2</sup>
500	0.1748	0.9971
600	0.2093	0.9985
700	0.1405	0.9935
800	0.1109	0.9916

It can be understood from the Fig. 4; all samples are good agreement with the first order kinetics. The photocatalytic parameters of the samples were given in Table 1. The film annealed at 600 °C proved to be the best photocatalyst among the samples annealed from 500 °C to 800 °C. The photocatalytic activity of TiO<sub>2</sub> structures depends on several factors such as surface area, crystallinity, phase composition and crystal orientation [Dikici *et al.*, 2015].

## CONCLUSION

It can be concluded that the structural properties of the films determined the best photocatalyst in this work. Annealing temperature of the 600 °C for 2 h in air is the best heat treatment regime that the anatase phase is predominant and rutile is the newly formed for the sample with higher surface area. Low anatase/rutile ratio is better for the photoactivity of micro-nanoporous TiO<sub>2</sub> films.

## REFERENCES

- Ahmed M.A., 2012, Synthesis and structural features of mesoporous NiO/TiO<sub>2</sub> nanocomposites prepared by sol-gel method for photodegradation of methylene blue dye, *J. Photochem. Photobiol. A* 238 63–70.
- Beltran A., Gracia L., Andres J., 2006, Density functional theory study of the brookite surfaces and phase transitions between natural titania polymorphs, *J. Phys. Chem. B* 46 23417-23423.
- Chen X.B., Mao S.S., 2007, Titanium dioxide nanomaterials: synthesis, properties, modifications, and applications, *Chem. Rev.* 107 2891.
- Dikici, T, Yildirim, S., Yurddaskal, M., Erol, M., Yigit, R., Toparli, M. and Celik, E., 2015, A comparative study on the photocatalytic activities of microporous and nanoporous TiO<sub>2</sub> layers prepared by electrochemical anodization, *Surf. & Coat. Tech.* 263 1.
- Fujishima A., Honda K., 1972, *Nature* 238 637.
- Fujishima A., Rao T.N., Tryk D.A., 2000, Titanium dioxide photocatalysis, *J. Photochem. Photobiol. C Rev.* 1 1–21.
- Gong D., Grimes C.A., Varghese O.K., Hu W.C., Singh R.S., Chen Z., Dickey E.C., 2001, *J. Mater. Res.* 16 3331.
- Indira K., Ningshen S., Mudali U.K., Rajendran N., 2012, Effect of anodization parameters on the structural morphology of titanium in fluoride containing electrolytes, *Mater. Charac.* 71 58-65.
- Kenanakis G., Vernardou D., Dalamagkas A., Katsarakis N., 2015, Photocatalytic and electrooxidation properties of TiO<sub>2</sub> thin films deposited by sol-gel *Catal. Today*, 240, 146-152
- Komarov F.F., Vlasukova L.A., Milchanin O.M., Gaiduk P.I., Yuvchenko V.N., Grechnyi S.S., 2005, Ion-beam formation of nanopores and nanoclusters in SiO<sub>2</sub>, *Vacuum* 78 361.
- Linsebigler A.L., Lu G.Q., Yates J.T., 1995, Photocatalysis on TiO<sub>2</sub> surfaces: principles, mechanisms, and selected results, *Chem. Rev.* 95 735–758.
- Liu Z.Y., Sun D.D., Guo P., Leckie J.O., 2007, An efficient bicomponent TiO<sub>2</sub>/SnO<sub>2</sub> nanofiber photocatalyst fabricated by electrospinning with a side-by-side dual spinneret method, *Nano Lett.* 7 1081–1085.
- Liu Z.Y., Zhang X.T., Nishimoto S., Jin M., Tryk D.A., Murakami T., Fujishima A., 2008, Highly ordered TiO<sub>2</sub> nanotube arrays with controllable length for photoelectrocatalytic degradation of phenol, *J. Phys. Chem. C* 112 253-259.
- Masahashi N., Mizukoshi Y., Semboshi S., Ohtsu N., 2009, Enhanced photocatalytic activity of rutile TiO<sub>2</sub> prepared by anodic oxidation in a high concentration sulfuric acid electrolyte, *Appl. Catal. B: Environ.* 90 255-261.
- Matsumoto Y., Koinuma M., Iwanaga Y., Sato T., Ida S., 2009, N Doping of oxide nanosheets, *J. Am. Chem. Soc.* 131 6644–6645
- Pan J.H., Lee W.I., 2006, Preparation of highly ordered cubic mesoporous WO<sub>3</sub>/TiO<sub>2</sub> films and their photocatalytic properties, *Chem. Mater.* 18 847-853.
- Ryu J., Park D.S., Hahn B.D., Choi J.J., Yoon W.H., Kim K.Y., Yun H.S., 2008, Photocatalytic TiO<sub>2</sub> thin films by aerosol-deposition: From micron-sized particles to nano-grained thin film at room temperature, *Appl. Catal. B: Environ.* 83 1-7.
- Tomandl G., Mangler M., Pippel E., Woltersdorf J., 2000, Evidence of nanopores in sol-gel based TiO<sub>2</sub> and TiN ultrafiltration membranes, *Mater Chem Phys* 63 139–144.

Yu H., Chen S., Quan X., Zhao H., Zhang Y., 2009, Silicon nanowire/TiO<sub>2</sub> heterojunction arrays for effective photoelectrocatalysis under simulated solar light irradiation, Appl. Catal. B: Environ. 90 242-248.

Yu J.G., Yu H.G., Cheng B., Zhao X.J., Yu J.C., Ho W.K., 2003, J. Phys. Chem. B 107 13871.

Zhao Y., Zhang X., Zhai J., He J., Jiang L., Liu Z., Nishimoto S., Murakami T., Fujishima A., Zhu D., 2008, Enhanced photocatalytic activity of hierarchically micro-/nano-porous TiO<sub>2</sub> films, Appl. Catal. B: Environ. 83 24-29.



## SIMULATION OF CO-CURED MULTI-CELL COMPOSITE BOX BEAM MANUFACTURING VIA VARTM

Mert AKIN<sup>a</sup>, Merve ERDAL

Middle East Technical University, Department of Mechanical Engineering, Ankara, Turkey

*(This article first appeared in PPM 2017 and was accepted as a non-peer-reviewed manuscript to be published in JOTCSA)*

**Abstract:** Sub-structures of aircraft structures mainly consist of stiffened shells such as fuselage frames, ribs and multi-cell box beams. Conventionally, these stiffened shells are manufactured through a process wherein shells and stiffeners are fabricated separately and then are integrated either through mechanical fastening and adhesive bonding. Co-curing is an integral molding technique that can greatly reduce the part count and the final assembly costs for composite materials. This article presents a simulation of integral manufacturing of a three-cell composite box beam by vacuum assisted resin infusion process. To validate the model, the characterization tests of both resin and reinforcement materials were carried out. Porosity and permeability testing of the reinforcement materials were conducted. Moreover, the effect of stacking sequence and vacuum level on the preform porosity were investigated. Additionally, the resin viscosity measurements were performed and the influence of temperature and curing on resin viscosity were examined. Having obtained the characterization data, vacuum infusion model was validated using RTMWorx software and then simulation of a three-cell composite box beam was conducted.

**Keywords:** vacuum-assisted infusion process, model validation, vacuum infusion model.

**Cite this:** Akin M, Erdal M. SIMULATION OF CO-CURED MULTI-CELL COMPOSITE BOX BEAM MANUFACTURING VIA VARTM. JOTCSA. 2017;5(sp.is.1):93–102.

**\*Corresponding author.** E-mail: [mert.akin@metu.edu.tr](mailto:mert.akin@metu.edu.tr).

## INTRODUCTION

Sub-structures of aircraft structures are mainly consisted of stiffened shells such as fuselage frames, ribs and multi-cell box beams. Conventionally, these stiffened shells are manufactured through a process where shells and stiffeners are fabricated separately and then are integrated either through mechanical fastening or adhesive bonding. This conventional process is so-called Secondary Bonding.

Co-curing is an integral molding technique that can greatly reduce the part count and the final assembly costs for composite materials. Co-curing and its tooling technology proprietary in nature and details are mostly not open publicly. The very first application of this technology in literature is Japanese XF-2 fighter aircraft wing in late 1990s [Kageyama & Yoshida, 2000]. In the XF-2 fighter aircraft wing, spars and ribs were co-cured with the bottom skin. [Mahruz et al., 2004] developed a new process to manufacture composite skin-stringer assembly in one-step using VARTM.

VARTM is highly labor intensive and difficult process so that if injection and venting strategy is not properly configured, dry spots that regions with only dry fibers or racetracking problem can easily occur. Simulation of the resin flow will allow one to investigate the resin impregnation process and strategically design gates and vents and injection schemes to optimally fill the composite part without any dry spots. In this paper, simulation of a co-cured multi-cell composite box beam is investigated by using RTM-Worx resin flow simulation software. The manufacturing method of the multi-cell box beam is based on the procedure of [Mahruz et al., 2004] with slight modification.

## EXPERIMENTS

Both preform and resin characterization tests are carried out. For preform characterization, two sets of experiments are performed: (1) porosity experiments, and (2) permeability tests; whereas rheological experiments are made for the resin characterization.

### Materials

Materials used in characterization tests are given in Table 1.

**Table 1:** Resin and fabric materials used in characterization tests.

Reinforcement	Carbon Fiber, 1x1 Plain, 200g/m <sup>2</sup>
Resin	Huntsman XB3585- Aradur 3486
Peel Ply	Metyx PA80R1
Distribution	Metyx PE Flow
Media	Mesh

## Fabric Characterization Experiments

### *Porosity Experiments*

The term porosity of dry reinforcement material refers the amount of space in reinforcement that can be filled with resin. Porosity is often calculated as

$$\phi = 1 - V_f \quad (\text{Eq. 1})$$

Basically, the fiber volume fraction is a fraction of amount of fiber to the total volume and can be calculated as, (Bird, Stewart, & Lightfoot, 1960),

$$V_f = \frac{W}{hA_f\rho} \quad (\text{Eq. 2})$$

where,  $W$  is the sample mass in kg,  $h$  is the sample thickness in m, and  $A_f$  is the area of sample in m<sup>2</sup>,  $\rho$  is the density of fabric in kg/m<sup>3</sup>. The setup of porosity experiment is shown in Figure 1 and the results are given in Table 2.

### *Effect of Stacking Sequence on Porosity*

The effect of the number of preforms on preform porosity is investigated using two, five, seven and ten layers of 1x1 plain, 200gr/cm<sup>2</sup> carbon fiber preforms.

In order to calculate the porosity, first physical measurement of fabric is made. All fabrics are cut in 300mm x 400mm dimensions and each is weighted as 24 grams. The thickness of fabric is 0.3mm.

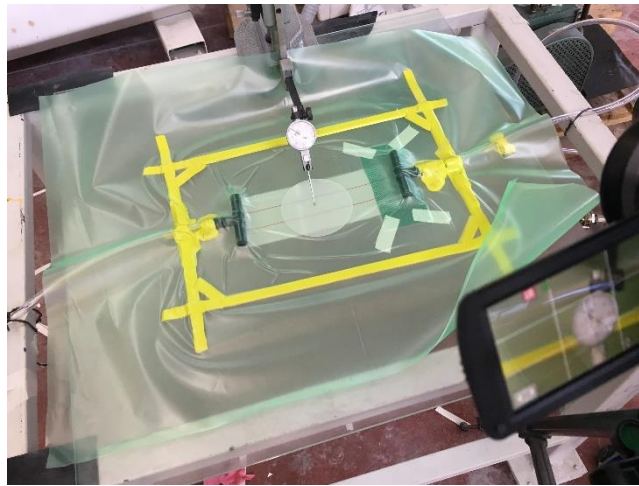


**Figure 1:** Porosity Experiment Set-up.

**Table 2:** Porosity experiment results.

Material Name	Superficial Density (g/cm <sup>2</sup> )	Porosity	Layer Thickness (mm)
Distribution Media	-	0.85	1.35
Peel Ply	80	0.35	0.2
Carbon Fiber Preform	200	0.52	0.3

Having obtained the physical properties, change in preform thickness is measured precisely using a dial gauge, shown in Figure 1. Vacuum is continued after the preform compaction for 10 minutes in order to reduce the nestling effect. Two sets of measurements are collected: (1) immediately after the vacuum is applied (2) after the 10minutes hold time. The results show a quasi-linear relation between the porosity and the number of layers, see Figure 2.

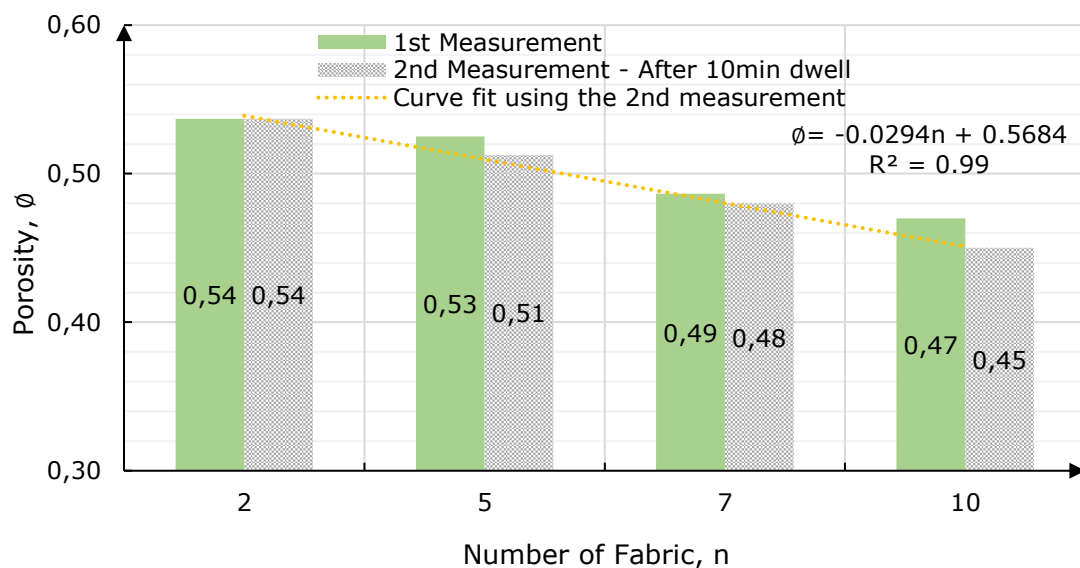


**Figure 2:** Porosity of carbon fiber fabric with respect to the number of layer count.

*Effect of Vacuum Level on Porosity*

Having analyzed the effect of the preform count, the effect of the vacuum level on preform porosity is investigated by changing the vacuum level from 13000Pa (100mmHg) to 93325Pa (700mmHg). Both peel ply, distribution media and carbon fiber preform are tested and the results are presented in Figure 3.

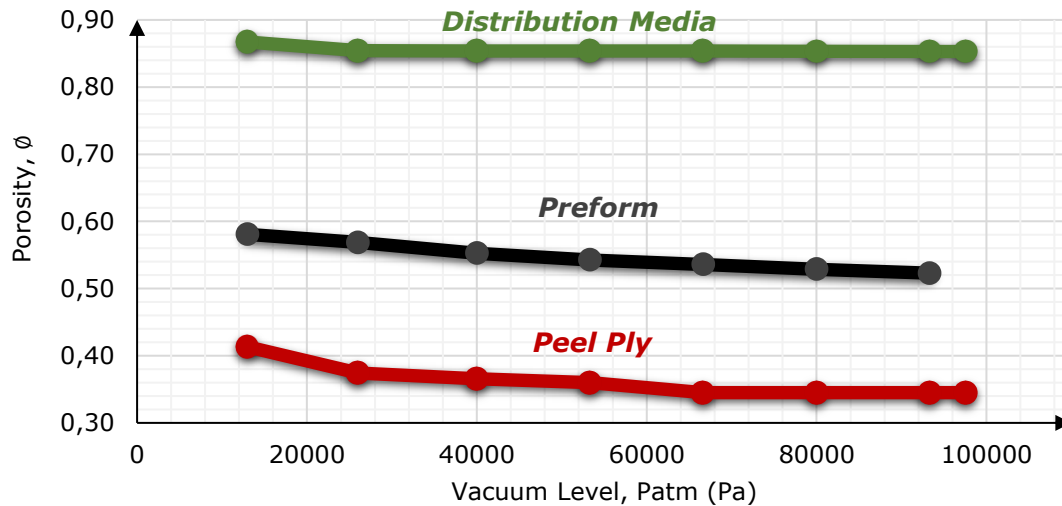


**Figure 3:** Porosity of layers with respect to vacuum level.

*Permeability Tests*

Permeability characterizes the ease with which a fluid can flow through a porous medium. In this paper, 1D channel flow method was used to determine permeability, which utilizes the following formulation (Rudd, Long, Kendall, & Mangin, 1997).

$$K = \frac{\mu \phi x_f^2}{2 \Delta p t_f} \quad (\text{Eq. 3})$$

where  $\mu$  is the resin viscosity in Pa.s,  $\phi$  is the fabric porosity,  $\Delta p$  is the pressure difference in Pa,  $x_f$  is the flow front in m and  $t_f$  is the time elapsed for flow front in s. The permeability test set-up is shown in Figure 4.

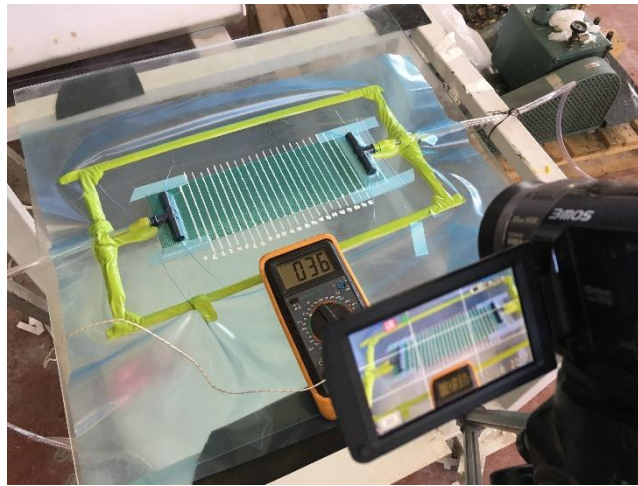


**Figure 4:** Permeability Test Set-up.

The porosity and resin viscosity data is taken from the experiments and the test results are tabulated in Table 3.

**Table 3:** Permeability Test Results.

Test Properties and Results	Distribution Media	Peel Ply	Carbon Fiber
Resin Temperature (°C)	36-37	54-55	35-40
Resin Viscosity (Pa.s)	0.3085	0.115	0.29
Porosity	0.85	0.35	0.54
Vacuum Pressure (Pa)	99325	97325	97325
$K_{11}$ (m <sup>2</sup> )	5.24E-09	2.06E-12	2.85E-12

### Resin Characterization Experiments

Rheological measurements for resin are conducted by using TA, AR2000 rheometer. Parallel circular plates having a diameter of 25mm with the maximum gap of 1mm under the flow mode are chosen in this study.

#### *Effect of Temperature on Viscosity*

To investigate the temperature effect on viscosity, temperature ramp test is carried out, whose results are seen in Figure 4. Equation (4) is the exponential curve fit acquired by the experiment.

$$\mu = 488235T^{-3.641}, R^2 = 0.998 \quad (\text{Eq. 4})$$

#### *Effect of Curing on Viscosity*

Since chemical reaction sets in, the resin starts the cross-binding process whereby its viscosity is increasing. In order to understand the curing effect on viscosity, resin with catalyst is tested additionally. The curve fit equation is given in Equation (5).

$$\mu = 819.34T^{-2.191}, R^2 = 0.976 \quad (\text{Eq. 5})$$

As shown in Figure 5, resin has lower viscosity when mixed with catalyst.

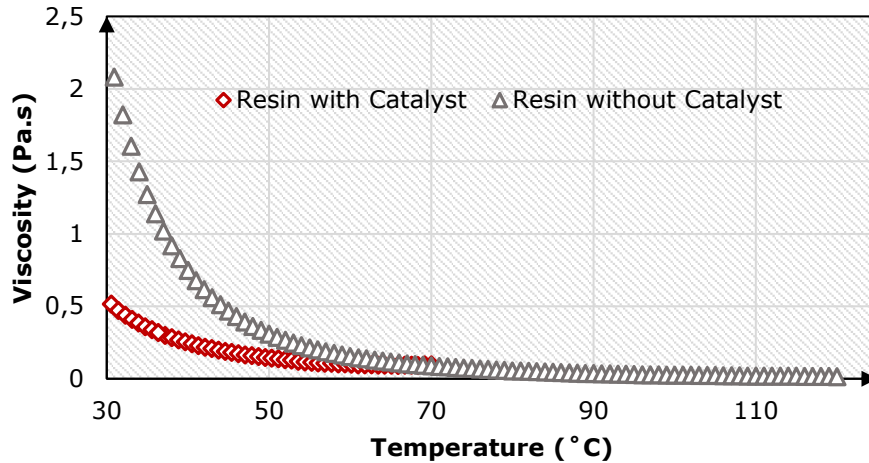


**Figure 5:** Resin with and without catalyst viscosities as a function of temperature.

Time hold test is furthermore conducted at 40°C, which is the process temperature, to better understand the time dependent characteristic of viscosity. Figure 6 presents the exponential characteristic of the viscosity and the curve fit equation is given in Equation (6).

$$\mu = 0.1669e^{(1.6102 \frac{t_{gel}}{t})}, R^2 = 0.999 \quad (\text{Eq. 6})$$

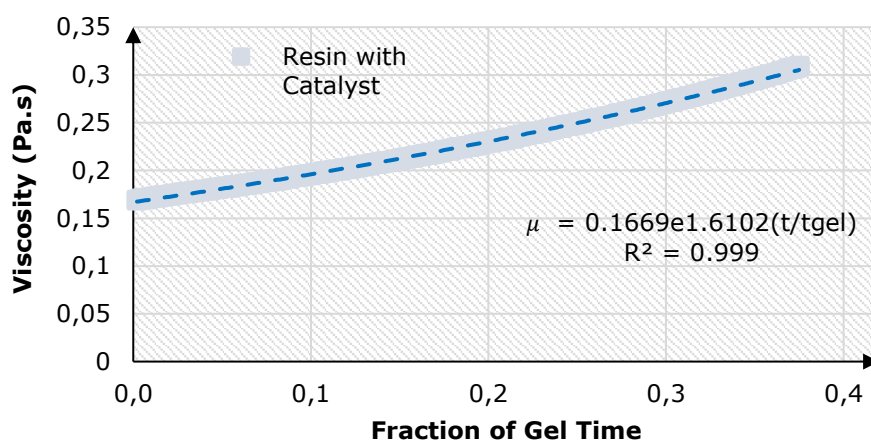


**Figure 6:** Resin with catalyst viscosity as a function of the normalized curing time.

## SIMULATION RESULTS AND DISCUSSION

The resin flow simulation of a co-cured multi-cell box beam is made by using RTMWorx software, which solves the governing Darcy's flow equation using Finite Element/Control Volume (FE/CV) technique. In this study, so-called  $2\frac{1}{2}$ D model, wherein resin flow in 3D space is considered as 2D, since resin flow through thickness is negligible, is constructed. Hereby, permeability averaging technique (Equation (7)), that is simply based on rule of mixture is used to average the permeability of fiber preform having the stacking sequence presenting in Figure 7.

$$\bar{K}_{uv} = \frac{1}{H} \sum_{j=1}^n h^{(j)} K_{uv}^{(j)} \quad (\text{Eq. 7})$$

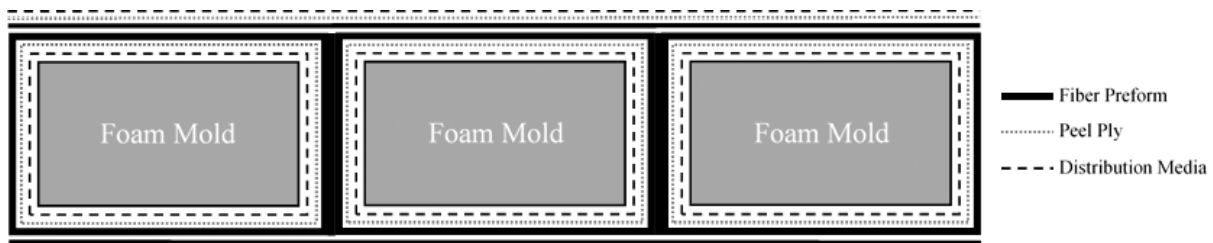


**Figure 7:** Schematic diagram of the stacking sequences of box beam.

The size of box beam is selected to be consistent with [Mahruz et. al., 2004] so that the webs are 50 mm high and 90 mm wide. The assembly is 288.3 mm wide, 500 mm long.

**Table 4:** Simulation Inputs.

Skin Thickness	2.1mm
Web Thickness	3.0mm
Side Web Thickness	1.5mm
Resin Viscosity	0.24 Pa.s
Pressure Difference	97325 Pa
Injection Line Diameter	14mm
Suction Line Diameter	14mm
Number of Elements	15292

In practice, a space needs to secure the injection line thereby the feed line is placed 30mm away from the edge, while the suction line is positioned along the opposite edge. The additional simulation parameters are stated in Table 4.

Figure 8 presents the results of flow simulation. The total fill time is calculated as 761s and no dry spot is observed; nevertheless, the lead-lag between the top and bottom skins is present.

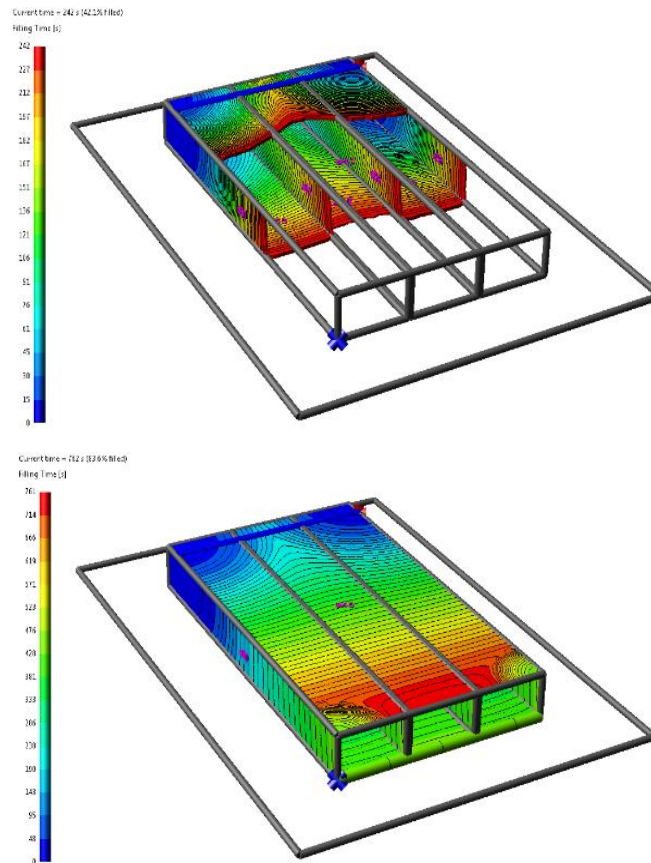


**Figure 8:** Resin flow propagation at a)  $t=242s$  b)  $t=761s$ .

Considering the injection strategy, there can be two possible reasons for the lead-lag: (1) Suction is applied from the lower surface. (2) As the resin feed line on the top skin, resin is forced to travel around the three molds, which are wrapped with preform.

## CONCLUSIONS

In this study, the simulation of co-cured three-cell box beam is presented. Both resin and preform characterization tests are carried out. One of the important results we have achieved from the characterization tests is that porosity of preform declines as the number of layer increases. The effect of vacuum level is additionally investigated for the layers and the results are presented in Figure 3. For the resin viscosity both the temperature and curing effects are investigated. The simulation results show that dry is not the case for the selected injection strategy; nonetheless the lead-lag between the top and bottom skins is observed. The reasons for the lead-lag are presented.

## ACKNOWLEDGEMENTS

The authors would like to thank İZOREEL Composites for the supports to this research work.

**REFERENCES**

- Bird, B. R., Stewart, W. E., & Lightfoot, E. N. (1960). *Transport Phenomena*. New York: Wiley.
- Kageyama, M., & Yoshida, S. (2000). Development of XF-2 Fighter Composite Structures(cocured composite wings). Proceedings of the 41st structures, structural dynamics, and materials conference and exhibit. AIAA.
- Mahruz, H., Majumdar, P., Saha, M., Shamery, F., & Jeelani, S. (2004). Integral Manufacturing of Composite Skin-Stringer Assembly and Their Stability Analysis. *Applied Composite Materials*(11), 155-171.
- Rudd, C. D., Long, A. C., Kendall, K. N., & Mangin, C. (1997). *Liquid Molding Technologies* (Vol. 31). Woodhead Publishing.
- Xu, W., Gu, Y., Li, M., Ma, X., zhang, D., & Zhang, Z. (2014). Co-curing Process Combining Resin Film Infusion With Prepreg And Co-cured Interlaminar Properties of Carbon Fiber Composites. *Journal of Composite Materials*, 48, 1709-1724.



## SYNTHESIS, CRYSTAL STRUCTURE, MAGNETIC PROPERTY, AND N<sub>2</sub>-GAS-ADSORPTION PROPERTY OF DINUCLEAR COPPER(II) 3,4,5-TRIMETHOXYBENZOATE

Masahiro Mikuriya<sup>1\*</sup>, Chihiro Yamakawa<sup>1</sup>, Kensuke Tanabe<sup>1</sup>, Daisuke Yoshioka<sup>1</sup>, Ryoji Mitsuhashi<sup>1</sup>, Hidekazu Tanaka<sup>2</sup> and Makoto Handa<sup>2</sup>

1. Kwanaei Gakuin University, School of Science and Technology, Department of Applied Chemistry for Environment, Sanda, 669-1337 Japan
2. Shimane University, Interdisciplinary Graduate School of Science and Engineering, Department of Chemistry, Matsue 690-8504, Japan

(This article first appeared in PPM2017 and was accepted as a non-peer-reviewed manuscript to be published in JOTCSA)

**Abstract:** Copper(II) 3,4,5-trimethoxybenzoate,  $[\text{Cu}_2(3,4,5\text{-(CH}_3\text{O)}_3\text{C}_6\text{H}_2\text{CO}_2)_4(\text{CH}_3\text{OH})_2]\cdot 2\text{DMF}$ , was prepared and characterized by elemental analysis, infrared and UV-vis spectra and temperature dependence of magnetic susceptibilities (4.5–300 K). The crystal structure was determined by the single-crystal X-ray diffraction method. It crystallizes in the triclinic space group  $P\bar{1}$  with  $a = 8.2110(13) \text{ \AA}$ ,  $b = 13.181(2) \text{ \AA}$ ,  $c = 13.409(2) \text{ \AA}$ ,  $\alpha = 97.967(3)^\circ$ ,  $\beta = 102.378(3)^\circ$ ,  $\gamma = 105.009(3)^\circ$ ,  $V = 1339.8(4) \text{ \AA}^3$ ,  $D_x = 1.465 \text{ g/cm}^3$ , and  $Z = 1$ . The  $R1 [I > 2\sigma(I)]$  and  $wR2$  (all data) values are 0.0363 and 0.0816, respectively, for all 5991 independent reflections. The crystal contains crystallographically centrosymmetric dinuclear molecule with axial methanol molecules and crystal DMF molecules [ $\text{Cu}\cdots\text{Cu}$  2.6190(6)  $\text{ \AA}$ ]. Magnetic susceptibility data show a considerable antiferromagnetic interaction between the two copper(II) ions ( $2J = -292 \text{ cm}^{-1}$ ). Gas-adsorption behavior was investigated for N<sub>2</sub>.

**Keywords:** Dinuclear copper complex, crystal structure determinations, nitrogen gas absorption property.

**Cite this:** Mikuriya M, Yamakawa C, Tanabe K, Yoshioka D, Mitsuhashi R, Tanaka H, vd. SYNTHESIS, CRYSTAL STRUCTURE, MAGNETIC PROPERTY, AND N<sub>2</sub>-GAS-ADSORPTION PROPERTY OF DINUCLEAR COPPER(II) 3,4,5-TRIMETHOXYBENZOATE. JOTCSA. 2017;5(sp.is.1):103–110.

\*Corresponding author. Masahiro Mikuriya, [junpei@kwansei.ac.jp](mailto:junpei@kwansei.ac.jp).

## INTRODUCTION

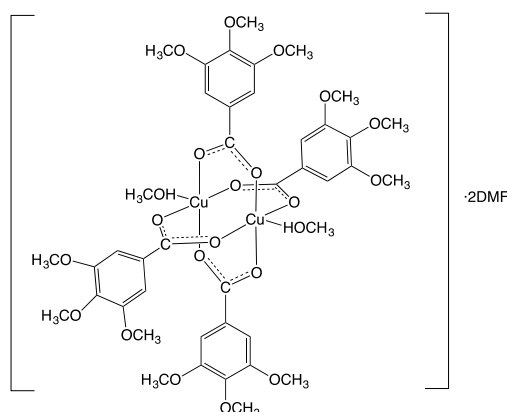


**Figure 1:** Chemical structure of  $[\text{Cu}_2(345\text{tmbz})_4(\text{CH}_3\text{OH})_2] \cdot 2\text{DMF}$ .

Copper acetate  $[\text{Cu}_2(\text{CH}_3\text{CO}_2)_4(\text{H}_2\text{O})_2]$  is a famous copper(II) compound with a lantern-like dinuclear core and has attracted much attention for a long period because of the unique structure and properties [Horikoshi and Mikuriya, 2005; Matsushima *et al.*, 1999; Mori *et al.*, 1999; Mikuriya *et al.*, 1995; Mikuriya *et al.*, 1977; Mikuriya *et al.*, 1999; Mikuriya *et al.*, 2000a; Mikuriya *et al.*, 2000b; Mikuriya *et al.*, 2002a; Mikuriya *et al.*, 2002b; Mikuriya, 2008; Mikuriya *et al.*, 2015a; Mikuriya *et al.*, 2015b, Nakashima *et al.*, 1985; Nukada *et al.*, 1999; Nukada *et al.*, 2001; Nukada *et al.*, 2015]. There are a number of analogous compounds with a lantern-like core as dinuclear metal carboxylates [Cotton *et al.*, 2005]. Previously, we reported that copper(II) benzoate forms a chain compound with pyrazine and the assembled compound has a gas-occlusion property for  $\text{N}_2$  [Nukada *et al.*, 1999]. We found that the aromaticity of the benzoate group plays an important role to construct a hydrophobic micropore [Nukada *et al.*, 2015]. In order to understand the adsorption properties of these compounds, systematic investigations are needed for various types of copper(II) carboxylates. In this study, we synthesized a dinuclear copper(II) complex with a lantern-like core by using 3,4,5-trimethoxybenzoic acid (H345tmbz) substituted with methoxy group at the three positions of the benzoate group (Figure 1) in order to give variety to these compounds. The isolated compound was characterized by measuring elemental-analysis data, infrared and UV-Vis spectra, and temperature dependence of magnetic susceptibility. Crystal structure was determined by the single-crystal X-ray diffraction method. Gas-adsorption behavior was investigated for  $\text{N}_2$ .

## EXPERIMENTAL

Copper(II) 3,4,5-trimethoxybenzoate was prepared by the following method.  $[\text{Cu}_2(345\text{tmbz})_4(\text{CH}_3\text{OH})_2] \cdot 2\text{DMF}$ : A 0.505 g (2.38 mmol) portion of 3,4,5-trimethoxybenzoic acid was added to a 5  $\text{cm}^3$  of 0.10 M sodium hydroxide solution. The mixed solution was neutralized by adding nitric acid with phenolphthalein indicator. To this solution, a solution of

copper(II) nitrate trihydrate (0.301 g, 1.25 mmol) in water (5 cm<sup>3</sup>) was added with stirring to give a pale blue precipitate. The precipitate was collected and dried under vacuum. Yield, 0.587 g (72.2%). Anal. Found: C, 47.57; H, 4.86%. Calcd for C<sub>40</sub>H<sub>48</sub>Cu<sub>2</sub>O<sub>22</sub>: C, 47.67; H, 4.80%. The precipitate was recrystallized from DMF-methanol to give greenish blue crystals. Anal. Found: C, 49.13; H, 5.39; N, 2.59%. Calcd for C<sub>48</sub>H<sub>66</sub>Cu<sub>2</sub>N<sub>2</sub>O<sub>24</sub>: C, 48.77; H, 5.63; N, 2.37%. IR (KBr, cm<sup>-1</sup>): 3019, 2943 ( $\nu_{\text{as}}\text{CH}_3$ ), 2838 ( $\nu_{\text{s}}\text{CH}_3$ ), 1574 ( $\nu_{\text{as}}\text{COO}$ ), 1415 ( $\nu_{\text{s}}\text{COO}$ ). Diffuse reflectance spectra:  $\lambda_{\text{max}}$  280, 370sh, 716 nm.

Measurements: Elemental analyses for C, H, and N were performed using a Thermo-Finnigan FLASH EA1112 series CHNO-S analyzer. Infrared spectra were measured with a JASCO MFT-2000 FT-IR Spectrometer in the 4000–600 cm<sup>-1</sup> region. Diffuse reflectance spectra were measured with a Shimadzu UV-vis-NIR Recording Spectrophotometer Model UV-3100. Magnetic susceptibilities were measured with a Quantum Design MPMS-XL7 SQUID susceptometer operating at a magnetic field of 0.5 T over a range of 4.5–300 K. Adsorption measurements for N<sub>2</sub> were performed by a MicrotracBEL BELSORP-mini II. Prior to the adsorption, the sample was evacuated at 298 K for 2h.

X-Ray Crystallography: X-Ray diffraction data were collected on a Bruker CCD X-ray diffractometer (SMART APEX) using graphite-monochromated Mo-K $\alpha$  radiation. Crystal data of [Cu<sub>2</sub>(345tmbz)<sub>4</sub>(CH<sub>3</sub>OH)<sub>2</sub>] $\cdot$ 2DMF: C<sub>48</sub>H<sub>66</sub>Cu<sub>2</sub>N<sub>2</sub>O<sub>24</sub>,  $M_r = 1182.1$ ,  $T = 90$  K, triclinic, space group  $P\bar{1}$  with  $a = 8.2110(13)$  Å,  $b = 13.181(2)$  Å,  $c = 13.409(2)$  Å,  $\alpha = 97.967(3)^\circ$ ,  $\beta = 102.378(3)^\circ$ ,  $\gamma = 105.009(3)^\circ$ ,  $V = 1339.8(4)$  Å<sup>3</sup>,  $D_x = 1.465$  g/cm<sup>3</sup>, and  $Z = 1$ . The  $R1$  [ $I > 2\sigma(I)$ ] and  $wR2$  (all data) values are 0.0363 and 0.0816, respectively, for all 5991 independent reflections.

The structures were solved by direct methods, and refined by full-matrix least-squares method. The hydrogen atom attached to the coordinating methanol molecule was located from a difference Fourier map and the others were inserted at their calculated positions and fixed there. All of the calculations were carried out on a Windows 7 Core i5 computer utilizing the SHELXTL software package (Sheldrick 2008) and SHELXL-2014/7 (Sheldrick 2015). Crystallographic data have been deposited with Cambridge Crystallographic Data Centre: Deposit number CCDC-1570806. Copies of the data can be obtained free of charge via <http://www.ccdc.cam.ac.uk/conts/retrieving.html> (or from the Cambridge Crystallographic Data Centre, 12, Union Road, Cambridge, CB2 1EZ, UK; Fax: +44 1223 336033; e-mail: [deposit@ccdc.cam.ac.uk](mailto:deposit@ccdc.cam.ac.uk)).

## RESULTS AND DISCUSSION

Elemental analysis of the isolated compound showed the formulation  $[\text{Cu}_2(345\text{tmbz})_4(\text{CH}_3\text{OH})_2] \cdot 2\text{DMF}$ . IR data showed two COO stretching bands at 1574 and 1415  $\text{cm}^{-1}$  with the difference in energy characteristic of bridging carboxylate [Nakamoto, 2009]. The diffuse reflectance spectrum of  $[\text{Cu}_2(345\text{tmbz})_4(\text{CH}_3\text{OH})_2] \cdot 2\text{DMF}$  shows a strong band at 280 nm, a shoulder at 370 nm, and a broad band at 716 nm with a shoulder at lower energy side in the visible region. The former two bands can be assigned to LMCT bands from the carboxylato-oxygen to the  $\text{Cu}^{\text{II}}$  d orbital. The visible region band can be associated with d-d transitions, confirming a square-pyramidal coordination environment of the copper(II) atoms.

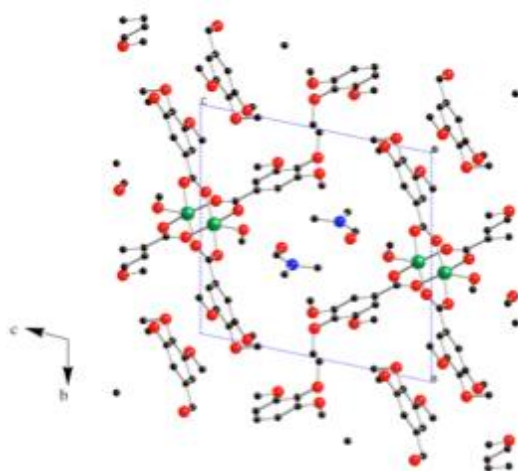


**Figure 2:** Molecular structure of  $[\text{Cu}_2(345\text{tmbz})_4(\text{CH}_3\text{OH})_2] \cdot 2\text{DMF}$ . The thermal ellipsoids are shown at the 50% probability level. Hydrogen atoms are omitted for clarity. Symmetry code: (i)  $1-x, 1-y, -z$ .

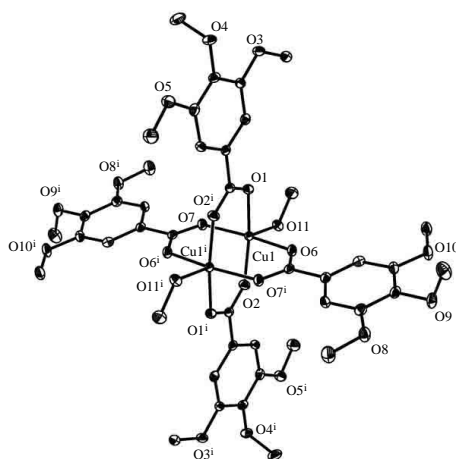


**Figure 3:** Packing diagram of  $[\text{Cu}_2(345\text{tmbz})_4(\text{CH}_3\text{OH})_2] \cdot 2\text{DMF}$ .

The molecular structure for  $[\text{Cu}_2(345\text{tmbz})_4(\text{CH}_3\text{OH})_2] \cdot 2\text{DMF}$  was drawn as an ORTEP diagram (Figure 2). The asymmetric unit contains one crystal DMF molecule and one-half of dinuclear  $[\text{Cu}_2(345\text{tmbz})_4(\text{CH}_3\text{OH})_2]$  unit with a crystallographic inversion center at the midpoint of the

Cu1 and Cu1<sup>i</sup> atoms. The dinuclear unit has a lantern-like dinuclear core bridged by four 345tmbz<sup>-</sup> ligands in a *syn-syn* fashion [Mikuriya, 2008]. The Cu1...Cu1<sup>i</sup> distance is 2.6190(6) Å, which is in the range found in dinuclear copper(II) carboxylates [Mikuriya, 2008; Mikuriya *et al.*, 1995; Mikuriya *et al.*, 2015a; Mikuriya *et al.*, 2015b; Nukada *et al.*, 1999]. The coordination geometry around each copper atom is an elongated square-pyramid. The bond distances of the Cu1 and basal O atoms are 1.9529(14)–1.9688(15) Å, which are within the normal range found in copper(II) carboxylates. The fifth position of the Cu1 atom is occupied by a methanol molecule with the Cu1-O11 distance of 2.1582(15) Å, which is also in the normal range as axial bonding for the copper(II) carboxylates [Mikuriya, 2008]. In the crystal, DMF molecules are trapped into the cavities between the dinuclear units (Figure 3).

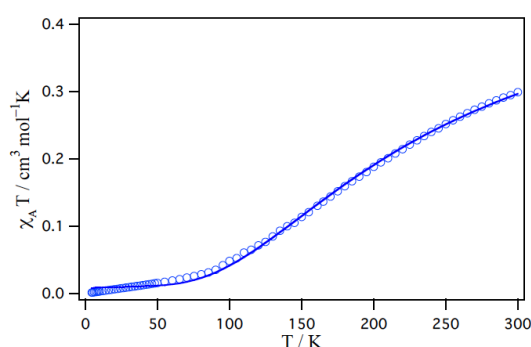


**Figure 4:** Temperature dependence of  $\chi_A T$  of  $[\text{Cu}_2(345\text{tmbz})_4(\text{CH}_3\text{OH})_2]\cdot 2\text{DMF}$ . The solid lines represent the best fit of the data.

The magnetic data of  $[\text{Cu}_2(345\text{tmbz})_4(\text{CH}_3\text{OH})_2]\cdot 2\text{DMF}$  are shown in the form of  $\chi_A T$  vs  $T$  plot (Figure 4). The magnetic moment at 300 K is  $1.55 \mu_B$  (per  $\text{Cu}^{\text{II}}$  unit), which is significantly lower than the spin-only value ( $1.73 \mu_B$ ) of  $\text{Cu}^{\text{II}}$  ( $S = 1/2$ ) ion. The magnetic moment decreases with lowering of the temperature, showing a considerable antiferromagnetic interaction between the copper(II) ions. The magnetic data were analyzed with the Bleaney-Bowers equation based on the Heisenberg model ( $H = -2JS_1 \cdot S_2$  ( $S_1 = S_2 = 1/2$ )):

$$\chi_A = (1-p)[Ng^2\mu_B^2/kT][3+\exp(-2J/kT)]^{-1} + pNg^2\mu_B^2/4kT + Na,$$

where  $J$  is an exchange coupling constant for the two copper(II) ions,  $p$  is the fraction of mononuclear impurity, and  $Na$  is the temperature-independent paramagnetism, which was set to  $60 \times 10^{-6} \text{ cm}^3 \text{ mol}^{-1}$  for each copper(II) ion (Horikoshi and Mikuriya, 2005). The best-fitting parameters ( $2J = -292(2) \text{ cm}^{-1}$ ,  $g = 2.28(1)$ ,  $p = 0.0171(1)$ ) are normal as copper(II) carboxylates, showing a strong antiferromagnetic interaction between the two copper(II) ions.

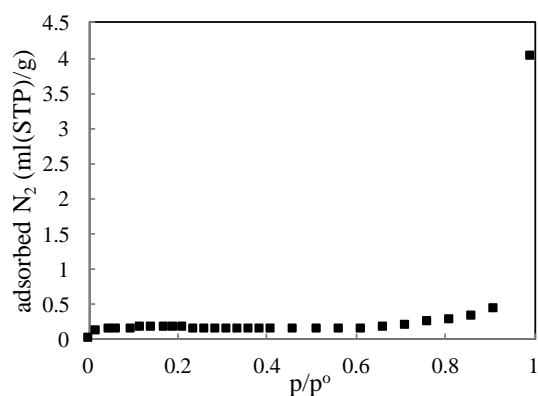


**Figure 5:** N<sub>2</sub> adsorption isotherm on [Cu<sub>2</sub>(345tmbz)<sub>4</sub>(CH<sub>3</sub>OH)<sub>2</sub>] $\cdot$ 2DMF.

We expected an adsorbing ability for the present complex, if the crystal DMF molecules are lost. However, the adsorption isotherm of [Cu<sub>2</sub>(345tmbz)<sub>4</sub>(CH<sub>3</sub>OH)<sub>2</sub>] $\cdot$ 2DMF showed that the isotherm belongs to Type II in the IUPAC classification ( $S_{\text{BET}} = 0.4 \text{ m}^2\text{g}^{-1}$ ), suggesting that physical adsorption only occurred because the cavities in the crystal seem to have been still occupied by DMF molecules at the measurement.

## ACKNOWLEDGEMENTS

The present work was partially supported by Grant-in-Aid for Scientific Research No. 17K05820 from the Ministry of Education, Culture, Sports, Science and Technology (MEXT, Japan).

## REFERENCES

- Cotton, F. A., Murillo, C. A., Walton, R. A., 2005, Multiple Bonds Between Metal Atoms, 3rd ed., Springer Science and Business Media, New York, 1.
- Horikoshi, R. and Mikuriya, M., 2005, One-Dimensional Coordination Polymers from the Self-Assembly of Copper(II) Carboxylates and 4,4'-Dithiobis(pyridine), *Bull. Chem. Soc. Jpn.*, 78, 827.
- Matsushima, H., Koikawa, M., Nukada, R., Mikuriya, M., Tokii, T., 1999, Structural Characterization and Magnetic Properties of Triply Carboxylato-Bridged Dinuclear Copper(II) Complexes, *Bull. Chem. Soc. Jpn.*, 72, 1025.
- Mikuriya, M., Nukada, R., Morishita, H., and Handa, M., 1995. Chain Compounds Formed by the Reaction of Copper(II) Carboxylate [Cu<sub>2</sub>(O<sub>2</sub>CR)<sub>4</sub>] (R = C(CH<sub>3</sub>)<sub>3</sub>, CCl<sub>3</sub>) and Bridging Ligand L (L = Pyrazine, 4,4'-Bipyridine, and 1,4-Diazabicyclo[2.2.2]octane), *Chem. Lett.*, 24, 617.
- Mikuriya, M., Kida, S., Ueda, I., Tokii, T., Muto, Y., 1977. The Crystal Structure and Magnetic Property of Di- $\mu$ -propionato-*O,O'*-bis[*N-p*-tolylsalicylideneaminatocopper(II)], *Bull. Chem. Soc. Jpn.*, 50, 2464.

- Mikuriya, M., Azuma, H., Nukada, R., and Handa, M., Synthesis, 1999. X-Ray Structures, and Magnetic Properties of  $[\text{Cu}_2(\text{piv})_4(\text{Et}_3\text{N})_2]$  and  $[\text{Cu}_6(\text{piv})_6(\text{EtO})_6]$  (Hpiv = Pivalic Acid): Role of Base for Dinuclear Adduct and Oligonuclear Formation, *Chem. Lett.*, 57.
- Mikuriya, M., Azuma, H., Nukada, R., Sayama, Y., Tanaka, K., Lim, J.-W., and Handa, M., 2000a. Antiferromagnetic Adducts of Copper(II) Propionate with Pyridyl Nitronyl Nitroxides, *Bull. Chem. Soc. Jpn.*, 73, 2493.
- Mikuriya, M., Azuma, H., Handa, M., 2000b. Coordination Polymers of Copper(II) and Copper(I) Trifluoroacetates with Pyrazine, *Mol. Cryst. Liq. Cryst.*, 342, 205.
- Mikuriya, M., Azuma, H., Sun, J., Yoshioka, D., and Handa, M., 2002a. Dinuclear Copper(II) Complexes of Free Radical Carboxylic Acids, *Chem. Lett.*, 608.
- Mikuriya, M., Azuma, H., Handa, M., 2002b. Coordination Polymers of Copper(II) Propionate with Linking Ligands, *Mol. Cryst. Liq. Cryst.*, 379, 205.
- Mikuriya, M., 2008. Copper(II) Acetate as a Motif for Metal-Assembled Complexes, *Bull. Jpn. Soc. Coord. Chem.* 52, 17.
- Mikuriya, M., Yano, M., Takahashi, N., Yoshioka, D., Tanaka, H., and Handa, M., 2015a. Synthesis and Crystal Structure of a Chain Complex of Copper(II) Pivalate and 1,2-Bis(4-pyridyl)ethane in Relation to Adsorption Property for  $\text{N}_2$ , *X-ray Struct. Anal. Online*, 31, 47.
- Mikuriya, M., Yano, M., Takahashi, N., Yoshioka, D., Tanaka, H., and Handa, M., 2015b. Synthesis, crystal structure, magnetic property, and  $\text{N}_2$ -gas-adsorption property of chain compounds of dinuclear copper(II) pivalate with  $N,N'$ -bidentate ligands, *The Proceedings of the 2nd International Porous and Powder Materials Symposium and Exhibition PPM 2015*, Üç Adım Printing House, Izmir, Turkey, 72.
- Mori, W., Hoshino, H., Nishimoto, Y., and Takamizawa, S., 1999. Synthesis and Gas Occlusion of New Micropore Substance Rhodium(II) Carboxylates Bridged by Pyrazine, *Chem. Lett.*, 331.
- Nakamoto, K., 2009. *Infrared and Raman Spectra of Inorganic and Coordination Compounds, Part B* (6th ed.) John Wiley & Sons, Inc, Hoboken.
- Nakashima, M., Mikuriya, M., and Muto, Y., 1985, Structural, Magnetic and IR Spectroscopic Characterization of Dinuclear Copper(II) Trichloroacetic Adduct with Benzonitrile. Nature of the Copper(II)-Benzonitrile Bond, *Bull. Chem. Soc. Jpn.*, 58, 968.
- Nukada, R., Mori, W., Takamizawa, S., Mikuriya, M., Handa, M., and Naono, H., 1999. Microporous Structure of a Chain Compound of Copper(II) Benzoate Bridged by Pyrazine, *Chem. Lett.*, 367.

Nukada, R., Mikuriya, M., Yamashita, A., and Handa, M., 2001. Mononuclear and Polynuclear Chain Compounds of Copper(II) Pivalate with *N,N'*-Didentate Ligands, Challenges for Coordination Chemistry in the New Century, Slovak Technical University Press, Bratislava, Slovakia, 83.

Nukada, R., Mikuriya, M., Handa, M., and Naono, H., 2015. Hydrophobic micropore in a chain compound of dinuclear copper(II) benzoate with pyrazine—Adsorption properties for N<sub>2</sub>, CCl<sub>4</sub>, H<sub>2</sub>O, CO<sub>2</sub>, and CH<sub>3</sub>CN. The Proceedings of the 2nd International Porous and Powder Materials Symposium and Exhibition PPM 2015, Üç Adım Printing House, Izmir, Turkey, 77.

Sheldrick, G. M., 2008. A short history of SHELX. Acta Crystallogr. Sect A, 64, 112.

Sheldrick, G. M., 2015, Crystal Structure refinement with SHELXL, Acta Crystallogr. Sect C, 71, 3.